The cold, the hot, and the puffy

Atmospheric lessons from three transiting exoplanets

Submitted by Jessica Spake

to the University of Exeter as a thesis for the degree of

Doctor of Philosophy in Physics

May 2019

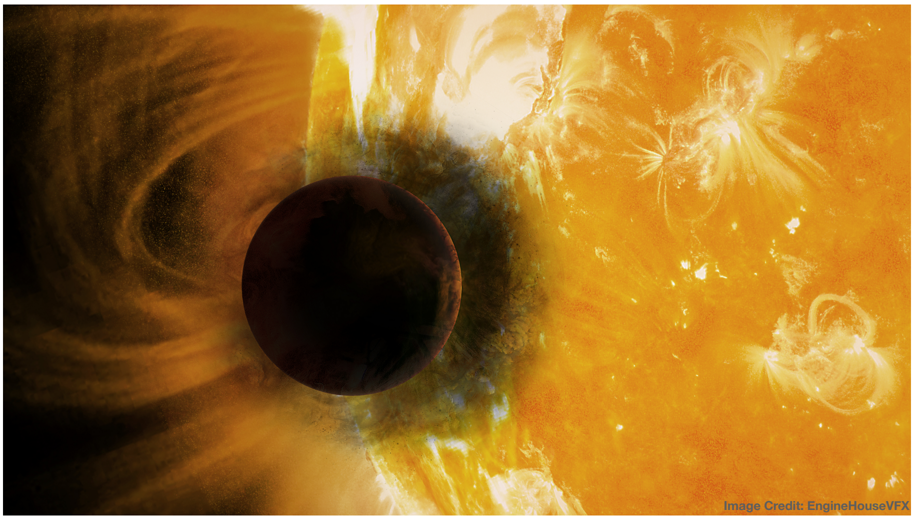

Image Credit: EngineHouseVFX

……………………………

Abstract

Exoplanets are complex astrophysical bodies but are difficult to study in detail. Despite the challenges, we are starting to solve the interrelated puzzles of what exoplanets are made of; how they evolve; and how their atmospheric dynamics work. Exoplanet atmospheres have particularly small measurable signatures, to which we must apply precise and innovative observations. We must choose case-study planets carefully, as time on the best telescopes is limited. One solution is to study extreme systems (e.g. the coldest, the hottest, the lowest-density planets), which are laboratories for testing our understanding of atmospheric physics at their limits. To that end, the three projects presented here are observations of extreme gas-giant exoplanets that transit their host stars. Firstly, using the Hubble Space Telescope (HST)'s Wide Field Camera 3 instrument (WFC3), we measured the 0.8 - 1.1 μm transmission spectrum of WASP-107b, which has a relatively cold equilibrium temperature of 700 K. With these observations we detected helium on an exoplanet for the first time, via the 10 830Å line of metastable helium, and showed that WASP-107b has an extended and possibly escaping upper atmosphere. Secondly, we observed a near-infrared phase curve of the hot (2 100 K) exoplanet WASP-19b with HST's WFC3, covering the 1.1 - 1.7μm wavelength range. We detected a large hotspot offset in its phase curve (60° in longitude), which means WASP-19b likely has strong equatorial winds in its deep (1 bar) atmosphere. Thirdly, WASP-127b is one of the lowest-density planets known to science and an attractive target for atmospheric characterisation. We observed a near-ultraviolet to near-infrared transmission spectrum, covering 0.3-5μm, of WASP-127b using HST and the Spitzer space telescope. On this planet, we detected sodium, potassium, water, carbon-bearing species, and some unknown hazes and clouds. In summary of our contributions to the puzzles mentioned above: we introduced a new method to observe exoplanet atmospheres and escape processes; we added to the growing sample of measurements of heat transport in exoplanet atmospheres; and we made a step towards determining the atmospheric composition of an ideal planet for study with the upcoming James Webb Space Telescope.

Acknowledgements

I am indebted to the STFC for funding this PhD and the travel that it involved. Thank you for allowing me to live my dream of doing science as a day job - I was a terrible waitress. Additionally, these results would not have been possible without funding from the European Research Council under the European Unions Seventh Framework Programme (FP7/2007-2013) / ERC grant agreement no. 336792. To hell with Brexit. Thanks to my Mum, Carl, and my Dad for financial support and accommodation while I wrote up this work. My thoughts go to those students whose curiosity burns but who do not have the means to do science. I was extremely fortunate.

My first personal thanks go to David Sing for his unfailing expertise; for his remarkable patience and generosity; for never once being too busy to listen; for gently steering me towards more exciting work than I could have imagined; and for being a joy to work with. I thank my lucky stars (WASP-107 and WASP-127) I got to do a PhD with such a brilliant scientist and kind mentor.

Thanks to Nikolay Nikolov for hundreds of hours of help with data analysis, scientific guidance, and emotional support. Thanks to Tom Evans for all that plus everything else.

Thanks to Nathan Mayne for comments on this thesis, and for being an enthusiastic and thoughtful second supervisor; Jayesh Goyal for many joyous conversations, and for being a wonderful friend and collaborator; Hannah Wakeford and Tiffany Kataria for lifting me up scientifically, and helping me back down again with a few pints afterwards; Coel Hellier for the good planets; Antonija Oklopčić for her exciting work and for sharing a memorable moment; Andrea Dupree for introducing us; Lynne Hillenbrand for her expertise and patience; David Ehrenreich and his group for their collaboration; Drake Deming for being reviewer number one in every sense; James Owen for his priceless guidance; Sara Seager and Laura Kreidberg for inspiring and encouraging me; Rox Middleton, Chess Boughey and Carmen Palacios-Berraquero for giving me free accommodation in Cambridge; Didier Queloz for taking a chance on me years ago; Brice-Olivier Demory for kind supervision back then; Don Pollacco for the latter two things plus a sick reference letter; too many friends from Warwick

to count; collaborators, dear friends, and drinking partners from Exeter, especially Elisabeth Matthews, Tom Constantino, Tom Goffrey, Ahmad Ali, Aarrynn Carter, and Alice Mills; Jennifer Hatchell, Matthew Bate, and Isabelle Barraffe for academic support; Emma Way, Jenny Seat, Martyn Brake, and Krysztian Kohary for paperwork and IT support; Theresa for brightening my time in the office and saving me from my own mess; my new friends and collaborators from Baltimore, in particular Sarah Moran, Ankit Barik, and Regu Angappan.

Sincere thanks go to my two examiners - Peter Wheatley and Tim Naylor - for extremely helpful comments which significantly improved this thesis.

Thanks to all of my friends, but especially Chess Boughey, Rox Middleton, Sally Blumenthal, Daisy Vaughan, and Yolanda Ohene, for teaching me that the most dazzling life forms that I'd like to connect with are here on Earth.

Thanks to all of my family, especially Dad, Avril, Harriet, Maddie, Nan Rosa, Grandad Derek, Carl, and Auntie Mandy, for their limitless support and for cheering me on. Thanks Mike for putting up with me your entire life. I am so proud of you.

Finally and most importantly, thank you Mum. I owe you the most. You raised us with a fierce love, all by yourself, and whenever I search myself for courage it's your voice I hear in my head shouting 'COME ON JESSAYYY' like you did when I was struggling to swim my first 2 km. It keeps me going. Thank you for being both my biggest fan, and biggest influence.

Dedication

At the National Air and Space Museum in Washington, DC, they have a life-sized replica of the Hubble Space Telescope. It shares an exhibit with missiles and ceramic noses for nuclear warheads. The first time I saw it I heard an eight- or nine-year-old girl scream "Look! It's the Hubble!" as she ran towards it. I'd never felt as honored that I got to use Hubble data as I did then. I dedicate this work to her, and all the others who walk past weapons to delight in a more beautiful vision of the universe.

Contents

Chapter 1

Introduction

1.1 Motivation

Exoplanets are more diverse than planet formation and evolution theorists had perhaps imagined before 1995, when the first exoplanet around a sun-like star was discovered - a gas giant orbiting its host every 4 days (Mayor & Queloz 1995). We must study a large number of exoplanets in order to understand the physical laws that generated the population we observe today and to be able to predict what it is *like* on a given exoplanet that we cannot visit. Planetary atmospheres are complex, and they vary depending on many physical processes like the activity of the host star; the history of atmospheric escape; stellar and planetary magnetic fields; impact pollution; greenhouse effects; cloud feedback; surface oceans; and weathering, to name a few. How could one predict, for example, the presence of surface water on an exoplanet knowing only its mass, radius, and mean stellar flux? Detailed observations of individual exoplanet atmospheres are expensive in telescope time and capital but may help to build coherent pictures of the dominant atmospheric processes of benchmark systems. The lessons learnt may then be included in models of those exoplanets whose atmospheres we are unable to observe.

Given limited telescope time, we must choose case-study exoplanets carefully. There are two things to take into account: firstly, what could we learn from a given system?

Extreme exoplanets (e.g. the coldest, the hottest, the fastest-rotating) are laboratories for testing predictions of atmospheric physics, at their extreme limits where the physical effects can more easily be isolated and tested. Secondly, we should consider limits of technology. Warm, transiting, gas-giant exoplanets around bright stars have some of the most readily-observable atmospheres. The atmospheres of Earth-sized exoplanets remain out of reach for now (e.g. Greene et al. 2016). Here I present the lessons in atmospheric physics learnt from three transiting, gas-giant exoplanets with highly observable atmospheres. The cold: WASP-107b is a low-mass gas giant orbiting a cool, orange star; it is one of the coldest exoplanets to have its atmosphere detected so far. The hot: WASP-19b is an ultra-hot, massive gas giant with one of the shortest orbital periods known. The puffy: WASP-127b is the lowest-density gas giant known to science, which means it has a very extended, 'puffy' atmosphere, highly amenable to transit spectroscopy.

1.2 Background

1.2.1 How we observe exoplanets and their atmospheres

Only a few exoplanets have been imaged directly. Because of the high brightness contrast between a planet and its host star (e.g. $\sim 10^{-10}$ for the Earth/Sun system in visible light), direct imaging has only been possible for a few young, massive planets (of several Jupiter masses) on wide orbits around very nearby stars (e.g. Marois et al. 2008, Lagrange et al. 2010, Rameau et al. 2013). It is possible to measure spectra of directly imaged planets and hence probe the composition and temperature structure of their atmospheres (e.g. Macintosh et al. 2015, Bonnefoy et al. 2016 , Chauvin et al. 2017). However, we cannot yet observe the vast majority of exoplanets in this way. Instead, we must detect and characterise exoplanets using indirect methods.

The first exoplanet found around a sun-like star was discovered using the radial velocity technique (Mayor & Queloz 1995). This indirect way to detect exoplanets works by searching for the gravitational influence of an exoplanet on its host star. Both the star and its planet orbit the common centre of mass of the system, and one can detect the back-and-forth wobbling motion of the star, in the line of sight (the radial direction) by looking for Doppler shifts in high-resolution stellar spectra. Unless a planet's orbit is perfectly perpendicular to the plane of the sky (i.e. at an inclination of 90°), then some component of the star's velocity will be parallel to the plane of the sky, and immeasurable to us with the radial velocity technique. A more massive planet with an orbital inclination less than 90°can give the same stellar radial velocity amplitude as a less massive planet with an inclination of 90°. Therefore we can only measure the planet's minimum mass with the radial velocity technique. If the orbital inclination of the planet is further constrained then the mass estimate can be greatly improved.

The transit technique is by far the most successful exoplanet detection method[1]. If all the planetary systems in the galaxy are aligned randomly relative to our line of sight, some planets will, by chance, pass in front of their host star once per orbit, and block out some of the starlight. This event is called a transit, and we can detect transiting exoplanets by measuring the stellar flux over time and searching for repeated dips in the stellar brightness. The amount of light that the planet obscures can be used to estimate its size. A typical transit depth for a large gas giant orbiting a sun-like star is $\sim 1-2\%$, but for an Earth-sized planet, it is $\sim 0.01\%$. Wide-field, ground-based transit surveys dominated exoplanet detections in the 2000s, for example, the HATNet survey (Bakos et al. 2004); OGLE (Udalski et al. 2002); TrES (Alonso et al. 2004); and especially WASP (Pollacco et al. 2006) - all three planets in this study were discovered by the WASP survey. In 2009 the *Kepler* space telescope was launched (Borucki et al. 2010), which found thousands of transiting exoplanets in a small patch of sky, and the following K2 mission has found hundreds of planets along the ecliptic plane. Planets are still being found in the *Kepler* and K2 archival data. The next generation of transit surveys are focused on finding small planets around bright stars across the entire sky, like the ground-based NGTS (Wheatley

---

[1] exoplanets.org, accessed 10/03/2019

et al. 2018); and the space-based TESS (Ricker et al. 2015), which was launched in 2018 (see Section 5.2.1).

The combination of the transit and radial velocity techniques is a powerful way to determine some of the bulk properties of an exoplanet and its host star. Once the stellar mass and radius have been estimated by comparing observed spectra of the host star to stellar models, the radius of the planet can be determined from the transit depth, and the inclination of the planet's orbit can be measured from the shape of the transit[2]. The transit duration, period, and orbital inclination provide a powerful, independent measurement of the bulk density of the star. This is because, for a circular orbit and a given inclination, the ratio of the transit duration to the orbital period gives the ratio of the stellar radius to the orbital distance. If we assume that the star is much more massive than the planet, substituting the radius-to-distance ratio into Kepler's third law yields an expression for the stellar density that depends on directly measurable quantities. The stellar density can immediately be used to rule out giant stars, and a much larger-than-planetary transiting companion (Seager & Mallén-Ornelas 2003).

Also, we can combine the inclination information with radial velocity measurements to precisely estimate the planetary mass. We can then estimate the bulk density of an exoplanet, and understand if the planet is more like a gas giant, for example, rather than a smaller, rocky body.

Transiting exoplanets are extremely valuable for atmospheric studies for two reasons: perhaps the most successful exoplanet atmospheric characterisation technique is transmission spectroscopy (discussed below) - which we can only apply to transiting exoplanets; and transiting exoplanets around typical main-sequence stars are often very amenable to radial velocity measurements[3], which means we can get fairly

---

[2] A transiting planet with an inclination less than 90° will not pass the centre of the stellar disk, and will therefore have a shorter overall transit duration. It will also have a longer ingress and egress, i.e. the time between the first contact of the planet and stellar disk, and the second contact - when the entire planet is in front of the stellar disk. These two effects mean that lower inclination angles give shorter, more V-shaped transits.

[3] Short period, large-radius planets are easier to detect with the transit technique. These planets tend to be massive, so their favourable planet-to-star mass ratios and small orbits result in relatively large radial velocity amplitudes in the star.

precise (∼10%) mass estimates. It is more challenging to interpret observations of exoplanet atmospheres without knowing the mass of the planet, as planetary gravity directly affects many aspects of atmospheric physics, such as the scale height of the atmosphere, and the settling times of any condensate particles. Additionally, the size of the observational signals of exoplanet atmospheres can be degenerate with temperature and atmospheric scale height (higher temperatures and lower gravities give bigger signals). Thirdly, it is currently impossible to directly measure the radii of directly imaged planets, leaving large uncertainties in the planetary gravity (e.g. Lavie et al. 2017). For these reasons, studies of transiting exoplanets have dominated the first two decades of exoplanet atmosphere characterisation. The three planets in this work are all transiting exoplanets. In the following subsections I briefly explain the techniques used to study the atmospheres of transiting exoplanets, and in Section 1.3 I discuss what has been learnt so far with these techniques, and the questions we hope to answer with them next.

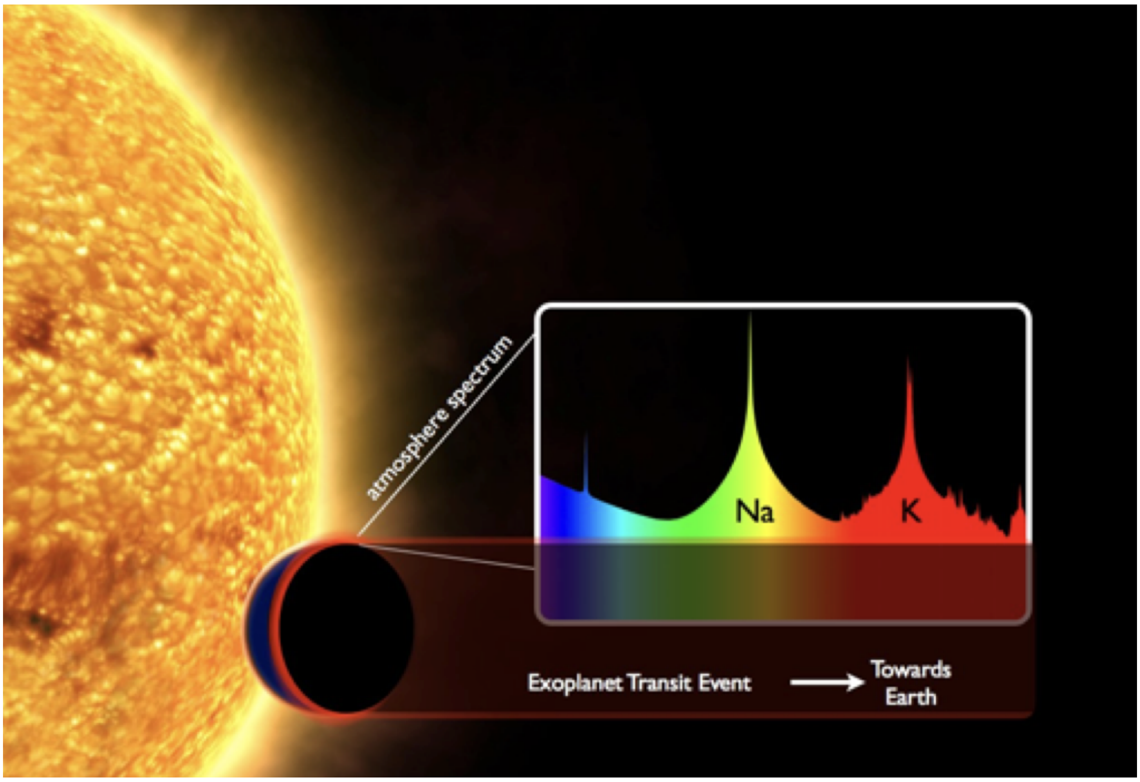

Figure 1.1: A schematic of the transmission spectroscopy technique, which can reveal the composition of exoplanet atmospheres though wavelength-dependent changes in transit depth. Figure from ESO/David Sing (2011)

Transmission spectroscopy

During a transit, stellar light passes through the optically-thin upper atmosphere of a planet. Certain wavelengths of light may be absorbed or scattered by different species in the atmosphere. Measuring the apparent size of the planet at different wavelengths (by measuring the depth of the transit signal) may inform us of the composition of the atmosphere. This technique is called transmission spectroscopy and is illustrated in Figure 1.1.

The use of this technique as a probe of atmospheric composition was suggested and numerically modelled by Seager & Sasselov (2000), Brown (2001), Burrows et al. (2001), and Hubbard et al. (2001). Then Fortney (2005) derived analytical expressions for the optical depth through an exoplanet atmosphere at slant geometry during a transit, assuming that the pressures probed by transmission spectroscopy are under hydrostatic equilibrium, act as an ideal gas, and that the temperature and mean molecular weight does not change over this region (i.e. a Barotropic atmosphere). In this case, the increase in altitude required for the pressure to drop by a factor of e - called the pressure scale height, H, is given by

$$H = \frac{kT}{\mu g}, \tag{1.1}$$

where k is Boltzmann's constant, T is the temperature of the atmosphere, μ is the mean molecular weight, and g is the acceleration due to gravity. We can describe the altitude-dependent number density, $n(z)$, of the atmosphere as

$$n(z) = n_0 e^{-z/H}, \tag{1.2}$$

where n_0 is the volume density at the base of the atmosphere (or "surface" of the planet), and z is the altitude above the surface. Here we define the surface to be at a planetary radius, R_{pl}, below which the entire planet appears opaque at all wavelengths during a transit. Integrating the number density from R_{pl} to infinity gives the *vertical* column density of the atmosphere above the surface:

$$N_{\mathrm{V}} = n_0 H. \tag{1.3}$$

To derive the optical depth of the atmosphere during transit, one must find the *horizontal* column density of the atmosphere through a line, x, tangential to the surface, shown in Figure 1.2. Using Pythagoras' theorem, and assuming that $2R_{\mathrm{pl}}z \gg z$, then $z \approx x^2/2R_{\mathrm{pl}}$, which can be substituted into Equation **??** to give

$$n(x) = n_0 \mathrm{exp}\left(\frac{-x^2}{2R_{\mathrm{pl}}H}\right). \tag{1.4}$$

Integrating $n(x)$ from horizon to horizon gives the horizontal column density:

$$N_{\mathrm{H}} = n_0\sqrt{2\pi R_{\mathrm{pl}}/H}. \tag{1.5}$$

Note that the ratio of the horizontal to vertical column density is large for typical planets - for example for Earth it is approximately 75, and for Jupiter it is approximately 128. For this reason, transmission spectroscopy is only sensitive to the upper layers of exoplanet atmospheres. The optical depth at a given wavelength and altitude, $\tau(\lambda, z)$, is the integral of the product of the absorption cross-section of the dominant absorbing species $\sigma_{\mathrm{abs}}(\lambda)$, and the column density, so

$$\tau(\lambda, z) \approx \sigma(\lambda) n(z)\sqrt{2\pi R_{\mathrm{pl}}/H}. \tag{1.6}$$

Lecavelier Des Etangs et al. (2008) then used the optical depth formula to calculate the effective altitude of a given planetary atmosphere (i.e. how large the atmosphere should appear) as a function of wavelength. The quantity of interest is the equivalent altitude, z_{eq}, in the atmosphere at which an opaque, occulting disk of radius $R_{\mathrm{pl}} + z_{\mathrm{eq}}$ would produce the same absorption depth as the planet plus its semi-transparent atmosphere. We can find z_{eq} by defining the optical depth at that altitude, τ_{eq}, as

$$R_{\mathrm{meas}}(\lambda) = R_{\mathrm{pl}} + z(\tau = \tau_{\mathrm{eq}}), \tag{1.7}$$

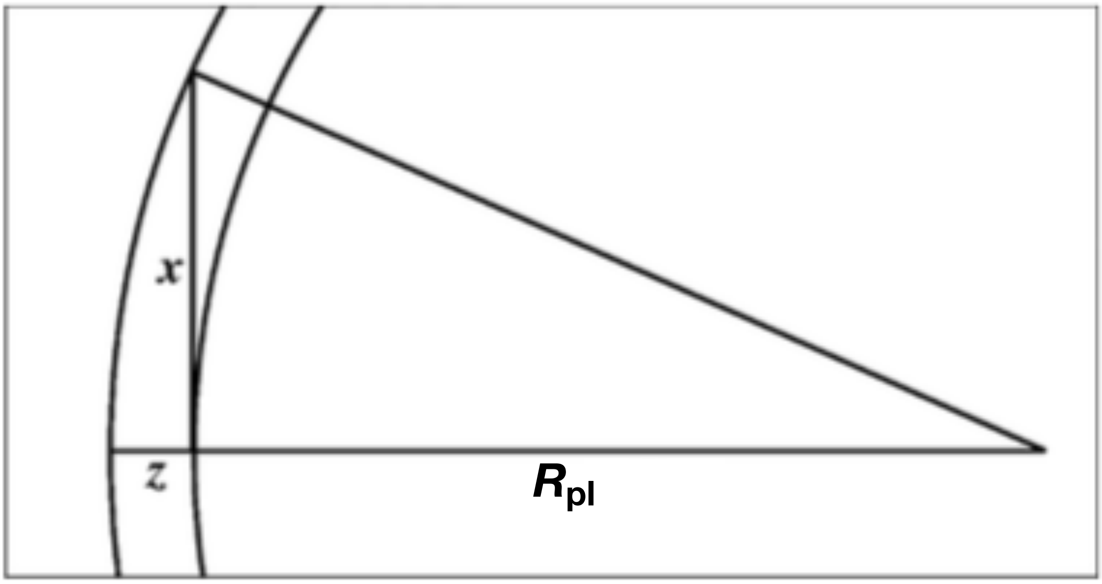

Figure 1.2: For a planet with a large radius R_{pl}, the optical depth for radiation passing through its atmosphere for transmission (through x) can be much longer than for the path radially outwards from the planet surface (z). Figure adapted from Fortney (2005).

where $R_{\mathrm{meas}}(\lambda)$ is the wavelength-dependent, *measured* planet radius. We can combine Equations 1.2, 1.6, and 1.7 to find

$$z(\lambda) = H\ln\Bigg(\xi_{\mathrm{abs}} P_{z=0} \sigma_{\mathrm{abs}}(\lambda)/\tau_{\mathrm{eq}} \times \sqrt{2\pi R_{\mathrm{pl}}/kT\mu g}\Bigg) \tag{1.8}$$

where ξ_{abs} is the fractional abundance of the dominant absorbing species in the atmosphere, and $P_{z=0}$ is the atmospheric pressure at R_{pl}. An important point to note is that $z(\lambda)$, the effective altitude, is directly measurable with transmission spectroscopy. A transmission spectrum is essentially a plot of $z(\lambda)$ against λ, and can in principle tell us the abundances of chemical species in an exoplanet atmosphere.

Clouds and hazes

All of the solar system bodies with significant atmospheres have clouds or hazes (or both) in their atmospheres. We should not be surprised, therefore, that many exoplanet atmospheres show evidence of clouds and hazes. Throughout this work we use the following definitions: clouds are grey opacity sources in exoplanet atmospheres which absorb all wavelengths of light equally. Droplets of condensates which are much larger than the wavelength of optical and near-infrared light (i.e. $\gg 1\ \mu$m) are expected to act as grey absorbers in exoplanet transmission spectra. Condensates can form when gaseous species condense out of atmospheres to form liquid droplets or solid particles. Figure 1.3 shows condensation curves for various species plotted with model pressure-temperature profiles for various planetary atmospheres. Moving up from low altitudes (high pressures), the base of a cloud deck for a particular species forms where the lines cross. We define hazes as condensates which scatter radiation out of the line of sight in a wavelength-dependent manner - e.g. as Rayleigh scattering. Condensate particles which are smaller than one micron in size can scatter optical light in this way, and in the Solar System these small-particled hazes are often formed in upper atmospheres via photochemistry - chemical reactions caused by the absorption of stellar radiation that can combine volatile gases to form solid or liquid particles. High-altitude clouds and hazes can prevent the detection of gaseous species in exoplanet atmospheres because they can act as grey absorbers that block the transmission of light at all wavelengths, or as wavelength-dependent Rayleigh scatterers, that scatter stellar radiation out of the line of sight. Clouds and hazes can completely obscure absorption features, but patchier, thinner, or lower-altitude condensates may mute absorption features, but might not produce entirely flat spectra. For this reason, transmission spectroscopy is generally better at measuring the relative abundances of multiple atmospheric species. If condensates mute the features somewhat, it is more informative to compare the relative sizes of absorption features (rather than their absolute amplitudes). Often, however, the nature of the scattering/absorption in the transmission spectrum can tell us about the particle size of the haze or cloud (e.g. Wakeford & Sing 2015).

Secondary eclipses

If a planet is on a circular orbit, and it transits in front of its host star, it will also pass behind the star once per orbit. This occultation of the planet by the star is called a secondary eclipse and is illustrated in Figure 1.4. With this technique, we measure the flux from the star-plus-planet system just before the secondary eclipse

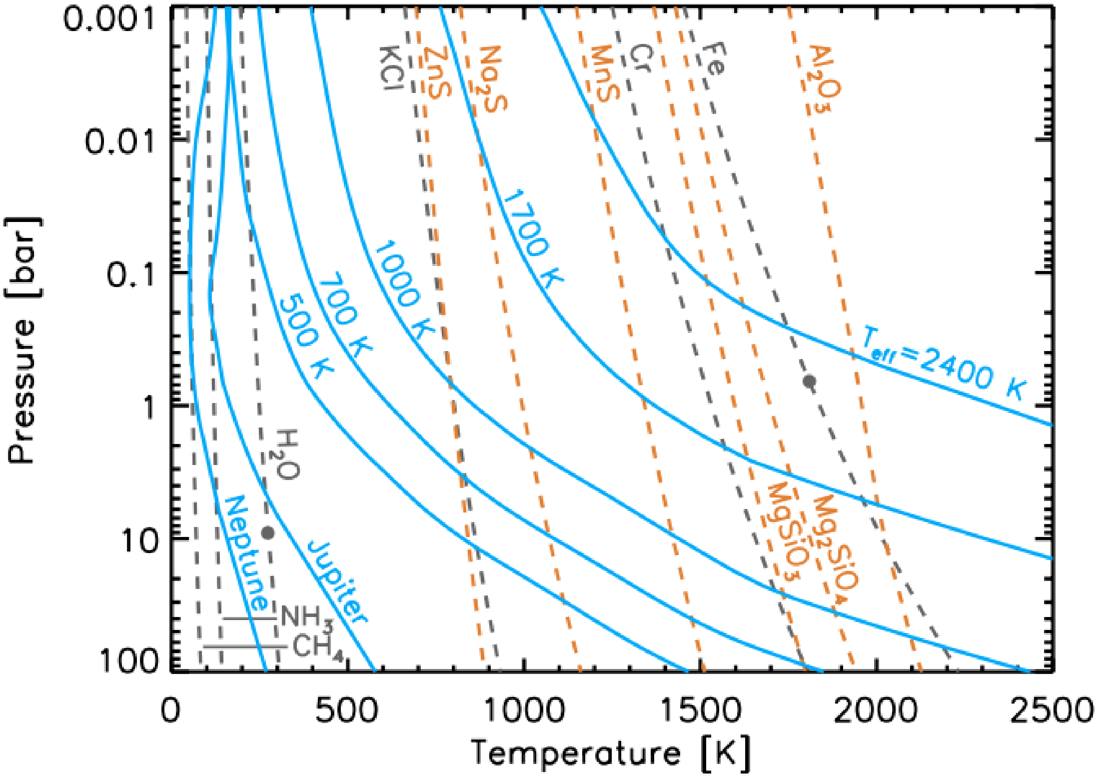

Figure 1.3: condensation curves (dashed lines) for various species assuming solar metallicity from Lodders (2003). Gray curves are for direct condensation, while orange curves are for condensates that form due to chemical reactions. Filled circles indicate a liquid-solid transition. Also plotted are P-T profiles for several planets. Figure from Marley & Robinson (2015)

and compare it with the flux from the star alone during the occultation. This strategy allows us to separate the flux from the planet and the star.

Secondary eclipse measurements at different wavelengths give valuable information about exoplanet atmospheres. For example, planetary flux measurements in the infrared constrain the thermal emission from various layers of the atmosphere (e.g. Deming et al. 2005, Charbonneau et al. 2005). Secondary eclipse observations at optical wavelengths measure how much starlight is reflected by the atmosphere (e.g. Evans et al. 2013). This information is especially helpful for understanding the temperature profiles of atmospheres and can be used to infer the presence of clouds and other atmospheric components.

Secondary eclipses are highly complementary to primary transit measurements, as it is possible to probe much deeper layers of exoplanet atmospheres. Due to the

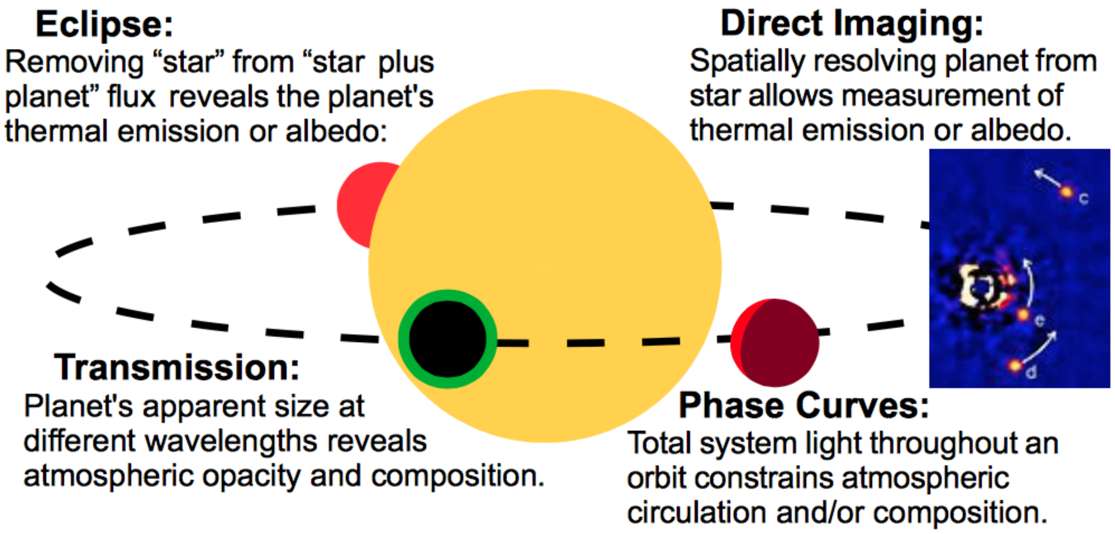

Figure 1.4: A schematic of four of the techniques used to study exoplanet atmospheres discussed here. Figure from Crossfield (2015)

longer path length at slant geometry (see Figure 1.2), primary transit observations only probe the topmost layers of atmospheres, whereas the more direct path length of secondary eclipse measurements means we can probe deeper atmospheric layers.

Phase curves

Throughout its orbit, different phases of a planet will face the observer on Earth, which causes the light curve of the star-plus-planet system to be slightly modulated by the varying flux received from the planet. This phenomenon is similar to the different phases of the moon and is illustrated in Figure 1.4. By taking a light curve covering substantial fractions of an orbit, we can measure the reflected light or thermal emission from varying longitudes of an exoplanet, to make brightness and temperature 'maps'. The light measured from an exoplanet is the combination of the reflected light and thermally emitted light. At optical wavelengths this is usually dominated by reflected light - perhaps from clouds - and thermal emission dominates at longer wavelengths. Hotter exoplanets (>2 000 K) are dominated by thermal emission. The disadvantage of this observing technique is that it requires a lot of observing time. However, it can provide much more information about an exoplanet atmosphere than a secondary eclipse, for example.

Hot Jupiters and hot Neptunes are expected to be tidally locked (Guillot et al. 1996), which means we can equate the orbital phase of the planet to the longitude of the centre of its hemisphere that faces the observer. Therefore for these tidally locked planets we can make hemispherically-averaged maps of the whole planet once every full orbit. For an exoplanet that orbits close to its host star, one might expect the hottest part of the atmosphere to be located directly under the substellar point, where it receives the highest irradiation. We can look for the hottest longitudinal location of an exoplanet by measuring where its phase curve peaks. If the hottest part is indeed at the substellar point the peak of the phase curve should correspond to the middle of the secondary eclipse. However, especially for tidally-locked exoplanets, there can be a large temperature contrast between the day and the night side of the exoplanet as one side permanently faces the star. The contrast should drive strong, planet-scale winds around the planet, which could shift the hottest part of the atmosphere around the planet before heat radiates away (Showman & Guillot 2002). Therefore searching for offsets in the position of the phase curve maximum can inform us about the dynamics of the planetary atmosphere - in particular the relative advective and radiative timescales (e.g. Knutson et al. 2007, and see Section 1.3.2). Phase curve observations can be directly compared to 3D models of exoplanet atmospheres which include the global atmospheric dynamics (e.g. Kataria et al. 2015). Figure 1.5 illustrates the physical quantities that can be measured from a phase curve.

High dispersion spectroscopy

One further way to study exoplanet atmospheres is by cross-correlating the spectra of model atmospheres with observed spectra at very high resolution ($\lambda/\Delta\lambda \sim 100\,000$). This technique can be used to identify many narrow absorption lines rather than individual lines which may be too weak to detect by themselves. Using CRIRES on the Very Large telescope (VLT), Snellen et al. (2010) made the first detection of an exoplanet atmosphere this way, by measuring a positive cross-correlation signal in the atmosphere of the hot Jupiter HD209458b that corresponded to absorption by

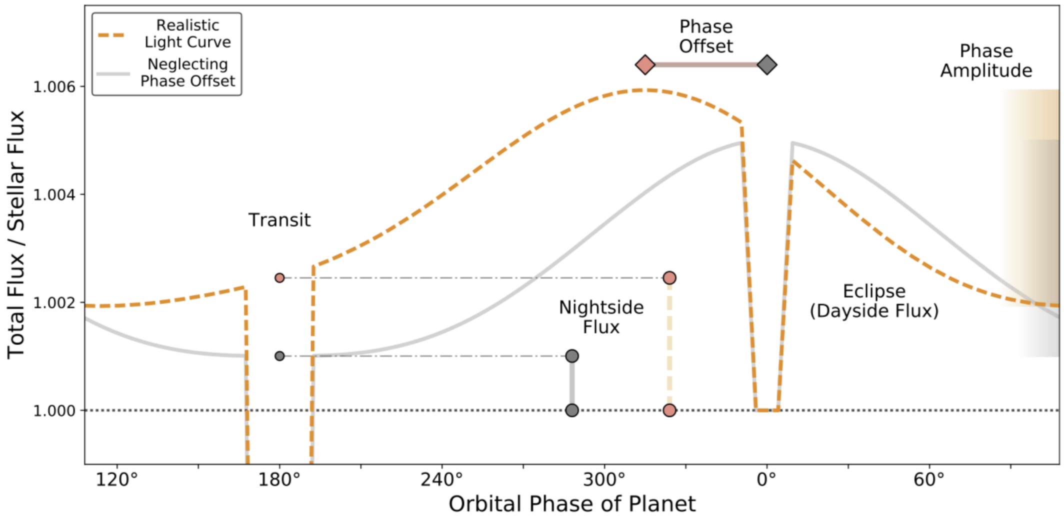

Figure 1.5: Schematic showing what can be learnt about exoplanet atmospheres from phase curve measurements. It shows model lightcurves for a transiting planet throughout an entire orbit. The grey model is for an atmosphere without a hotspot offset. To the lowest order, the planet's nightside flux is the eclipse depth minus the peak-to-trough phase amplitude. Figure and caption from Schwartz et al. (2017)

carbon monoxide - which has 56 absorption lines in their targeted wavelength range around 2.6 μm (see Figure 1.6). As well as detecting chemical species in exoplanet atmospheres, this technique can be used to measure the radial velocity of the planet itself, which will be manifested as shifts in the absorption signal in radial velocity space as the planet moves around its orbit - which is why the signal in Figure 1.6 has a diagonal trace. The same principle can be used to measure the spin rate of the planet and wind patterns (e.g. Snellen et al. 2014 and Snellen et al. 2010 respectively, and see Section 1.3.2).

1.2.2 Instrumentation

To measure a transmission spectrum, one should ideally take repeated measurements of the brightness of the system before, during, and after the transit event with a telescope. It is then possible to accurately measure the baseline stellar flux and compare it to the flux measured during transit. Ideally, a spectrograph is used to split the light into its constituent wavelengths and measure the wavelength-dependent transit depths simultaneously. However, in some cases (and at some wavelengths),

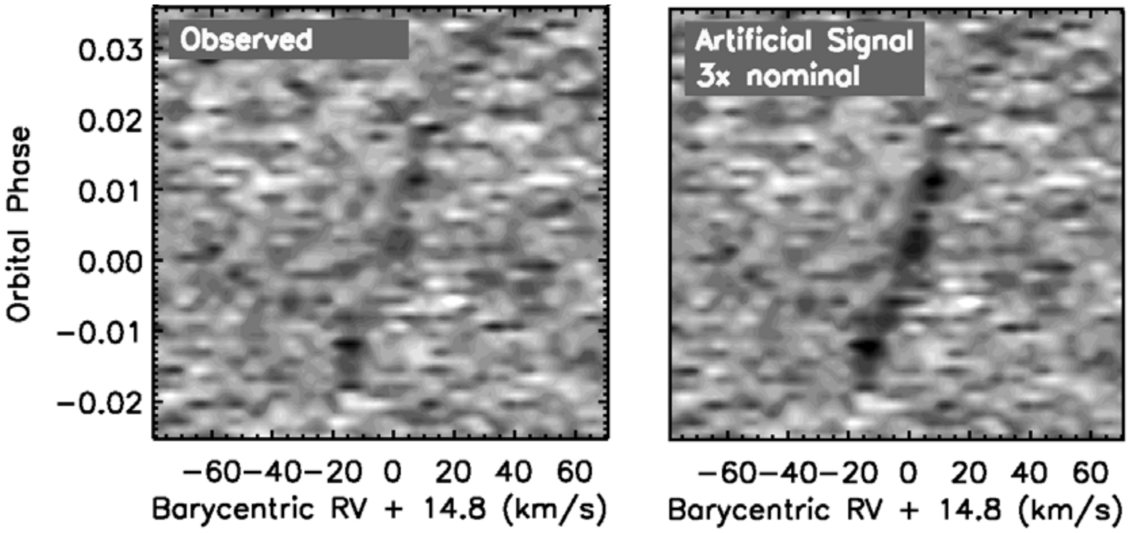

Figure 1.6: First detection of an exoplanet atmosphere using high-dispersion spectroscopy, for the hot Jupiter HD209458b. The left panel shows the real data: the individual spectra of the transiting planet at different orbital phases are cross-correlated with a synthetic atmospheric model with CO absorption which has been shifted in radial velocity space. Darker regions show stronger cross-correlation. The right panel shows a synthetic signal at 3× the observed amplitude for illustrative purposes. Figure from Snellen et al. (2010).

the available instruments do not allow this, and a low-resolution spectrum can be built up using different photometric filters and multiple transit measurements. Below is a brief introduction to the two main telescopes (and instruments) used in this work - the *Hubble Space Telescope* and the *Spitzer* space telescope - two of the most successful observatories used for exoplanet atmosphere studies. Future instruments which will be useful for the study of exoplanets and their atmospheres (including the James Webb Space Telescope) are discussed in Chapter 5.

The Hubble Space Telescope

The Hubble Space Telescope (HST) was launched in 1990 by NASA and is still working in low-Earth orbit (∼540 km), as of 2019. With a 2.4m-diameter primary mirror and five different instruments on board, it is one of the largest and most versatile space telescopes ever built. It was intended to be a ‘workhorse’ instrument - that is, a flexible, long-term observatory with multi-wavelength capabilities, which could answer a diverse set of science questions. To ensure its longevity and position at the cutting edge, NASA built it to be serviceable and have its instruments replaced by astronauts (see Figure 1.7).

Figure 1.7: Astronauts Andrew Feustel (left) and John Grunsfeld repairing the Hubble Space Telescope on a spacewalk of the STS-125 mission in May 2009, during which the WFC3 instrument was installed. Image from NASA

Even though it was launched before the first exoplanet discovery was confirmed, HST observations have been fundamental to the field of exoplanets, and exoplanet atmospheres in particular. For example, the first observation of an exoplanet atmosphere - sodium absorption in the transmission spectrum of HD2094558b - was made using the STIS spectrograph onboard Hubble, by Charbonneau et al. (2002). Because the telescope is in space, its observations do not suffer from absorption and scintillation from the Earth's atmosphere, as ground-based telescopes do. The lack of interference allows HST to make extremely precise photometric observations, and at wavelengths inaccessible from the ground - for example, at certain broad bands in the near-infrared, which are strongly absorbed by water molecules in the Earth's atmosphere. For these reasons, HST has been one of the most successfully employed instruments for exoplanet atmosphere studies, which often require precise, near-infrared spectroscopy. In this work, we used two instruments onboard HST: the Space Telescope Imaging Spectrograph (STIS), and the Wide Field Camera 3 (WFC3). Brief descriptions of each are given below.

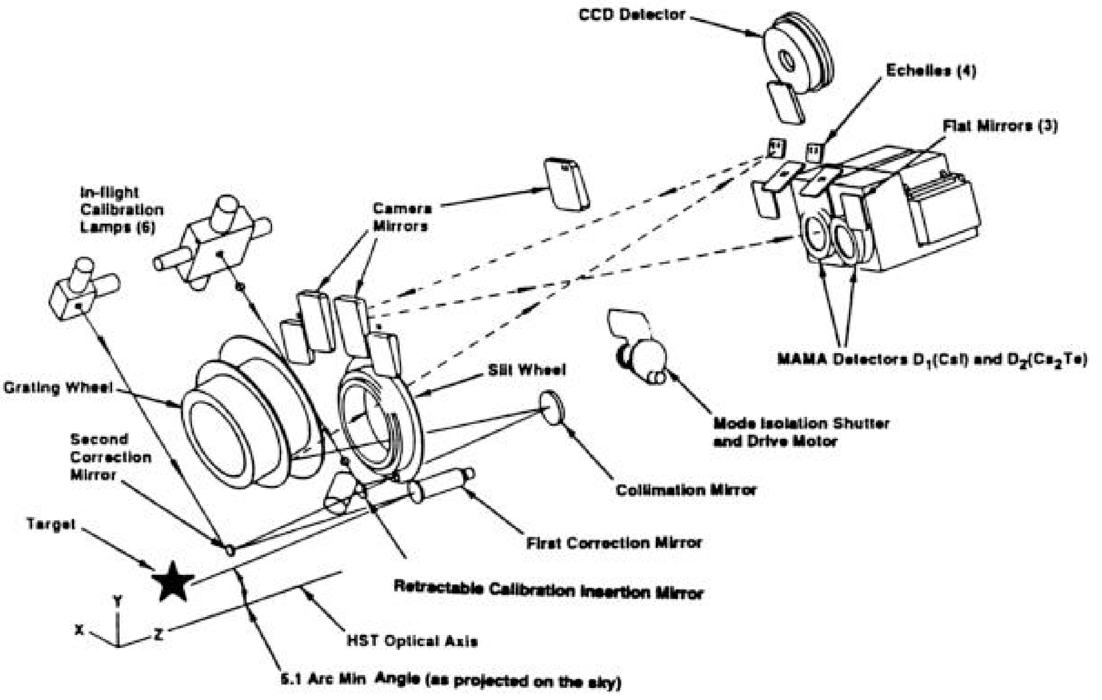

Figure 1.8: Optical bench design of HST/STIS, on board HST. Figure from STScI.

HST/STIS

STIS was installed on HST during Servicing Mission (SM) 2 in 1997. It is an imaging spectrograph which is sensitive to wavelengths from the UV to the near-infrared (1 150 to 10 300Å). Here I focus on its optical long-slit spectroscopy capabilities, which cover 3 000 - 10 300Å at medium-to-low resolution ($R \sim 500 - 17\,000$), which have been extensively used in exoplanet studies. The optical design of STIS is shown in Figure 1.8, and includes corrective optics to compensate for the spherical aberration of the primary mirror; a slit wheel; collimating optics; a grating wheel; and the detectors. The CCD detector is used for the optical spectroscopy, and the grating wheel contains first-order gratings which are used for long-slit optical spectroscopy. The G430L and G750L gratings have been most extensively used for exoplanet transmission spectroscopy. They cover wavelength ranges of 2 900 - 5 700Å and 5 250 - 10 270Å respectively, at $R \sim 500$. By taking two observations, one with each grating, one can efficiently observe a low-resolution spectrum from the optical (3 000Å) to the near infrared. Figure 1.9 shows an example raw spectrum of the exoplanet host star WASP-127 taken with STIS, using the G750L grism.

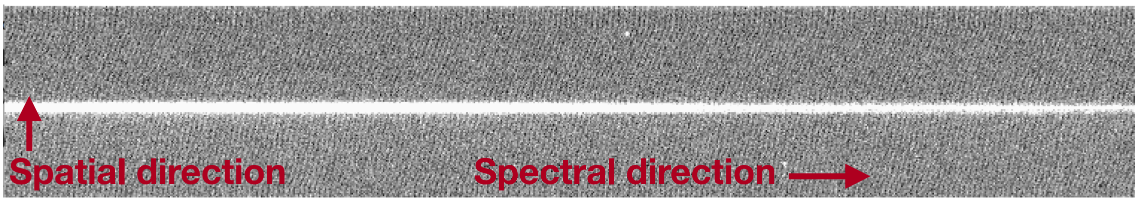

Figure 1.9: Example raw spectrum of WASP-127 from HST/STIS using the G750L grism. Data from HST proposal GO-14619 (P.I. Spake)

Charbonneau et al. (2002) used STIS to make the first detection of an exoplanet atmosphere, by measuring the transmission spectrum of HD209458b and detecting excess absorption in the sodium doublet at around 5 890Å. Since then, STIS has detected sodium and high-altitude condensates in the atmosphere of HD189733b (Pont et al. 2013); condensates on WASP-12b (Sing et al. 2013); sodium and condensates on HAT-P-1b (Nikolov et al. 2014); sodium on WASP-6b (Nikolov et al. 2014); and potassium and condensates on WASP-31b (Sing et al. 2015). Finally, in a landmark survey of 10 exoplanets, Sing et al. (2016) found sodium on WASP-17b; sodium and potassium on WASP-39b, sodium and condensates on HD209458b; and potassium and condensates on HAT-P-12b. In sum, these results from STIS have shown that hot Jupiter atmospheres are diverse, and that it is difficult to predict the presence of high-altitude condensates based on bulk properties like temperature and surface gravity. We present a transmission spectrum of the gas-giant WASP-127b using STIS G430L and G750L in Chapter 4.

HST/WFC3

WFC3 was installed on HST during SM4 in 2009. It is capable of imaging and spectroscopy from the UV to the near-infrared. Its large wavelength range (2 000 - 17 000Å), high sensitivity, high spatial resolution, large field of view and wide selection of spectral elements make WFC3 a very versatile instrument for astronomy. It has two channels - one for UV observations and one in the near-infrared, covering 8 000 - 17 00Å. The NIR channel, which we used in this work, has so far been the most useful of the two for exoplanet science, and it has also been used to observe some of the most iconic (and scientifically valuable) views of the universe - see Figure

1.10.

Figure 1.10: Left: the Horsehead nebula in the infrared, as seen by HST/WFC3. Right: the combined UV and near-infrared view of the Hubble Ultra Deep Field, which revealed 10,000 galaxies in a patch of sky one-tenth of the size of the full moon. The NIR observations were taken with HST/WFC3, and the UV were taken with HST/ACS. Images from STScI.

The optical design of WFC3 is shown in Figure 1.11, and it includes corrective optics to compensate for the spherical aberration of the primary mirror (as does STIS); a channel selection mirror which directs light to the IR channel; a filter wheel; and a HgCdTe infrared detector, which allows for non-destructive read-out and electronic shuttering. The IR channel has no mechanical shutter, and its filter wheel contains 15 photometric filters and two low-dispersion grisms: the G102 grism which covers 8 000 - 11 500Å at a resolution of $R \sim 210$, and the G141 grism which covers 10 750 - 17 000 at a resolution of $R \sim 130$.

Deming et al. (2013) pioneered the use of WFC3 in ‘spatial scan’ mode for exoplanet transmission spectroscopy. The method entails slewing the telescope in the spatial direction during an exposure, to spread the measured spectrum over many pixels to maximise the photon-collecting efficiency. With this technique they were able to observe convincing evidence of exoplanetary water (on HD209458b and XO-1b) for the first time with the G141 grism, which covers a broad band of water absorption lines centred around 1.4μm. An example of a WFC3+G141 raw spectrum in spatial scan mode is shown in Figure 1.12.

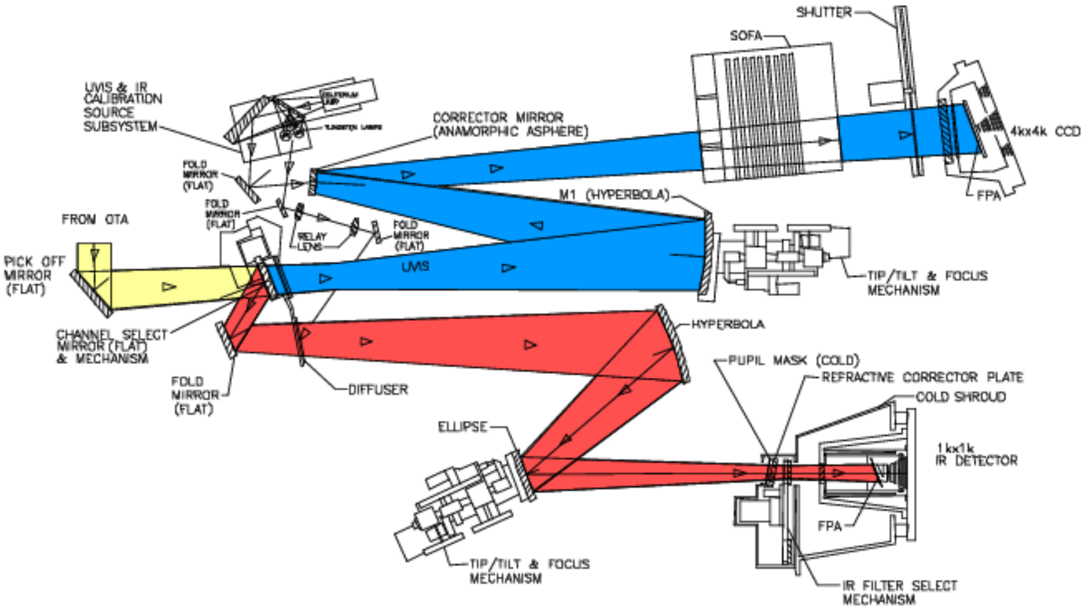

Figure 1.11: Optical bench design of WFC3, on board HST. Note the two separate channels - for infrared (bottom, red), and UV (top blue) observations. In this work only the infrared channel was used. Figure from STScI.

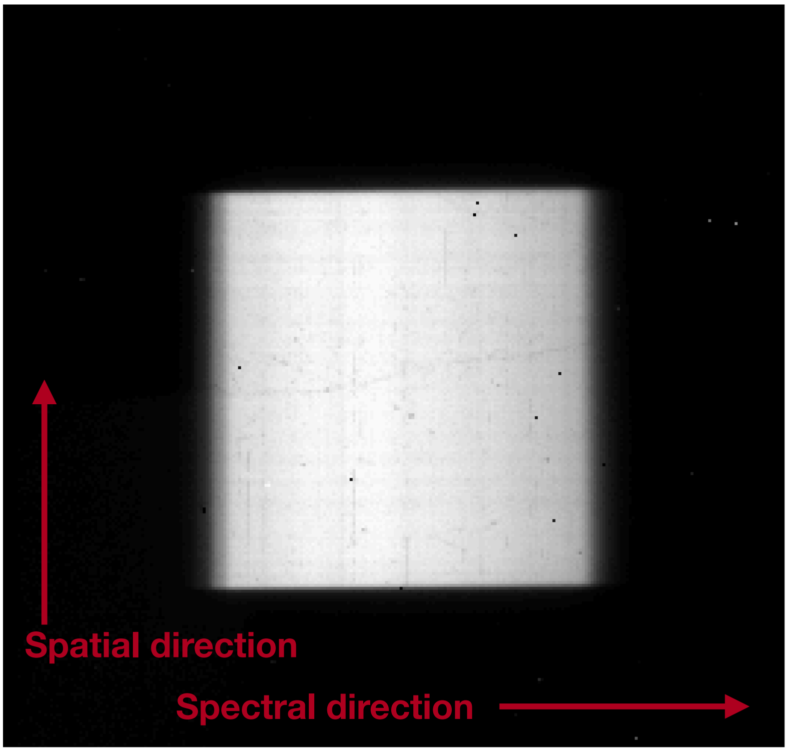

Figure 1.12: Example raw spectrum of WASP-127 from HST/WFC3 using the G141 grism. Data from HST proposal GO-14619 (P.I. Spake)

Since then WFC3 has been used to detect water in many giant exoplanets with transmission spectroscopy (e.g. Huitson et al. 2013; Mandell et al. 2013; McCullough et al. 2014; Wakeford et al. 2013; Wakeford et al. 2017; Kreidberg et al. 2015;

Evans et al. 2016); it made the first detection of an atmosphere of a Neptune-sized exoplanet (HAT-P-11b, Fraine et al. 2014); it detected clouds on a super-Earth (GJ1214b, Kreidberg et al. 2014); and made the first detection of water emission during the secondary eclipse of an exoplanet, implying the presence of a hot stratosphere on WASP-121b (Evans et al. 2017).

We used WFC3 in all three of the observational projects presented in this work: a transmission spectrum of WASP-107b taken with the G102 grism (Chapter 2); a phase curve of WASP-19b taken with the G141 grism (Chapter 3); and a transmission spectrum of WASP-127b taken with the G141 grism (Chapter 4).

The Spitzer space telescope

The Spitzer space telescope was launched in 2003 into a heliocentric, Earth-trailing orbit. It drifts away from the Earth at a rate of 0.1 AU per year, and in 2019 it was about 1.7 AU away. It is an infrared imaging telescope with three instruments on board (IRAC, IRS and MIPS), which cover a wavelength range of 3.6μm to 170μm in several broad band-passes. The scientific instruments were kept at a few degrees above absolute zero intil 2009 when the liquid helium supply ran out, leaving only the two shortest-wavelength channels of IRAC (centred on 3.6 and 4.5 μm) operational. Figure 1.13 shows the optical design of IRAC, which we used to observe two transits of WASP-127b (see Chapter 3). IRAC originally made use of four channels (including a 5.8μm and 8 μm channel), which each have a separate infrared detector.

Spitzer has been used to make significant exoplanet discoveries. For example, Deming et al. (2005) made the first detection of thermal emission from an exoplanet (the hot Jupiter HD209458b) using MIPS at 24 μm; Knutson et al. (2007) observed the first thermal phase curve of an exoplanet (the hot Jupiter HD189733b) with IRAC at 8 μm; and Gillon et al. (2017) used IRAC to help discover some of the seven temperate, Earth-sized planets in the TRAPPIST-1 system.

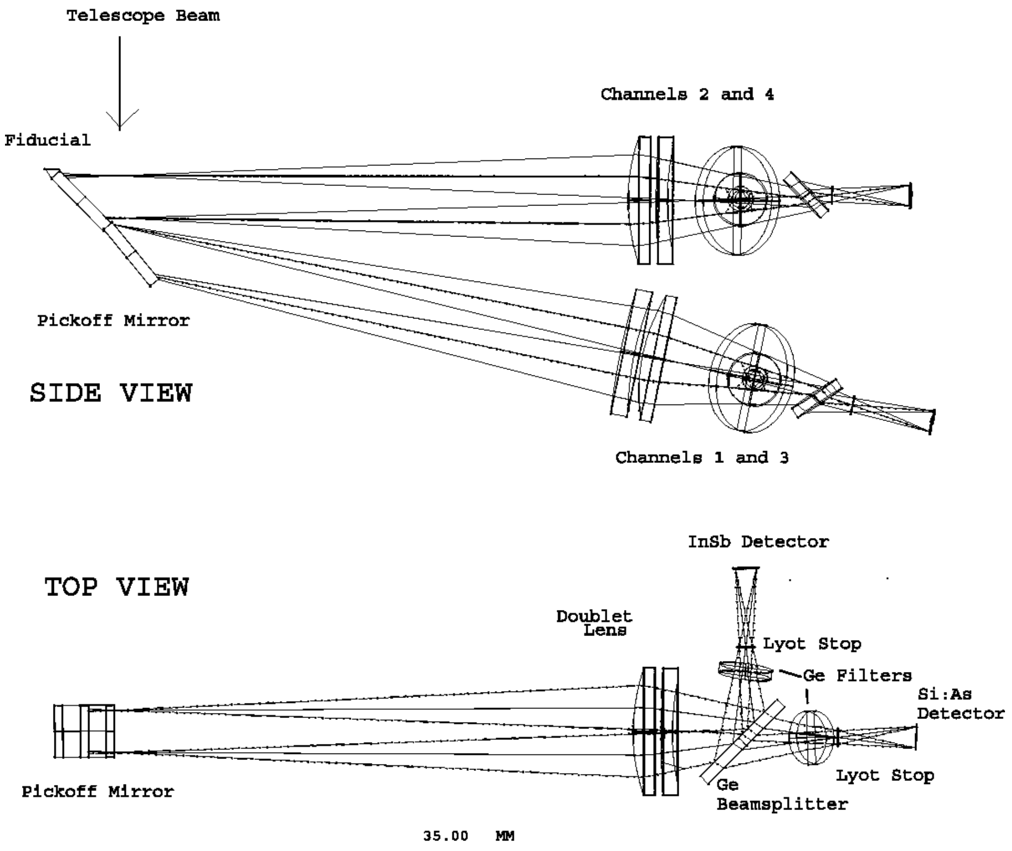

Figure 1.13: Optical bench design of IRAC, on board Spitzer. From Fazio et al. (2004)

1.2.3 Data analysis techniques

Once observations of exoplanets have been obtained, the data must be compared to theoretical models in order to measure the physical properties of the planet and robustly estimate the uncertainties on the parameters. The following sections describe two techniques used in this work to fit models to the data.

Markov Chain Monte Carlo techniques

Markov Chain Monte Carlo (MCMC) techniques are methods used to sample from - and thereby characterise - a target distribution that may be difficult to describe analytically, by taking random samples of the distribution. For our purposes, the target distribution that we want to characterise is a *posterior distribution*, which is the probability of a given set of physical parameters, given an observed dataset. If the posterior distribution is well characterised, it can be used to estimate the most likely value for a model parameter (or set of parameters), as well as estimate uncertainties on that value. It can also be used to investigate correlations or degeneracies between the estimated parameters. MCMC techniques combine two features: Monte-Carlo, and Markov chains. Monte Carlo techniques estimate properties of a distribution by taking random samples. They are useful when random samples are easy to draw, but describing the shape of the distribution analytically is difficult. Markov chains are sequences of samples where the current random sample is used as a stepping stone for the next, but the samples do not depend on the samples before the current one.

To calculate the posterior distribution, it is helpful to consider Bayes' theorem, which states:

$$p(\mu|D) \propto p(D|\mu) \times p(\mu), \tag{1.9}$$

where μ is the set of parameters and D is the data; $p(\mu|D)$ is the posterior distribution; $p(D|\mu)$ is the likelihood (the probablitiy of the data given the parameters); and $p(\mu)$ is the prior (the a-priori probability of μ). The prior can be used to encode already-known information into the posterior distribution. For example, when trying to measure the transit depth of an exoplanet, one can use the prior to tell the MCMC algorithm that the value of transit depth should be between zero and 1, as any other values would be unphysical. When an analytical expression for the likelihood is available, it can be combined with the posterior to derive the posterior distribution. However, this is often impossible, which is where MCMC techniques are useful.

The practical implementation of an MCMC consists of taking a long chain of samples, where each new sample is produced the following way: first, a proposal for the next sample is made by adding a small, random perturbation to the current sample. Next, the new proposal is either accepted as the next sample, or is rejected - and the current sample is kept. There are many ways to add random noise to the samples, and many different algorithms for deciding whether to accept or reject the proposal. Perhaps the simplest example is the Metropolis algorithm, which can be described by the following steps:

1. Choose a plausible starting value for the model parameters to start the chain
2. Create a proposed sample by adding random noise to the parameter values of the last sample. The noise comes from a symmetric proposal distribution centred on zero.
3. Compute the posterior (see Equation 1.9) at the current sample and the proposed sample
4. Accept the proposed sample if it has a higher posterior value than the current sample
5. If the proposed sample has a lower posterior than the current sample, then randomly choose to accept or reject it with a probability equal to the ratio of the two posterior values.
6. If the proposal is accepted, it becomes the next sample. If not, the next sample will be a copy of the first.
7. Return to step 2 until the chain has completed its defined number of steps

MCMC chains are typically hundreds or thousands of steps long, and since the initial guess for the starting parameters can be quite wrong, the first part of the Markov chain should be ignored - this is called ‘burn in’. Values for the model parameters can be calculated by taking the mean or median of all of the MCMC samples. A common practice for estimating the 1σ errors on the parameters is to find the range of values which contain 68% of all the samples.

Gaussian Processes

A Gaussian Process (GP) is the process of treating a finite set of data points as a sample from a multivariate Gaussian distribution, which is useful when attempting to model a dataset which doesn’t have a well-understood functional form. For example, time-series data from the Hubble Space Telescope are prone to strong systematic errors, for which some of the physical causes are poorly understood, and for which the functional forms are unknown. In this work (Chapter 4) we use GPs to model HST systematics and pass on uncertainties in their functional form to the final measurements of planetary parameters.

Suppose we have n observations of a dependent variable, y, that we assume can be described by a function of an independent variable, x, with Gaussian noise, so that

$$y = f(x) + \mathcal{N}(0, \sigma_n^2), \tag{1.10}$$

where $\mathcal{N}$ is a Gaussian distribution with mean 0 and variance σ_n^2. We could perhaps assume that $f(x)$ is a linear function, and use linear regression to find the posterior distribution of the gradient and y-intercept parameters, for example, which would be a *parametric* approach. Gaussian Processes, on the other hand, are non-parametric, and can be used to find the posterior distribution over the possible *functions*, $f(x)$, that are consistent with the observed data. The aim is not to find $f(x)$, but to be able to predict (with an uncertainty) any value of $y(x)$ within a certain range. The basic method is described below.

We can re-imagine our entire dataset of n observations as a single sample from an n-dimensional, multivariate Gaussian distribution. The simplest multivariate Gaussian to visualise is the two-dimensional case (Figure 1.14).

The shape of the surface will be controlled by the covariance function, $k(x, x')$, which relates one variable (x) to another (x'). If their covariance is zero, then any horizontal cross-section of the shape will give a perfect circle. If they have a covariance greater than zero, the cross-sections will be more oval shaped, which means there is some correlation between the two variables.

Although Gaussian Processes are much more flexible than linear regression, for example, it is still necessary to make some assumptions about the functional form of

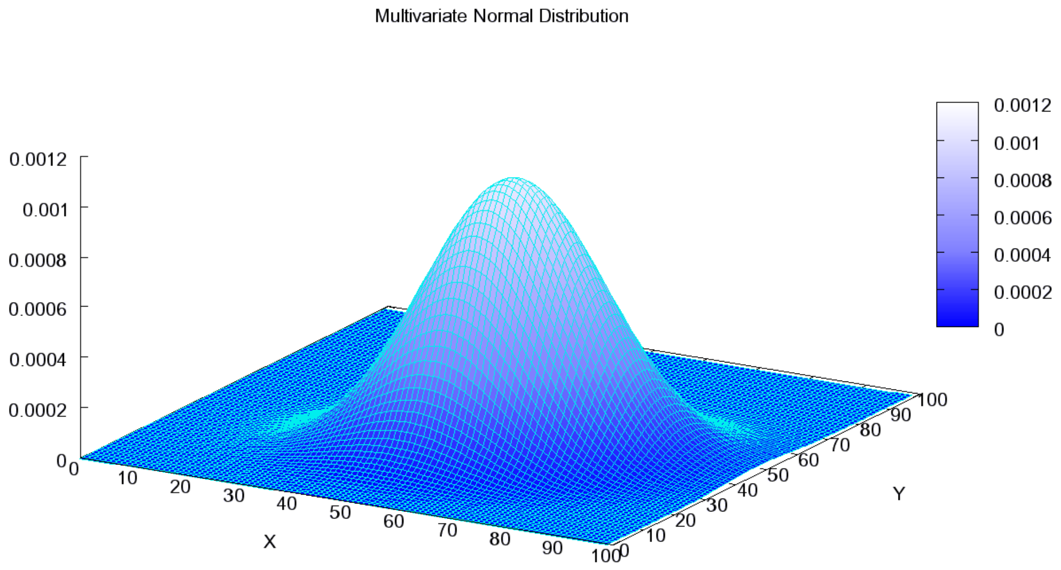

Figure 1.14: Two-dimensional Gaussian distribution, from Wikipedia

the covariance function (or kernel). One popular choice is the squared-exponential,

$$k(x, x') = \sigma_f^2 \exp\left(\frac{-(x - x')^2}{2l^2}\right), \tag{1.11}$$

where σ_f^2 is the maximum covariance - which will be higher for data sets which cover a broad range on the y-axis. If $x \approx x'$ then $k(x, x')$ approaches its maximum, and the y values of x and x' will be similar. This is useful when we want the model to vary smoothly. If x is far from x', then $k(x, x')$ approaches zero; more distant observations will have less of an effect, and the effective distance will be set by the length parameter, l.

To mathematically describe a Gaussian Process, we should consider that for two random vectors, $\boldsymbol{a}$ and $\boldsymbol{b}$, the joint mean ($\boldsymbol{\mu}_{a,b}$) and joint covariance ($\boldsymbol{\Sigma}_{a,b}$) can be written in block matrix form:

$$\boldsymbol{\mu}_{a,b} = \begin{bmatrix} \mu_a \\ \mu_b \end{bmatrix} \tag{1.12}$$

and

$$\boldsymbol{\Sigma}_{a,b} = \begin{bmatrix} k(a,a) & k(a,b) \\ k(b,a) & k(b,b) \end{bmatrix}. \tag{1.13}$$

And if $\boldsymbol{a}$ and $\boldsymbol{b}$ are jointly normally distributed, then the conditional distribution for $\boldsymbol{b}$ given $\boldsymbol{a}$ is

$$\boldsymbol{y}_{b|a} \sim \mathcal{N}(\boldsymbol{\mu}_{b|a}, \boldsymbol{\Sigma}_{b|a}) \tag{1.14}$$

which is defined by the conditional mean,

$$\boldsymbol{\mu}_{b|a} = \boldsymbol{\mu}_b + k(b,a)k(a,a)^{-1}(\boldsymbol{a} - \mu_a) \tag{1.15}$$

and the conditional variance,

$$\boldsymbol{\Sigma}_{b|a} = k(b,b) - k(b,a)k(a,a)^{-1}k(a,b) \tag{1.16}$$

The key to the predictive power of a Gaussian Process is to let $\boldsymbol{a} = y_{1,2,...n}$ and $\boldsymbol{b} = y_{n+1}$, where $y_{1,2,...n}$ are the observed data points and y_{n+1} is our prediction for a new data point consistent with the data. Its expected value can then be calculated (the conditional mean), as well as its uncertainty (from the conditional variance). If this calculation is performed for many points in x within a finite range, it can flexibly estimate the shape of the dataset with robust uncertainties. The calculations above are solvable if we can calculate the covariance function - for example by assuming it takes a squared-exponential form (many other forms can be chosen, some of which vary less smoothly). Gaussian Processes can be combined with a model-fitting procedure, like MCMC, to marginalise over the quantities which describe the chosen covariance function, and create a posterior distribution in functional space.

1.3 Big-picture questions and the state of the art

What have we learnt so far about exoplanet atmospheres? Which science questions can we try to answer with the indirect observational techniques discussed, and our available technology? I will focus on three questions at the forefront of our understanding: How has atmospheric escape sculpted the population of exoplanets that we observe today? How is heat transported around the very hottest, tidally locked exoplanets? Where and how do clouds form in exoplanet atmospheres? These questions are each linked to the three observational projects discussed in this work (Chapter 2, Chapter 3, and Chapter 4, respectively).

1.3.1 Where and how do clouds form in exoplanet atmospheres?

The development of 1-D radiative-convective models

Only by comparing observations to models can we infer atmospheric properties like temperatures, chemical abundances, and the presence and composition of clouds, for exoplanets. If we assume an atmosphere is isothermal (the same temperature at every altitude) and cloud-free, it is possible for example, to estimate atmospheric temperature and mean molecular weight from considering slopes in a transmission spectrum caused by Rayleigh scattering, as in Lecavelier Des Etangs et al. (2008). However, in reality, no planetary atmosphere is so simple. One branch of exoplanet atmosphere models encompasses one-dimensional, radiative transfer models which are often used to estimate planet- or longitudinally-averaged temperature and chemical profiles, that are invaluable to transmission spectroscopy. By using approximations to the radiative transfer problem, it is possible to calculate analytical temperature-pressure profiles for exoplanets, and this has been done several times for cloud-free hot Jupiters, for example by Hansen (2008), Guillot (2010) and Parmentier & Guillot (2014). However, often the complex atmospheric physics involved even in one-dimensional models must be modelled numerically.

The basic physics behind most 1D models involves numerically calculating a temperature-pressure (TP) profile. Certain assumptions are often made: for example, that the atmosphere is in hydrostatic and chemical equilibrium, and the atmosphere is cloud-free. Under the chemical equilibrium assumption, the chemical composition of a parcel of gas only depends on its temperature, pressure, and elemental abundances (which are often assumed to be Solar-like for gas giant exoplanet atmospheres). The chemical composition at a given temperature and pressure can be calculated by minimising the "free" chemical potential energy in the system (called the Gibbs free energy) - by finding where the rates of exothermic and endothermic reactions equalise and a steady state is reached (e.g. Madhusudhan et al. 2016). It is possible to self-consistently solve for the temperature-pressure profile of an atmosphere in chemical and hydrostatic equilibrium by simultaneously solving for the radiative transfer though the atmosphere; its chemistry; and vertical mixing - and then iterating the process in time. The temperature and pressure at a given altitude will affect the chemistry there, and in turn the chemical composition will affect the radiative transfer through that region due to the varying opacities of different gases at different wavelengths. Many iterations are performed until the model reaches a steady state. At this point a model transmission spectrum can be produced using the final PT profile, and performing another radiative-transfer calculation, this time along the observer's line of sight (at the slant geometry previously discussed).

Some of the earliest models in this vein assumed a cloud-free atmosphere in chemical equilibrium (e.g. Seager & Sasselov 2000). However, further investigations with 1D models have shown that non-equilibrium processes like vertical transport and photochemistry are important in the observed exoplanet population (e.g. Venot et al. 2012, Zahnle & Marley 2014 and Drummond et al. 2016). This should not be surprising, perhaps, since evidence of disequilibrium processes has been observed on Jupiter and Saturn since the 1970s (e.g. Beer 1975; Fink & Larson 1978). In addition, the observational and theoretical evidence of the importance of clouds in almost all exoplanet atmospheres has become overwhelming, and so they can rarely be ignored (see next section).

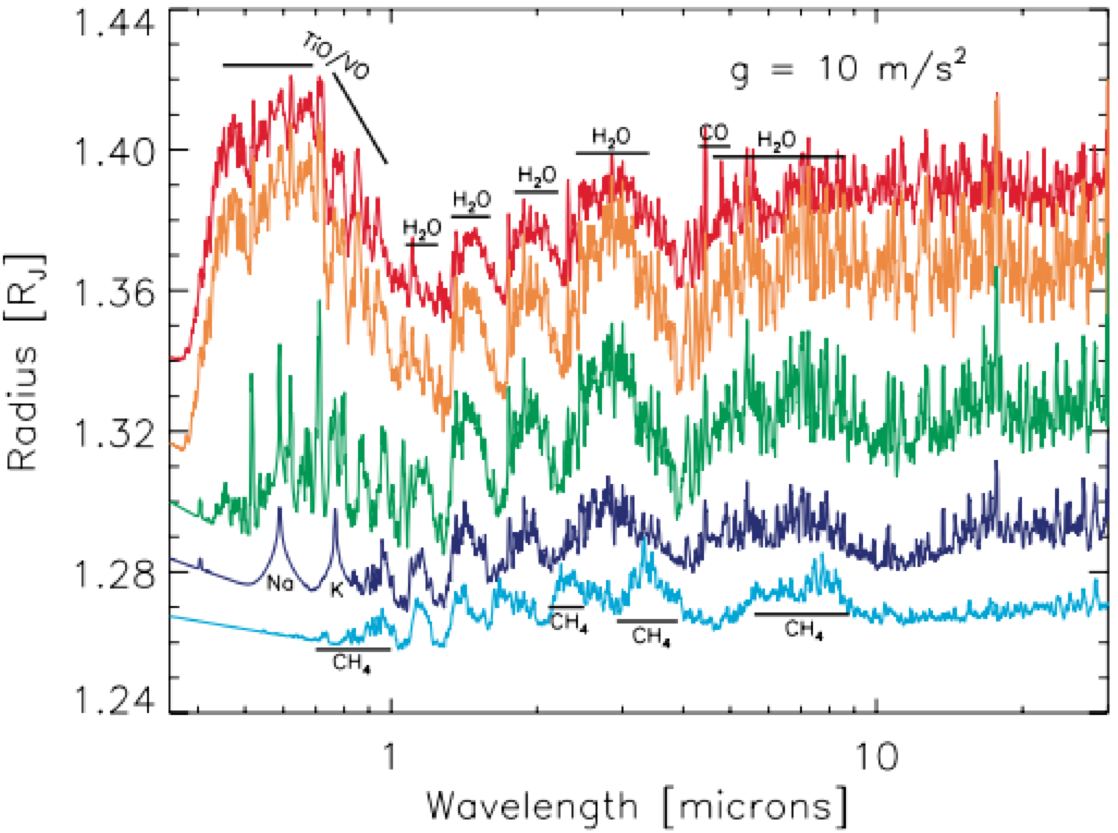

Figure 1.15: Transmission spectra (planet radius vs. wavelength) for isothermal model atmospheres with a gravitational acceleration of 10 ms^{-2}. Models have effective temperatures $T = 2\,500$, $2\,000$, $1\,500$, $1\,000$, and 500 K, from top to bottom and assume chemical equilibrium. Prominent absorption features from different species, which appear as increases in the planetary radii, are labeled. Figure from Fortney et al. (2010)

There are two main ways to use atmospheric models - the forward modelling approach and the retrieval approach. Forward models take a set of known or assumed planetary parameters (like the level of stellar irradiation, the planet radius and gravity), and self-consistently solve for the temperature-pressure profile and chemistry to generate model spectra. The important physical- and chemical processes are assumed to be known a priori. For example, Fortney et al. (2010) used 1D models of hot Jupiter atmospheres to predict chemical mixing ratios which could be observed in transmission spectra (Figure 1.15). This approach is invaluable for investigating atmospheric physics under controlled conditions, and it has been useful both for predicting yet-unseen observable features, like strong alkali absorption in hot Jupiters (Seager & Sasselov 2000), and for comparison with observed spectra, for example by Moses et al. (2011) and Goyal et al. (2018, 2019).

However, forward models have little ability to interpret observed exoplanet spectra in a statistically robust way. The problem is that forward models with self-consistently solved TP profiles and chemistry can qualitatively match observations, but the computational expense of calculating each model is too high to compare a large number of models against the data. Therefore it is difficult to explore vast areas of parameter space or any degeneracies that may exist between the different model parameters. Some early detections of molecular absorption and temperature inversions in exoplanet atmospheres, which were based on the few channels of infrared photometry available and compared with forward models, have since been revised (e.g. Barman 2007, Tinetti et al. 2007, Knutson et al. 2008, Swain et al. 2008).

Recent developments in observing techniques, atmospheric modelling, and the application of statistical methods to exoplanets, have borne a new approach to interpreting exoplanet spectra - which are now typically of higher precision and spectral resolution. The "retrieval" approach attempts to efficiently explore a large parameter space and formally fit models to the data in order to estimate atmospheric parameters and their uncertainties. This is achieved by *parametrising* the computationally-expensive physics of atmospheric models so that a large number of models can be computed and compared to the data (typically on the order of tens of thousands of models). For example, a 6-parameter, analytical TP profile described by Guillot (2010) can be calculated thousands of times faster than modelling the radiative-transfer physics of a self-consistent TP profile. The individual models may not be self-consistent, but by running thousands of models over a broad parameter space we can explore the range of scenarios consistent with the data, and we no longer need to assume that the underlying physical and chemical processes are known. For example, there is no need to assume hydrostatic- and chemical equilibrium conditions, because the TP profiles and chemistry are directly estimated from the data.

By combining parametrised models with advanced statistical inference methods, like Markov chain Monte Carlo (e.g. Benneke & Seager 2012, see Section 1.2.3) and Nested Sampling (e.g. Benneke & Seager 2013) techniques, the posterior probability distributions of all the model parameters can be calculated, from which we can see model degeneracies, and estimate the best-fitting parameters and uncertainties. Atmospheric retrievals had previously been used to study the Earth's atmosphere (e.g. Rodgers 2000), and Solar System planets (Irwin et al. 2008), and were first applied to exoplanets by Madhusudhan & Seager (2009). Since then they have become standard in interpreting exoplanet spectra (e.g. Line et al. 2013, Waldmann et al. 2015, Barstow et al. 2017 Evans et al. 2018, Wakeford et al. 2018).

Clouds and hazes in exoplanet atmospheres

Some of the earliest models of exoplanet atmospheres considered the effects of clouds on transmission spectra (Burrows & Sharp 1999). Observational evidence of clouds and hazes in exoplanet atmospheres within the exoplanet literature is now plentiful. It can be seen in Rayleigh scattering in their optical transmission spectra, for example in the hot Jupiters WASP-12b (Sing et al. 2013), WASP-31b (Sing et al. 2015), WASP-6b (Jordán et al. 2013; Nikolov et al. 2015), and HAT-P-18b (Kirk et al. 2017). It is also manifested as smaller amplitude absorption features than expected for clear atmosphere models, or entirely flat spectra, presumably due to gray absorbing clouds with large particle/droplet sizes. For example, in the flat spectra of the warm Neptune GJ 436b measured with HST/WFC3 (Knutson et al. 2014); of the super-earth GJ 1214b, measured from the ground in the optical Bean et al. (2010), and in the infrared from space (Kreidberg et al. 2014; Désert et al. 2011); of the rocky exoplanet GJ 1132b (Diamond-Lowe et al. 2018) and the extremely inflated hot Jupiter WASP-52b (Kirk et al. 2016) - both measured from the ground. Using High Dispersion Spectroscopy from the ground, Crossfield et al. (2011) also find no signs of molecular absorption in the atmosphere of GJ 1214b, which suggests clouds are present, but they are able to rule out many atmospheric models. Clouds can also be inferred from albedo (reflectivity) measurements from secondary eclipses (Evans et al. 2013). On the other hand, a few hot Jupiter atmospheres appear cloud-free and clear, like WASP-19b (Huitson et al. 2013) and WASP-96b (Nikolov et al. 2018).

Besides transiting exoplanets, evidence for clouds has been seen in directly imaged exoplanets and brown dwarfs, for example in the varying thermal profile of a free-floating, directly imaged planet (Biller et al. 2015). Clouds also flatten the emission spectra of these bodies and mute absorption features (e.g. Tsuji 2002; Tsuji 2005 and Tsuji et al. 2004). Including simple cloud schemes in the models of directly imaged exoplanets improves the consistency of the retrieved planetary radii with those estimated from planet evolutionary track models, which has been a problem in the past (e.g. Currie et al. 2011; Madhusudhan et al. 2011; Biller et al. 2015).

Observations of transiting exoplanet atmospheres are expensive because the measurements take hours to make, in order to cover the entire transit and stellar baseline flux (exoplanet phase curve observations can take *days* to cover entire planetary orbits). Therefore, building a large sample of diverse, characterised exoplanets is a monumental, collective endeavour. The first major success in this vein was the first detection of an exoplanet atmosphere by Charbonneau et al. (2002) using HST, and since then many milestones have been reached, including the first detections of exoplanet atmospheres from the ground (Redfield et al. 2008; Snellen et al. 2008), and numerous measurements of atmospheric abundances of different chemical species on exoplanets (e.g. potassium on WASP-17b, Sedaghati et al. 2016). After nearly two decades, a new era of comparative exoplanetology has arrived. In the first large, comparative study of exoplanet atmospheres, Sing et al. (2016) found a diverse spectrum of clear to cloudy atmospheres in their survery of 10 hot Jupiters, using HST and Spitzer observations. They showed that clouds were responsible for the muted water features observed in exoplanet atmospheres, rather than low water abundances; and that it is difficult to predict the presence of clouds or hazes based on properties like temperature and surface gravity alone.

Part of the problem with our understanding of cloud formation is that clouds are difficult to create in the lab, and they involve complex and poorly understood microphysics which is challenging to model. However, great efforts have been made in this area of theory. Ackerman & Marley (2001) developed early, relatively simple models of clouds in exoplanet atmospheres. The microphysics is paramaterised by a sedimentary efficiency parameter, $f_{\rm sed}$, which is tuned to fit observations - so the models offer little predictive power. Morley et al. (2013) developed detailed cloud models for warm sub-Neptune transiting exoplanets, and Helling et al. (2006, 2008, 2013) modelled the cloud microphysics for a range of exoplanet and brown dwarf atmospheres. There is still a lack of enough high-quality atmosphere observations to validate these complex models. Also, some have recently incorporated clouds into 3D models of exoplanet atmospheres (e.g. Lee et al. 2016, Parmentier et al. 2016, Lines et al. 2018). Recently, there have been hints of emerging trends between intrinsic planet properties and the prevalence of clouds. For example, Crossfield & Kreidberg (2017) find that for Neptune-sized exoplanets, those with warmer equilibrium temperatures or lower bulk densities tend to have less cloudy atmospheres. Still, for most types of exoplanet, it remains difficult to predict which planets will be cloudy before directly observing their atmospheres. It is still necessary to observationally classify exoplanets as clear or cloudy before we can attempt to measure, for example, the relative abundances of the gaseous species in their atmospheres. It is also important to select highly favourable targets that are likely to show atmospheric absorption features even with some modest cloud or haze, like WASP-127b (See Chapter 4).

1.3.2 How is heat transported around tidally-locked exoplanets?

Exoplanets are 3D objects, and we must understand how their atmospheric temperatures, wind speeds, and compositions vary with latitude, longitude, and altitude, if we want to interpret our observations, which target limited regions of their atmospheres. For example, transmission spectroscopy measures light filtering through an exoplanet's terminator, and secondary eclipse measurements are a sum of the dayside hemisphere emission. We cannot assume that an abundance measurement taken from a transmission spectrum is representative of the entire planet. A large day-night temperature contrast could condense some species on the cooler night side of an exoplanet, depleting them from the upper atmosphere when 1D equilibrium models may predict them to be present in transmission spectra. Even with a hot night side, heavy particles can settle out of an atmosphere if the vertical wind speeds are low, and, as Parmentier et al. (2013) show, horizontal and vertical wind speeds are linked. Knowing which exoplanets are able to efficiently transport heat from the day to the night side is one step towards effectively modelling exoplanet atmospheres in 3D.

We can understand the first-order basics of heat transport in exoplanet atmospheres by considering two simplified timescales which paramaterise the radiative cooling and heat transport efficiency. The radiative timescale is defined as the it time takes for a slab of atmosphere above a pressure level P to cool to $1/e$ its initial temperature via radiative cooling, if stellar heating were turned off. This can be estimated by considering the total thermal energy stored in this slab of the atmosphere, and by using the Stefan-Boltzmann law ($F = \sigma T^4$) to estimate the flux (F) emitted to space per unit area at the top of the atmosphere, assuming it acts as a black body. In this simplified scenario, the radiative timescale can be approximated as

$$\tau_{\rm rad} \sim \frac{P}{g}\frac{c_p}{4\sigma T^3} \tag{1.17}$$

(e.g. Showman & Guillot 2002), where P is the planet's orbital period, g its surface gravity, $c_{\rm p}$ is the specific heat capacity of the atmosphere and σ is the Stefan-Boltzmann constant. Because $\tau_{\rm rad}$ is proportional to both P and T^{-3}, it is very short for hot planets on short orbits. The second important timescale is the advective timescale, $\tau_{\rm adv}$, which is the characteristic time it takes to move a parcel of gas,

$$\tau_{\rm adv} \sim \frac{R_{\rm p}}{U} \tag{1.18}$$

(from Showman & Guillot 2002 and Seager et al. 2005), where $R_{\rm p}$ is the radius of the planet and U is the characteristic wind speed in the atmosphere.

It is the *ratio* of τ_{rad} to τ_{adv} that can tell us how quickly heat is transported around the planet before being radiated into space. For example, when $\tau_{\mathrm{rad}} << \tau_{\mathrm{adv}}$, the planet re-radiates the heat deposited onto its dayside relatively quickly - before it can be dynamically transported to the night side. This will result in large day-night temperature contrasts, which is manifested as large phase-curve amplitudes; and small, westward offsets in the peak of the phase curve. Conversely, when $\tau_{\mathrm{adv}} << \tau_{\mathrm{tau}}$, the heat is better recirculated and the temperature of the atmosphere will be more homogeneous. This will give a lower-amplitude phase curve, and a larger, westward hostspot offset. These intuitive predictions have been reproduced in results of 3D radiative-hydrodynamic codes, which simulate the fluid dynamics over the entire planet. For example, Showman & Guillot (2002); Dobbs-Dixon & Lin (2008); Menou & Rauscher (2009); Heng et al. (2011); Mayne et al. (2014); and Amundsen et al. (2016) clearly show planet-wide jets of wind, and hotspot offsets for highly-irradiated exoplanets.

High- resolution exoplanet spectra revealing Doppler shifting of atomic absorption lines has been detected on HD209458b (Snellen et al. 2010) and HD189733b (Louden & Wheatley 2015), as well as measurements of the emission as a function of orbital phase (e.g.Knutson et al. 2012; Zellem et al. 2014), have since confirmed these theoretical predictions. However Dang et al. (2018) recently reported a westward shift in the location of the hot spot on CoRoT-2b, which contradicts the eastward shifts unanimously predicted by current 3D models. The eastward shift could be caused by magnetic effects; partial cloud coverage; or because the planet is not tidally locked, as was expected.

Secondary eclipse measurements tell us the temperature profile of the dayside of the planet, which we can use to estimate how much heat gets transported around the planet. For example, Evans et al. (2017) detected water vapour emission from the hot Jupiter WASP-121b using spectroscopic secondary eclipse measurements from HST's WFC3 (see Figure 1.16). The 'glowing' water emission suggests that the upper layers of the atmosphere are hotter than the deeper layers - otherwise the water feature might be seen in absorption as the cooler upper layers absorbed radiation at those wavelengths. Besides the emission features, the measured spectrum of the planet followed the general shape of a black body spectrum, so the authors were able to esitmate the temperature profile of the dayside of the planet. They found high temperatures of around 2 700K, which suggests that heat is not efficiently transported around the planet before it radiates away from its dayside.

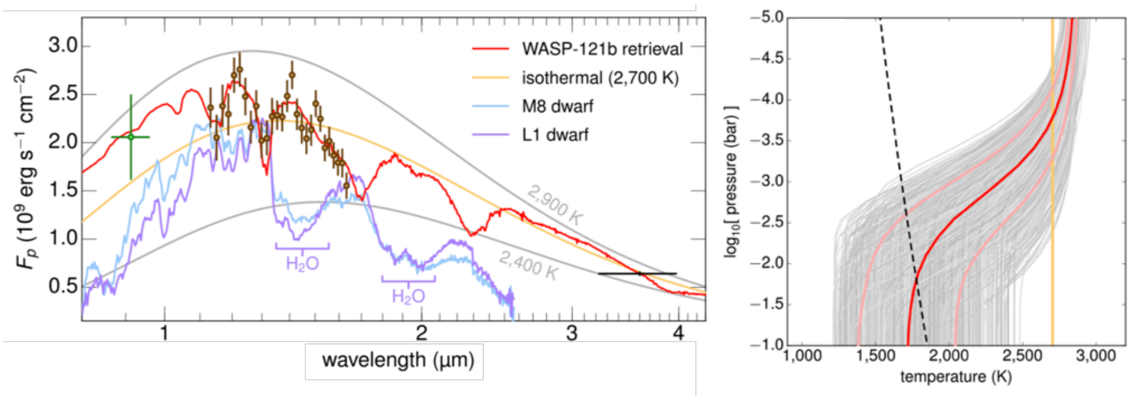

Figure 1.16: Left panel: thermal emission spectrum of the dayside of the hot Jupiter WASP-121b, measured with the Hubble Space Telescope's WFC3 instrument. The fact that water is seen in emission suggests that WASP-121b's atmosphere has a temperature inversion. The PT profile retrieved from this data is shown on the right. The high temperatures of around 2 700K suggests that heat is not efficiently transported around the planet. From Evans et al. (2017)

Figure 1.17 shows a phase curve of the canonical exoplanet HD189733b, one of the earliest photometric exoplanet phase curves, taken with Spitzer/IRAC's 4.5 micron channel. Since then, 13 exoplanets have had their thermal phase curves measured with Spitzer: the hot Jupiters HD209458b (Zellem et al. 2014), HD189733b (Knutson et al. 2012), υ And b (Crossfield et al. 2010), WASP-12b Cowan et al. (2012), WASP-19b (Wong et al. 2016) and WASP43b (Stevenson et al. 2017) have eastward hotspot offsets greater than 10° in Spitzer bandpasses; and the hot Jupiters HAT-P-7b (Wong et al. 2016), HD149026b (Knutson et al. 2009), WASP-14b (Wong et al. 2015), WASP-18b (Maxted et al. 2013) and WASP-103b (Kreidberg et al. 2018a) have either small ($< 10°$) or non-detected offsets. Of the smaller planets observed, Stevenson et al. (2012) found no significant hotspot offset on GJ436b (a warm Neptune), but interestingly, on the super-Earth 55 Cancri e Demory et al. (2016) found a 41±12° eastward offset combined with a large day-night temperature contrast. The 55 Cancri e data are consistent with either an optically thick atmosphere with heat recirculation confined to the planetary dayside, or a molten lava surface with little atmosphere.

To date, three exoplanets have had their spectroscopic phase curve measured by HST WFC3: WASP-43b, Stevenson et al. 2014; WASP-18b Arcangeli et al. 2019; and WASP-103b Kreidberg et al. 2018a. We present a fourth in Chapter 3. Additionally, Armstrong et al. (2016) detected variability in an exoplanet atmosphere for the first time, by detecting changes in the peak offset of HAT-P-7b's optical phase curve. The spectral variation of thermal phase curves is shaped by molecular features. Inside a molecular absorption band, a phase curve probes low pressures (high altitudes) while probing deeper outside a molecular absorption band (Showman et al. 2009; Kataria et al. 2015). Measuring the phase curve spectroscopically probes multiple pressures simultaneously. The observations discussed here cover the extremes of the hot gas-giant equilibrium temperature range, from $T_{\mathrm{eq}} \sim 700$ to 3 000 K. Note also that many more exoplanets have had their optical phase curves measured with Kepler, and 6 of them have had a hotspot offset detected. These observations are reviewed in Parmentier & Crossfield (2018).

Figure 1.18 summarises the hotspot offsets and amplitudes measured from exoplanet phase curves so far. We note that the amplitude, A_{F}, is defined here as the *relative* difference between the maximum and minimum of the phase curve, or

$$A_{\mathrm{F}} = (F_{\mathrm{p,Max}} - F_{\mathrm{p,Min}})/F_{\mathrm{p,Max}} \tag{1.19}$$

where $F_{\mathrm{p,Max}}$ is the peak of the phase curve and $F_{\mathrm{p,Min}}$ is the minimum, excluding the transit and eclipse events. These two points are shown in Figure 1.17. So far there are no obvious trends with hotspot offset or phase curve amplitude with planet temperature (see Figure 1.18), but in Spitzer/IRAC's 4.5 micron channel the phase curve amplitude appears to be correlated with planet temperature. Phase curve observations of more planets with different system parameters are needed to understand which planets are more efficient at redistributing heat from the day- to the night side.

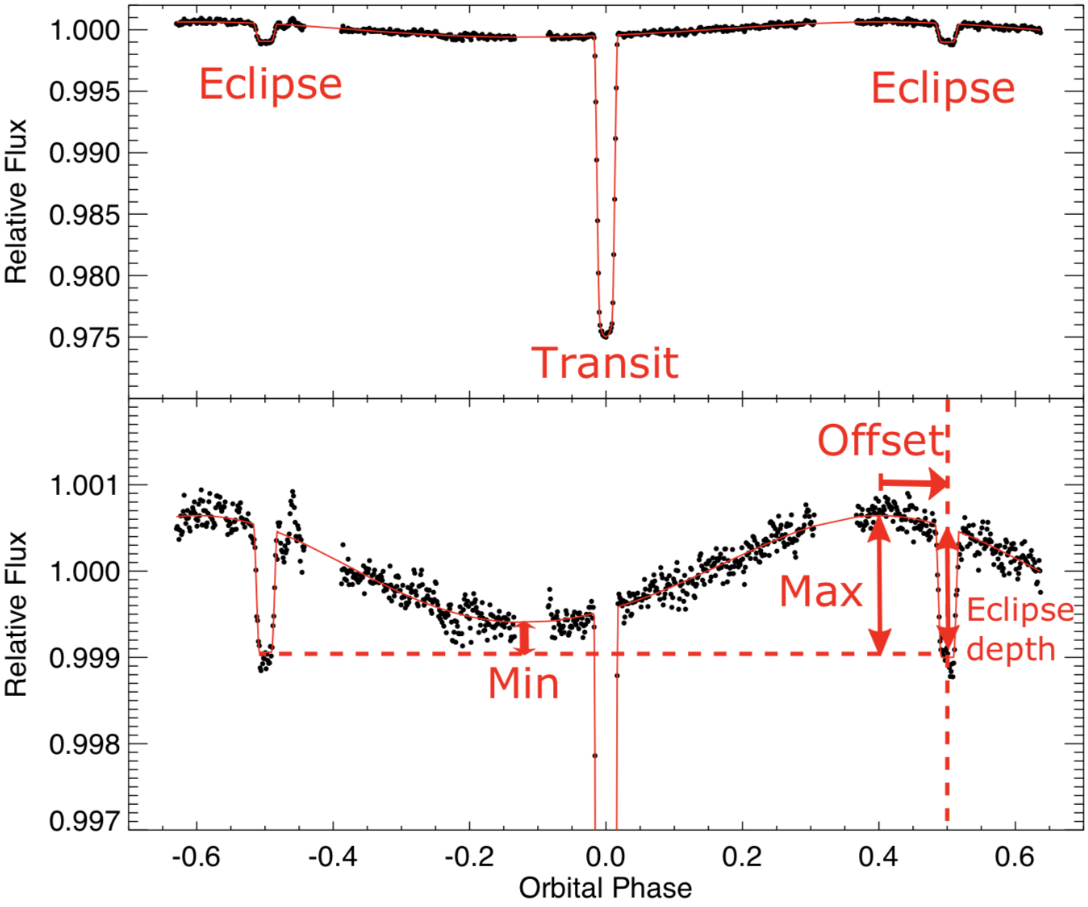

Figure 1.17: Thermal phase curve of the hot Jupiter HD189733b taken with Spitzer's IRAC, in the 3.5 micron channel, from Knutson et al. (2012). Red labels show the relevant measurements that can be made to learn about atmospheric dynamics, similar to the theoretical models in Figure 1.5. Figure from Parmentier & Crossfield (2018)

1.3.3 How has atmospheric escape sculpted the observed population of exoplanets?

There are several physical mechanisms which fall under the umbrella term 'atmospheric escape'. These include thermal processes in the Jeans- and hydrodynamical escape regimes, and non-thermal processes like stellar wind interactions and ejection through impacts. A given planet may be susceptible to many kinds of atmospheric escape, and so understanding exactly why and how a planet loses all or some of its atmosphere can be difficult. In the regime of low mass-loss rates, Jeans escape works as follows: the velocities of individual molecules in a gas change as they collide with one another and gain or lose kinetic energy, and the distribution of kinetic energy among the molecules is described by the Maxwell distrubution. At

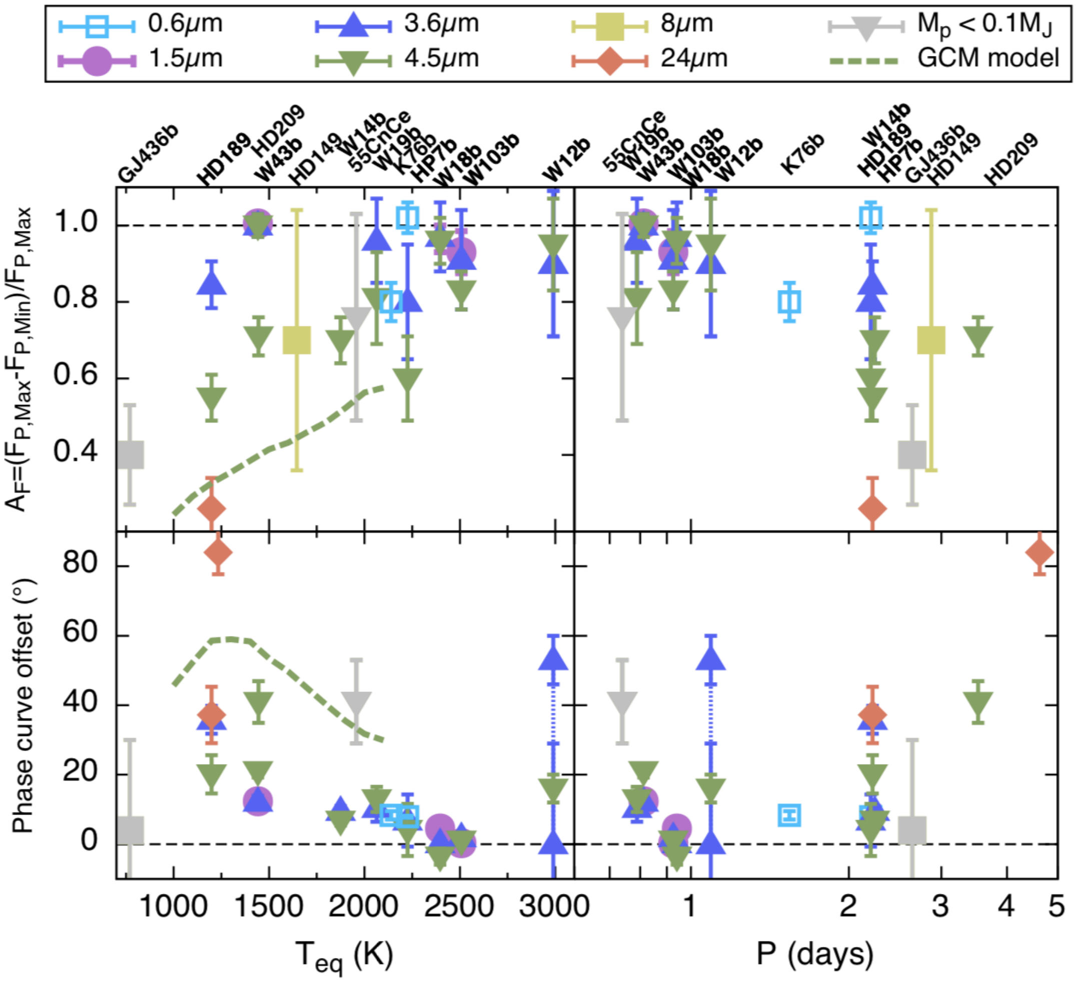

Figure 1.18: Amplitude (top) and offset (bottom) of exoplanet thermal phase curves as a function of equilibrium temperature (left) and orbital period (right). Different symbols and colors represent different wavelengths. Colored points are hot Jupiters, gray points are super-Earths and mini-Neptunes. There is no obvious trend in hotspot offset with equilibrium temperature. Figure from Parmentier & Crossfield (2018)

the top of a planetary atmosphere, individual molecules at the high-velocity tail of the distribution may exceed the escape velocity of the planet, and escape into space (Jeans 1925). Lecavelier des Etangs et al. (2004), modelled Jeans escape for hot Jupiters and showed that the escape rates should be small enough to have negligible effect on the evolution of their atmospheres. This is unsurprising considering the particle-by-particle nature of the mechanism.

On the other hand, hydrodynamical escape can be a much more dramatic process, particularly for highly-irradiated planets. It occurs when a parcel of gas in an atmosphere absorbs high-energy stellar irradiation, heats up, and expands. High-energy EUV and X-ray flux, with wavelengths of 1 240 - 100Å and 100 - 0.1Å respectively, is important for atmospheric escape because the atmospheric gases of planets have large absorption cross-sections at these short wavelengths - so most of the high-energy radiation gets absorbed at the top of the atmosphere. The hot, less-dense gas parcel will follow the negative pressure gradient of the atmosphere and move, in bulk, to higher altitudes, and escape into space. This is the essence of a Parker wind (Parker 1958), a model which was first used to describe the solar wind. This process can give high mass-loss rates as the atmosphere flows into space in bulk, rather than particle-by-particle.

Most exoplanets discovered to date orbit close to their host stars, at separations less than 0.1 AU[4]. At these small distances, planets receive extreme levels of high-energy radiation (e.g. Wheatley et al. 2017, King et al. 2018, 2019), which heat the diffuse upper layers of their atmospheres and can lead to hydrodynamical escape - particularly when the host star is active. It has been suggested that atmospheric escape processes have significantly affected the observed population of small, close-in exoplanets, and sculpted their radii into a tell-tale, double-peaked distribution (e.g. Owen & Wu 2013, Figure 1.19; Fulton et al. 2017, Figure 1.20) - but there is still debate over the significance and physical origin of this effect (Ginzburg et al. 2018; Zeng et al. 2018). It is imperative to understand the physical processes which govern atmospheric escape if we are to understand (1) how exoplanets and their atmospheres evolve over time, (2) how the presently- observed population of exoplanets formed, and ultimately (3) which exoplanets are able to hold on to their atmospheres for billions of years - long enough for life to evolve. Neptune-mass planets or smaller are particularly susceptible to losing significant fractions of their atmospheres over billions of years (Owen & Jackson 2012).

We can place first-order estimates on the mass loss rates of exoplanets by considering the ratio between the high-energy flux received by the star and the energy required to remove a unit mass of atmosphere from the gravitational well of the planet. This ‘energy limited’ approach has been discussed numerous times for Solar System

---

[4] https://exoplanetarchive.ipac.caltech.edu, March 2019

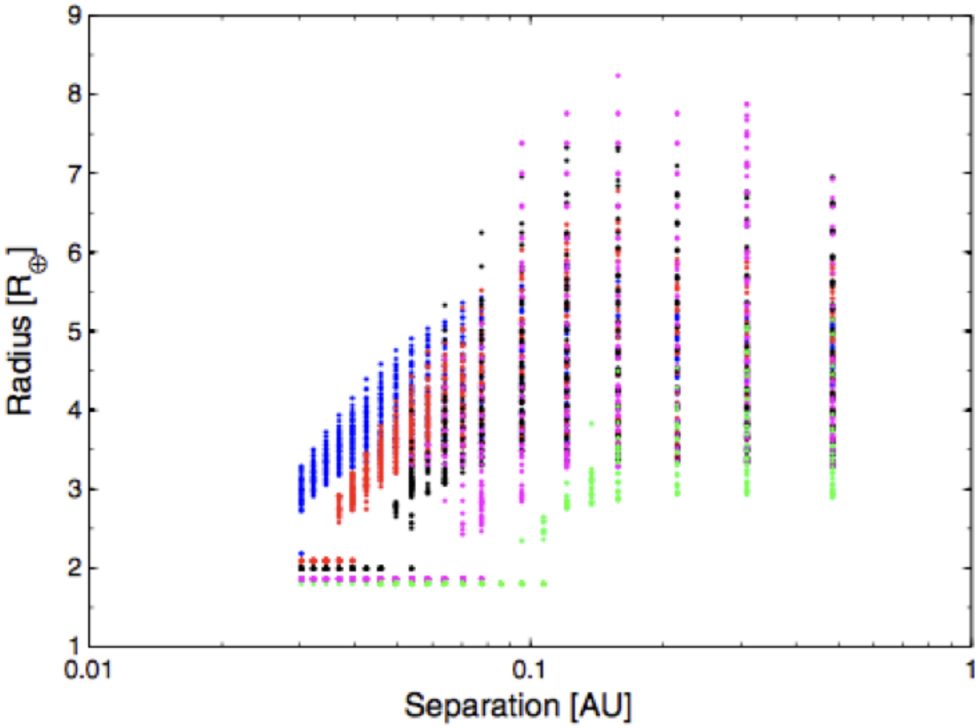

Figure 1.19: Results from exoplanet atmosphere evaporation models from Owen & Wu (2013). Points show the planets left after simulations including atmospheric escape processes. Different colours represent different core masses. The distribution has a clear gap: planets born in the gap have their atmospheres stripped entirely, become bare rocks. Planets above the gap have enough of an envelope that they can maintain their atmospheres for billions of years.

atmospheres (e.g. for Earth and Venus, by Watson et al. 1981) and exoplanet atmospheres (e.g. Lecavelier Des Etangs 2007, Erkaev et al. 2007, Lammer et al. 2009, Davis & Wheatley 2009, Owen & Jackson 2012). The high energy flux recieved by a planet orbiting a star is

$$F_{\rm HE} = \frac{L_{\rm HE}}{4\pi a^2} \times \pi R_{\rm p}^2, \tag{1.20}$$

where $L_{\rm HE}$ is the high-energy luminosity of the star, a is the orbital separation between the star and planet, and $R_{\rm p}$ is the planet radius. The gravitational binding energy of a parcel of atmosphere of mass m is

$$E_{\rm bind} = \frac{GM_{\rm p}}{R_{\rm p}} \times K(R_{\rm Roche}/R_{\rm p}), \tag{1.21}$$

where G is the gravitational constant, $M_{\rm p}$ is the mass of the planet, and $K(R_{\rm Roche}/R_{\rm p})$

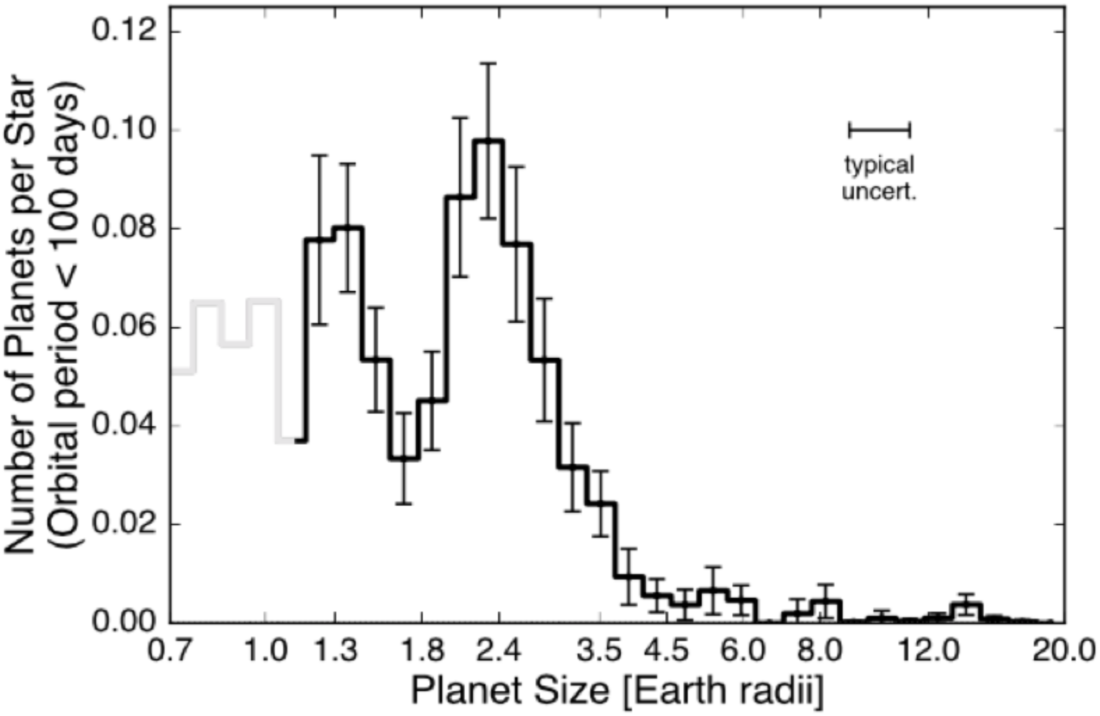

Figure 1.20: Radius-period distribution of 2025 Kepler planets, from Fulton et al. (2017). The gap in the distribution predicted by Owen Wu is clear. This suggests that atmospheric evaporation is indeed important to the evolution of exoplanets.

is a correctional constant that accounts for the reduction in planet binding energy due to the gravitational field of the star. R_{Roche} is the Roche radius of the planet, within which the gravitational influence of the planet dominates. The mass-loss rate of the planet's atmosphere, $\dot{m}$ can be approximated as

$$\dot{m} = \eta \times \frac{L_{\mathrm{HE}} R_{\mathrm{p}}^3}{4 G M_{\mathrm{p}} a^2 K(R_{\mathrm{Roche}}/R_{\mathrm{p}})}, \tag{1.22}$$

where η is the efficiency of the conversion of the stellar flux into useful mass-removing work. One issue with this energy-limited approach is that η is a tunable parameter that we expect to vary with system parameters, so it is difficult to predict mass-loss rates for individual planets with this simple analysis.

Instead, numerical models are required. A wide variety of 1D and multi-dimensional escaping atmosphere models exist in the literature, which each include varying physical processes (e.g. interaction with the stellar wind, stellar radiation pressure on individual particles, consistent hydrodynamics), and predict varying mass-loss rates (e.g. Lammer et al. 2003, Murray-Clay et al. 2009, Koskinen et al. 2010, Bourrier & Lecavelier des Etangs 2013, Tremblin & Chiang 2013, Salz et al. 2016). So far, there have been few direct observations of escaping atmospheres for individual exoplanets, and hence few opportunities to validate model predictions. This is in part due to the difficulty of studying the low-density upper atmospheres of exoplanets, which requires strong absorption lines of gases that represent a significant fraction of the composition of the upper atmospheres.

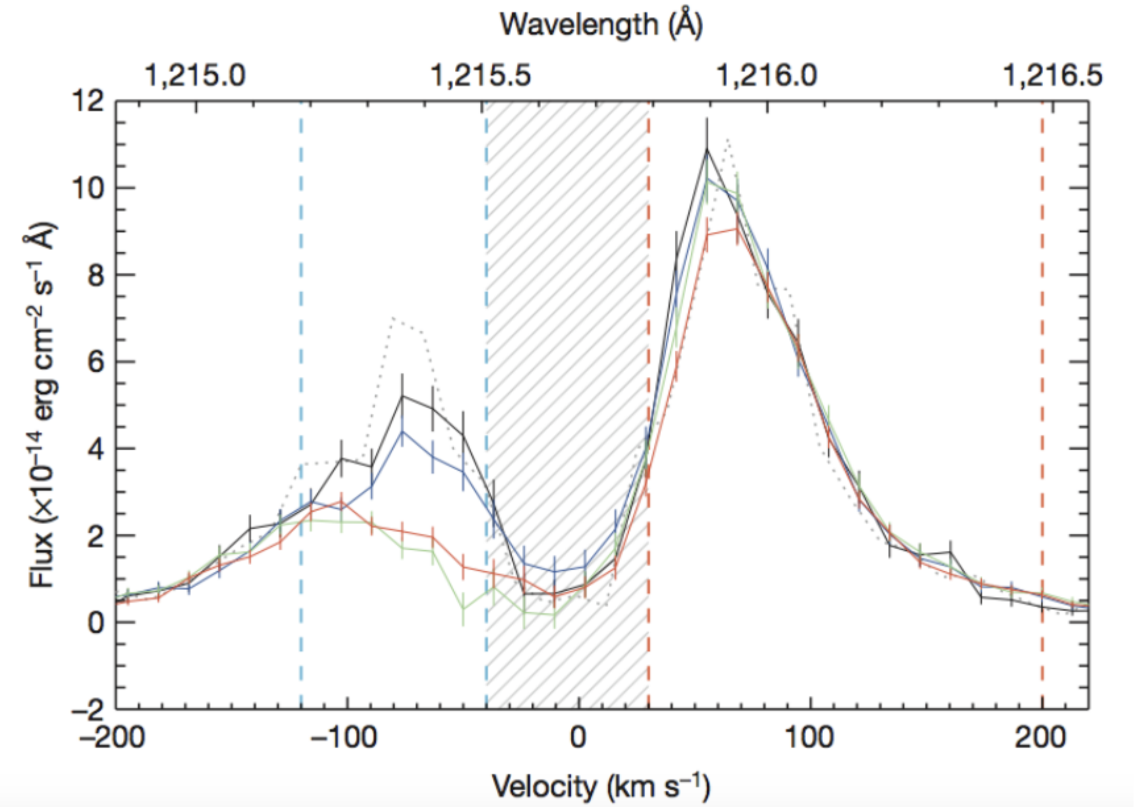

Figure 1.21: Detection of hydrogen absorption around the exoplanet GJ436b, using the Lyman-alpha line from Ehrenreich et al. (2015). The black line is the stellar flux before planetary transit, the green line is flux recieved during mid-transit, other lines are during ingress and egress. The shaded region shows wavelengths affected by absorption from the interstellar medium, which were not used in the analysis. The planet is less than 1% of the size of the star yet during mid transit it blocks out around 50% of the stellar flux.

Very soon after the first transiting exoplanet was discovered, and the first exoplanet atmosphere was discovered (Charbonneau et al. 2002, 2000), a large cloud of neutral hydrogen was observed surrounding the hot Jupiter HD209458b (Vidal-Madjar et al. 2003), via the Lyman-alpha line at UV wavelengths. The large size of the absorption signal suggested that the material was overflowing Roche radius (the sphere of gravitational influence) of the planet. This indicated that the planet was losing its atmosphere. Since then, large absorption signals in the Lyman alpha line have been measured for three more exoplanets (HD189733b: Lecavelier Des Etangs et al. 2010; GJ46b: Kulow et al. 2014; and GJ3470b Bourrier et al. 2018), some of which seem to be overflowing their Roche radius. GJ436b is a particularly striking example, because the planet itself is less than 1% of the size of the host star, but its extended atmosphere blocks out over 50% the starlight in the Lyman-alpha line (see Figure 1.21).

The difficulty of observing with the Lyman-alpha line is that Lyman-alpha radiation is absorbed by neutral hydrogen in the interstellar medium (ISM), leading to lower stellar flux, particularly in the core of the line corresponding to low radial velocity shifts. Additionally, hydrogen in the Earth's geocorona *emits* at Lyman-alpha wavelengths (see Figure 1.22). Therefore, we can only observe Lyman alpha absorption from the very closest exopanet systems, and the core of the line is completely unusable - this can be seen in Figure 1.21.

More evidence of exoplanetary escaping atmospheres have been observed at other wavelengths besides the Lyman-alpha line. For example, UV transit spectroscopy of HD209458b revealed large transit depths in narrow absorption lines of neutral oxygen and singly-ionised carbon (Vidal-Madjar et al. 2004) and similarly for HD189733b (Ben-Jaffel & Ballester 2013). The presence of heavy-elements in the extended atmospheres of hot Jupiters suggests that the atmospheres are escaping hydrodynamically and dragging heavier elements out into space. X-ray photons are absorbed by heavy elements (e.g. Verner & Yakovlev 1995) and an absorption depth of ∼5 - 8% was detected in a broadband X-ray transit for HD189733b (Poppenhaeger et al. 2013), which again supports the case for hydrodynamical escape on the planet. Additionally, Fossati et al. (2010) and Haswell et al. (2012) observed near-UV transits of WASP-12b and found some evidence of magnesium and iron in its upper atmosphere. Finally, Jensen et al. (2012) observed some evidence of extended hydrogen envelopes around the exoplanets HD209458b and HD189733b, and Yan & Henning (2018) detected strong evidence of hydrogen in the upper atmo-

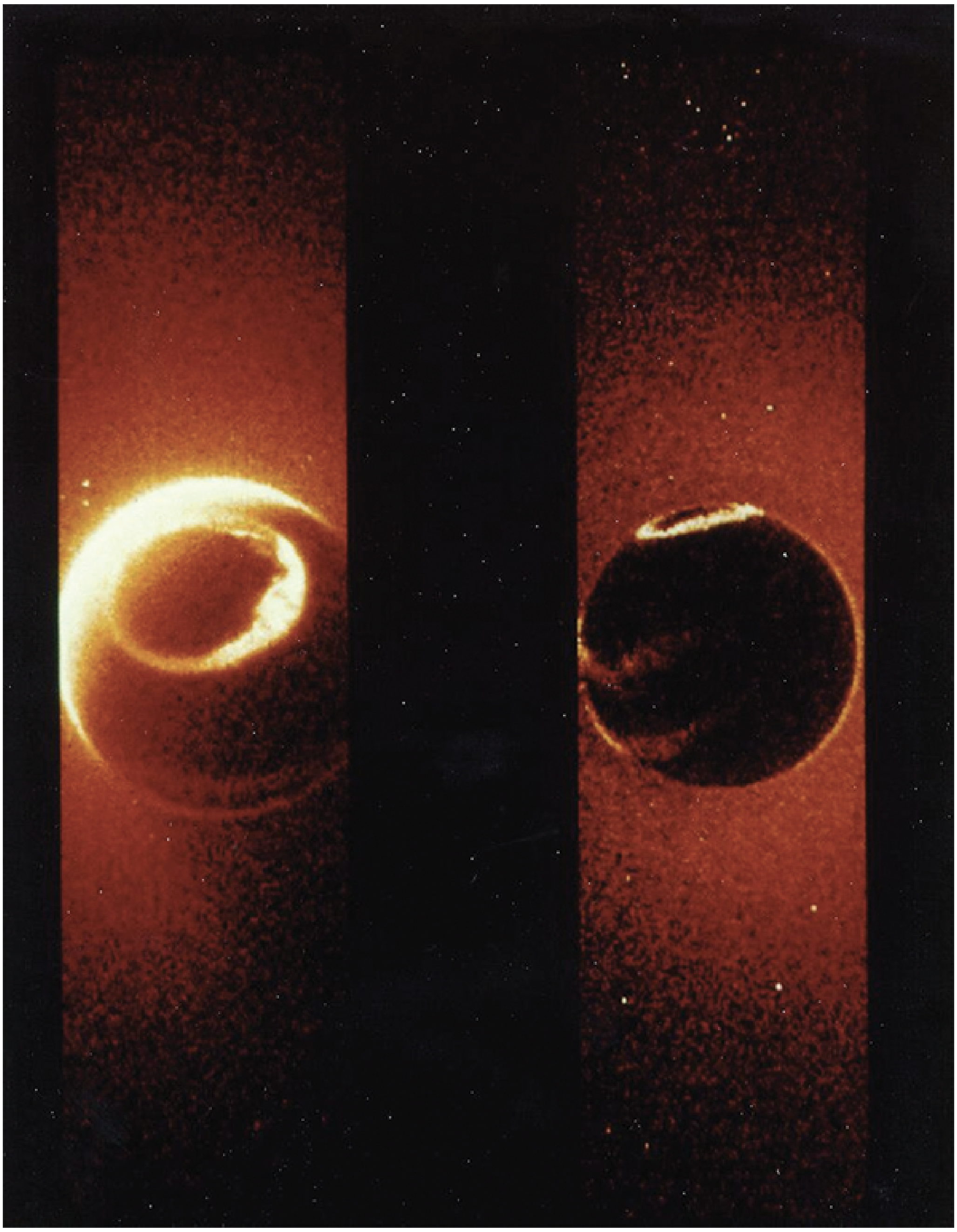

Figure 1.22: Image of the Earth at UV wavelengths taken from the Spin-scan Auroral Imaging instrument on board the Dynamics Explorer 1, at an altitude of 16,500 km. The large cloud surrounding the earth shows Lyman alpha emission from neutral hydrogen. Upper atmospheres of planets can extend to distances on the order of planetary radii. The geocoronal Lyman alpha emission makes astrophysical observations in the core of the line impossible. The glow at the pole and equator shows UV emission from oxygen. Image from NASA.

sphere of KELT-9b from the ground using the Balmer H-alpha line in the optical. In Chapter 2 we present the first observations of an extended (and possibly escaping) exoplanet atmosphere using infrared wavelengths, via the 10 830Å absorption line of metastable helium, which is briefly discussed below. One benefit of looking for helium in the upper atmospheres of exoplanets is that unlike Lyman alpha, 10 830Å radiation is not absorbed by the interstellar medium.

Helium in exoplanet atmospheres

Helium is the second most abundant element in the universe after hydrogen and is a major constituent of gas-giant planets in our Solar System. A neutral helium atom can exist in a singlet or triplet state - that is, its two electrons can either have their spins anti-aligned, or aligned, respectively. The 10 830Å helium triplet line corresponds to the transition between triplet states described by the term symbols 2^3S and 2^3P (see Figure 1.23). The first number of a term symbol is the principal quantum (shell) number, the superscript '3' denotes a triplet state, and the letter describes the azimuthal quantum number, L. The 10 830Å line can become prominent in highly-irradiated atmospheres as follows. Firstly, abundant neutral helium in the upper planetary atmosphere is photo-ionized by extreme ultraviolet (EUV) radiation at wavelengths shorter than 504Å, from the nearby host star. The resulting helium ions recombine with free electrons, which de-excite to lower energy levels. Approximately 75% of the cascading electrons end up in the triplet 2^3S state (Osterbrock & Ferland 2006), which is a metastable state. This is essentially a pseudo-ground state, because the transition from the 2^3S to the singlet ground state (1^1S) is doubly forbidden by quantum-mechanical selection rules. You cannot have two electrons with the same spin in the same state, but spin must be conserved. Additionally, the transition would violate the azimuthal angular momentum selection rule - if there is an electron jump, $\Delta L = \pm 1$, so the electron cannot jump from one S state to another. However, relativistic corrections to the magnetic dipole transition formula allow for the radiative decay of this transition. Its decay lifetime is 7 870±510 seconds (Drake 1971; Hodgman et al. 2009), giving the excited state an extremely long lifetime, compared to typical lifetimes on the order of nanoseconds for other excited atomic states. The long lived 2^3S helium atoms are then excited to the 2^3P state by incident stellar continuum photons at 10 830Å, resulting in a strong absorption feature in the planetary transmission spectrum at this wavelength.

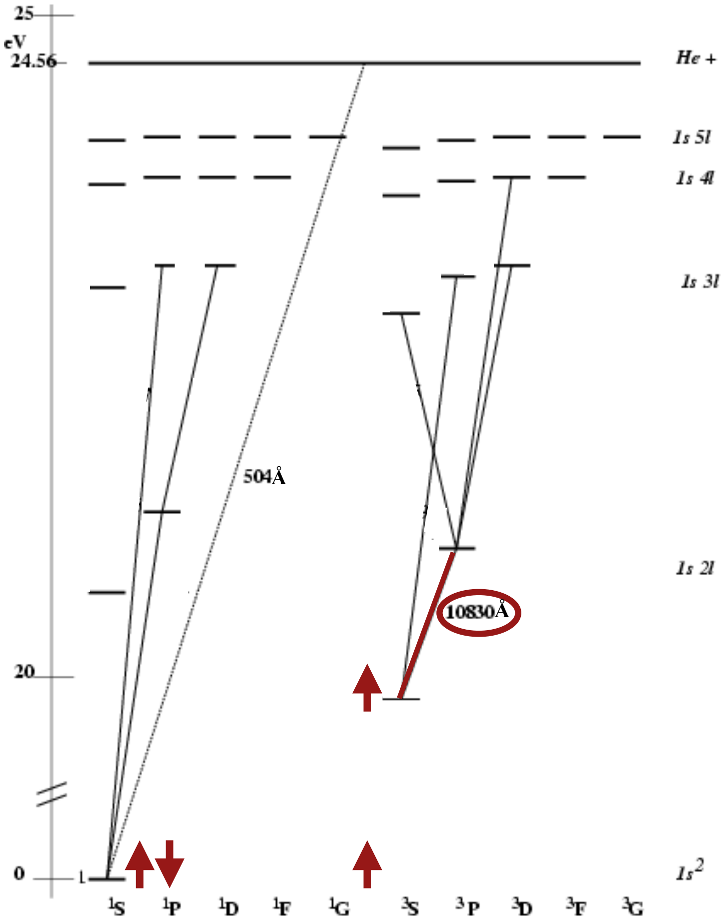

Figure 1.23: Energy levels of a helium atom, including the metastable state. The decay from the metastable state is forbidden by quantum mechanical selection rules, because both of the electrons have the same spin state. Relativistic corrections allow for the forbidden transition, however (Drake 1971).

In one of the earliest theoretical studies of transiting exoplanet atmospheres, Seager & Sasselov (2000) predicted that helium should be readily-detectable in transiting exoplanet atmospheres via the 10 830Å line. However, searches for helium have until now been unsuccessful - for example, Moutou et al. (2003) searched for helium in the atmosphere of the hot Jupiter HD209458b using the ISAAC spectrograph on the VLT, and found an upper limit of 0.5% at 3σ for a 3Å-wide bin. The first detection of helium on an exoplanet is presented in Chapter 2. We note that Turner et al. (2016) included the line in their list of ∼60 potentially interesting absorption lines for probing upper exoplanet atmospheres, and Oklopčić & Hirata (2018) were developing hydrodynamical models of 10 830Å absorption in escaping atmospheres at the time we made the detection.

Chapter 2

The cold: helium in the eroding atmosphere of WASP-107b

2.1 Statement of contribution

Sections of Chapter 2 have been previously published in Spake et al. (2018). J. J. Spake led the HST telescope time proposal (GO-14916), designed the observations, led the data analysis, identified the planetary helium, and wrote the manuscript with contributions from T. M. Evans, V. Bourrier, A. Oklopčić, J. Irwin, B. V. Rackham and G. W. Henry. A. Oklopčić and V. Bourrier performed detailed modelling of WASP-107b's upper atmosphere, with contributions from D. Erenreich. D. K. Sing performed the retrieval analysis.

2.2 Introduction

Here we present the first detection of helium on an exoplanet, at a confidence level of 4.5σ. We measured the near-infrared transmission spectrum of the warm gas giant WASP-107b (Anderson et al. 2017) with the Hubble Space Telescope and identified the narrow absorption feature of excited, metastable helium at 10 833 angstroms. The amplitude of the feature, in transit depth, is $0.049 \pm 0.011\%$ in a bandpass of

98 angstroms, which is more than 5 times greater than that which could be caused by nominal stellar chromospheric activity. The large absorption signal suggests that WASP-107b has an extended atmosphere that is eroding at a total rate of $10^{10} - 3 \times 10^{11}$ g/s (0.1-4% of its total mass per Gyr). WASP-107b is one of the lowest density planets known, with a radius similar to that of Jupiter ($0.94\pm0.02\mathrm{R_J}$) but a much lower mass ($0.12\pm0.01\mathrm{M_J}$). It orbits an active K6 dwarf every 5.7 days at a distance of 0.055±0.001 astronomical units (Anderson et al. 2017). WASP-107b is a particularly favourable target for the detection of helium absorption at 10 830Å, since it is an extremely low-density exoplanet, and thus prone to atmospheric escape. In addition, its active K6 star (Dai & Winn 2017; Močnik et al. 2017) is expected to have high EUV flux (which ionizes ground-state helium electrons) relative to near ultraviolet (NUV) flux which knocks electrons out of the metastable state (at <2 590Å). WASP-107b is a favourable target for characterisation using transmission spectroscopy, because its large atmospheric scale height and small, bright host star mean we can measure wavelength-dependent variations in its transit depth with a high signal-to-noise ratio (SNR). Figure 2.1 shows that we expect to measure WASP-107b's transit depth with an SNR of 20 in a wavelength channel of width 40 nm. With an equilibrium temperature of 700 K, WASP-107b is the coolest exoplanet to have such a high expected SNR for transit depth measurements. Because the majority of transiting exoplanets with detected atmospheres are hotter than 1 000 K (e.g. Sing et al. 2016, Evans et al. 2016), WASP-107b presents a favourable opportunity to probe the atmosphere of a colder exoplanet.

2.3 Observations & data reduction

On 31 May 2017, we observed one transit of WASP-107b with WFC3 on board the Hubble Space Telescope (HST), in spectroscopic mode, using the G102 grism (GO-14916, P.I. Spake). Our observations lasted 7 hours and we acquired 84 time-series spectra with the G102 grism, which covers the 8 000 11 000Å wavelength range. We used forward spatial scanning to spread the spectra over $\sim$ 60 pixels in the

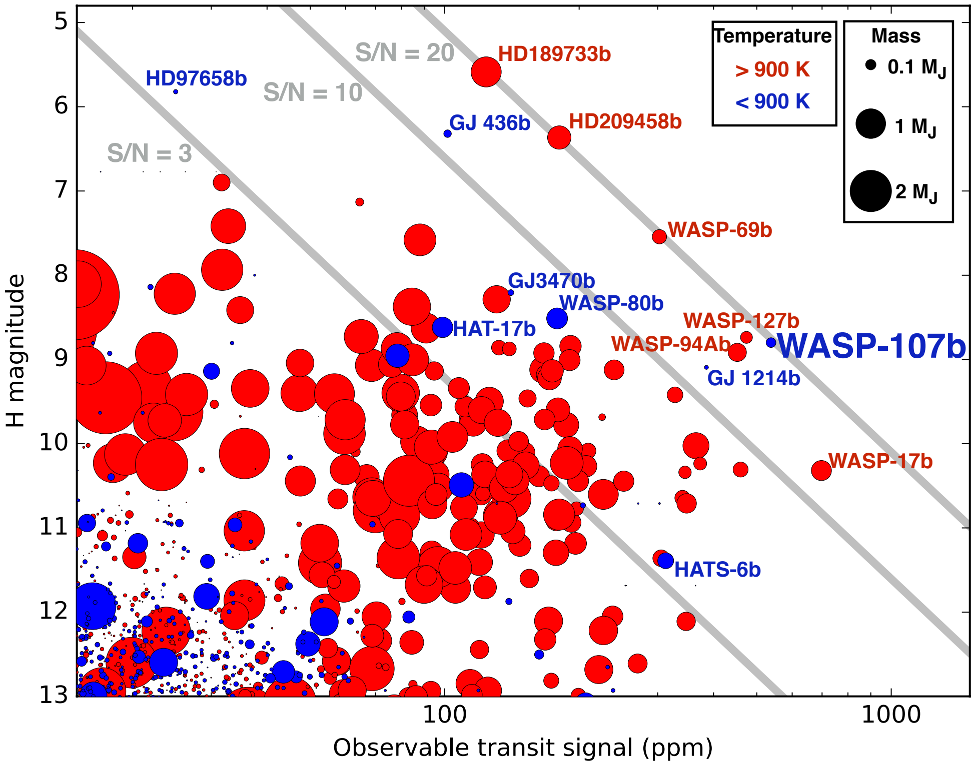

Figure 2.1: Observable atmospheric signals for well-characterized transiting exoplanets. Grey lines are contours of constant signal-to-noise ratio (SNR) of the change in transit depth due to a planetary radius change equivalent to one atmospheric scale height per 40 nm wavelength channel. Based on the precision measured for WASP-12b (Kreidberg et al. 2015). WASP-107b is a favourable planet for transmission spectroscopy, with an expected SNR rivalling the canonical planets HD209458b and HD189733b. It is also the coolest transiting exoplanet to have such a high expected SNR for atmospheric characterisation.

cross-dispersion direction with the SPARS10, NSAMP=15 setup, giving exposure times of ~ 103 seconds. This allowed 17 exposures per HST orbit. The observations lasted for five HST orbits, with two orbits pre-transit, one during the transit, and one post-transit, allowing us to precisely constrain the out-of-transit baseline. The raw frames were first reduced with the automatic CalWF3 pipeline. The 1-D spectra were then extracted following standard methods (Evans et al. 2016): building up flux counts by summing the difference between successive non-destructive reads. We removed the background from each read difference by subtracting the median of a box of pixels uncontaminated by the spectrum. We found the flux-weighted centre of each scan and set to zero all pixels more than 75 rows away from the centre in the cross-dispersion axis, which removes many cosmic rays. The remaining cosmic rays were flagged by finding 4 σ outliers relative to the median along the dispersion direction. We replaced each flagged pixel with the median along the dispersion direction, re-scaled to the count rate of the cross-dispersion column. Since the scans are visibly tilted from the dispersion axis, we used the IRAF package Apall to fit the trace of the 2-D scans and extract 1-D spectra. We found the wavelength solutions by cross-correlating the extracted spectra with an ATLAS model stellar spectrum (Castelli & Kurucz 2004) which most closely matches WASP-107 ($T_{\rm eff} = 4\,500$ K, log $g = 4.5$ cgs) modulated by the G102 grism throughput. Following standard methods (Kreidberg et al. 2018b) we interpolated each spectrum onto the wavelength range of the first to account for shifts in the dispersion axis over time. An example 1D spectrum is shown in Figure 2.2, where it can be seen that the resolution is too low to resolve the 10 830Å helium line.

2.4 Data analysis and results

2.4.1 White light curve analysis

We extracted the white light curve by summing the total counts of each 1-D spectrum. The raw light curve is shown in Figure 2.3. Like all time-series data from

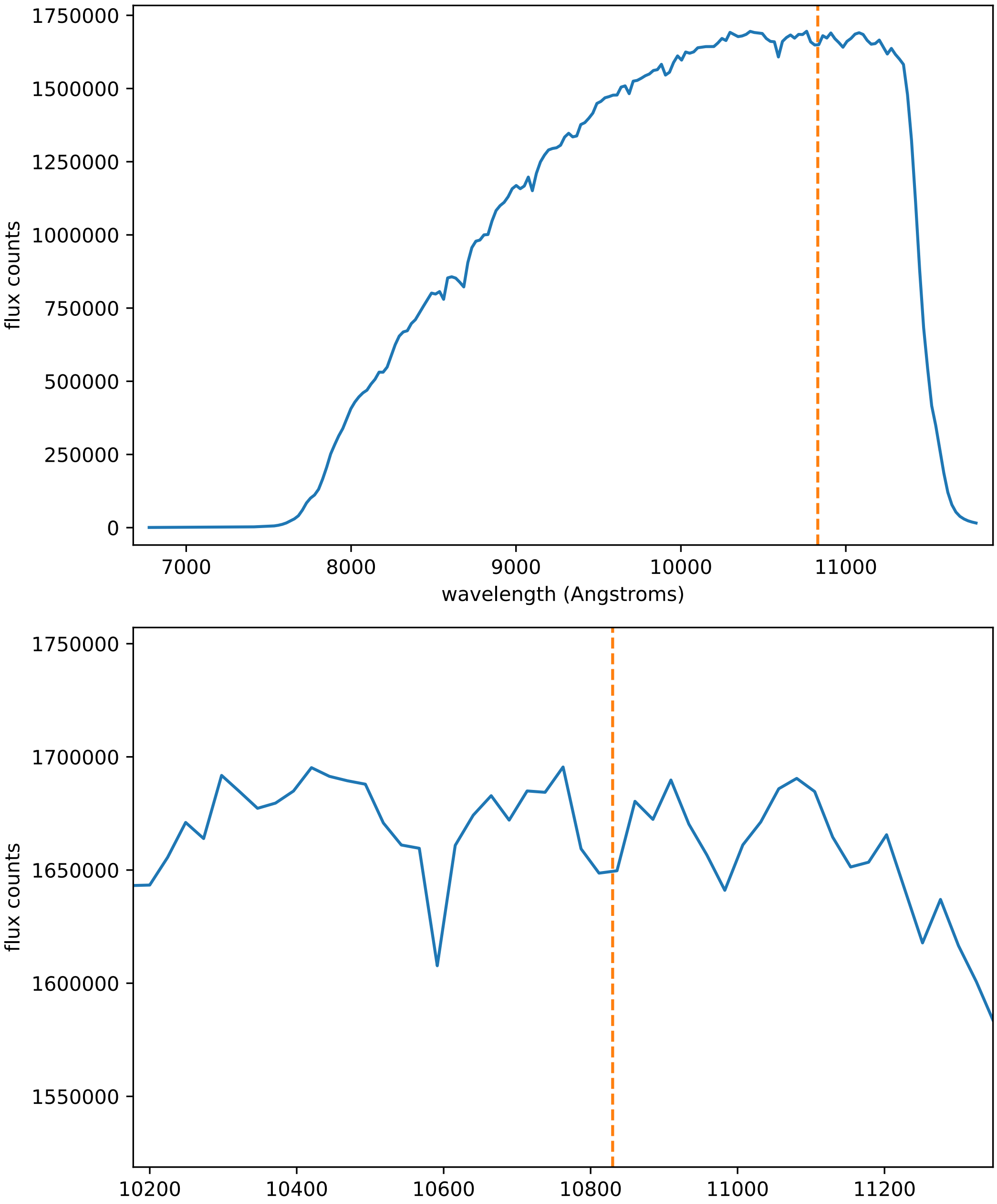

Figure 2.2: Example 1D stellar spectrum of WASP-107 (10th exposure in the time series) measured with HST/WFC3+G141. Top panel shows the full spectrum, bottom panel shows a zoom-in of around the 10 830Å helium line (orange dashed line), which has an approximate width of 3Å. The spectrum has a resolution of around $\Delta\lambda \sim 67$Å (Kuntschner et al., 2009), so the helium line is not resolved in the individual stellar spectra.

HST/WFC3's infrared channel, the photometry is affected by strong, ramp-like systematics in each of the 5 orbits - particularly the first - which is common in many similar infrared detectors. The individual elements of the WFC3 IR detector are photodiodes, which absorb photons and produce "free" charge carriers (electrons and holes). The free charge carriers follow the electric potential of the diode to reach the depletion zone. From there, the charge carriers are collected and measured as the signal. However, imperfections in the material can trap free charge carriers as they diffuse across the depletion zone, and lead to a lower measured signal. The PN junction is reset at the end of each exposure, but the trapped charge carriers can remain in the depletion region. The trapped charges are gradually released in subsequent exposures, which generates a signal, and causes an increasing "ramp" shape in time-series photometry. In order to model this systematic effect in the WASP-107b light curves, we used the RECTE model (Zhou et al. 2017), which is based on the charge-trapping theory of Smith (2008). RECTE models two populations of charge traps in individual pixels of the detector: a slow trap population that releases trapped particles with a long trapping lifetime, and a fast trap population that releases trapped particles with a short trapping lifetime. Zhou et al. (2017) previously analysed hundreds of orbits of WFC3 photometry to characterise the release-times of the two trap populations, and their model successfully replicates the ramp-like features that dominate WFC3 systematics.

In order to constrain the mid-time of the transit, we fit the white light curve with the BATMAN transit model (Kreidberg 2015), multiplied by a linear baseline trend and the RECTE systematics model. The free parameters of our final model were: the planet-to-star radius ratio, $\mathrm{R_p/R_s}$; mid-transit time, $\mathrm{t_0}$; the gradient and y-intercept of the linear background trend, $\mathrm{c_1}$ and $\mathrm{c_0}$ respectively; four parameters for the charge trapping model - the initial number of populated slow and fast traps s_{pop} and f_{pop}, and the changes in the two populations between each orbit, δs and δf; and an uncertainty rescaling factor, β for the expected photon noise. We fixed $\mathrm{a/R_s}$, i, e, and the period using estimates from Kepler light curves (Dai & Winn 2017).

To model the stellar limb darkening we fitted a four-parameter non-linear limb

Parameter	Value
$\mathrm{R_p/R_s}$	0.142988 ± 0.00012
t_0 ($\mathrm{BJD_{UTC}}$	2 457 904.7295 ± 0.0002
c_0	1.00004±0.00002
c_1	-0.0018±0.0002
s_{pop}	62±17
f_{pop}	42±6
δs	-2±10
δf	65±4
β	1.73±0.15
P	5.72147^a
i°	89.7^a
a/R_{s}	18.164^a
e (assumed)	0

Table 2.1: Fitted parameters from the G102 white light curve. Errors quoted encompass 68% of the MCMC samples after burn-in. (a) Parameters fixed from Dai Winn (2017).

darkening law (Claret 2000) to the ATLAS stellar model described above. Because the shape of the ramp-like systematics depends on the count level of the illuminated pixels, the RECTE model requires the ‘intrinsic’ count rate of a pixel (i.e. the actual flux received from the star) in order to model the charge trapping. To create a template of the intrinsic count rate, we median-combined four raw images from the end of the second orbit. Here the charge traps appear completely filled, and the ramp shape has tapered to a flat line. It is possible to model each illuminated pixel, however, for a large scan this is computationally expensive. Additionally, the ramp profile is washed out by systematics that are introduced by telescope jittering and pointing drift. Instead we divided the scan into columns of width 10 pixels along the dispersion axis and fed the median count profiles into the model. We used the Markov chain Monte Carlo (MCMC) package emcee (Foreman-Mackey et al. 2013) to marginalise over the parameter space of the model likelihood distribution. We used 80 walkers and ran chains for 8 000 steps, discarding the first 800 as burn-in before combining the walker chains into a single chain. The best-fit model and residuals are shown in Figure 2.5, with the parameter values and 1 σ uncertainties reported in Table 2.1. Although WASP-107b orbits an active star we see no evidence of star spot crossings. For context, only five spot-crossing events are reported in 10 Kepler transits (Dai & Winn 2017; Močnik et al. 2017).

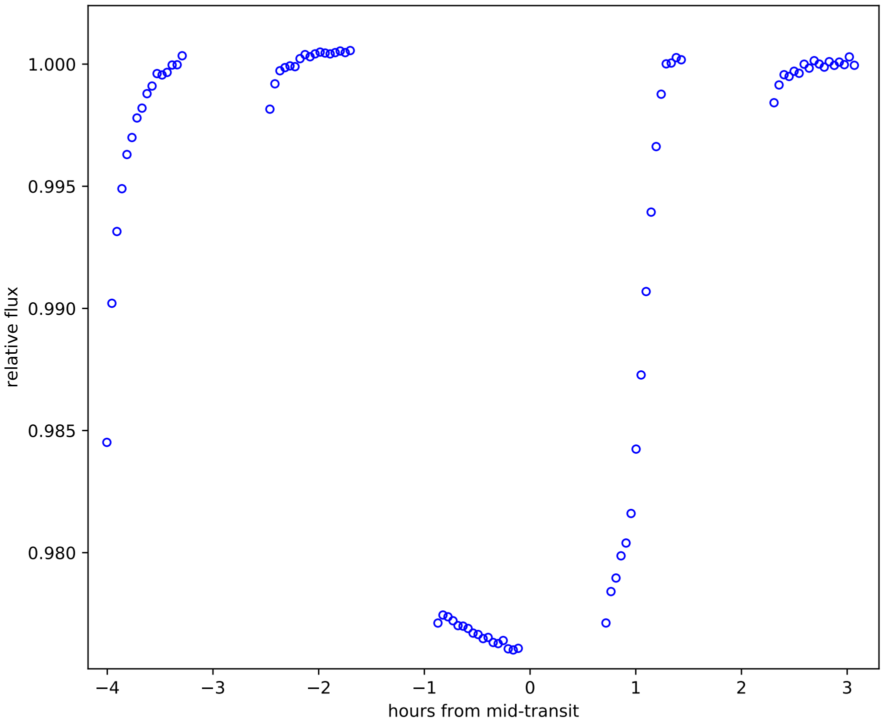

Figure 2.3: Raw G102 white light curve divided by the median out-of-transit flux level. Strong ramp-like shapes can be seen in each of the 5 HST orbits, especially the first.

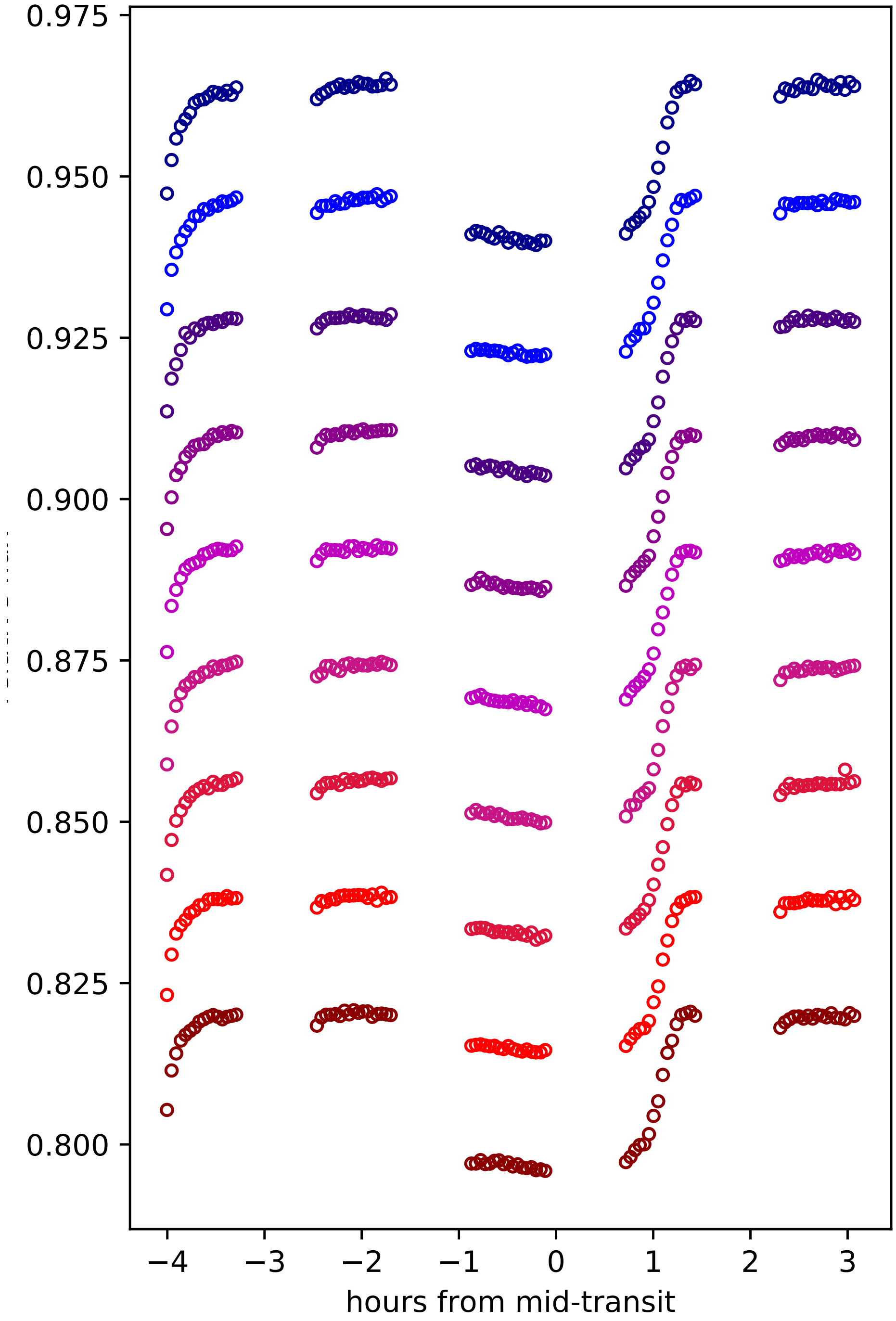

Figure 2.4: Raw G102 spectroscopic light curves divided by their median out-of-transit flux levels. Strong ramp-like shapes can be seen in each of the 5 HST orbits (especially the first), although the ramp shape is slightly different in each spectroscopic channel.

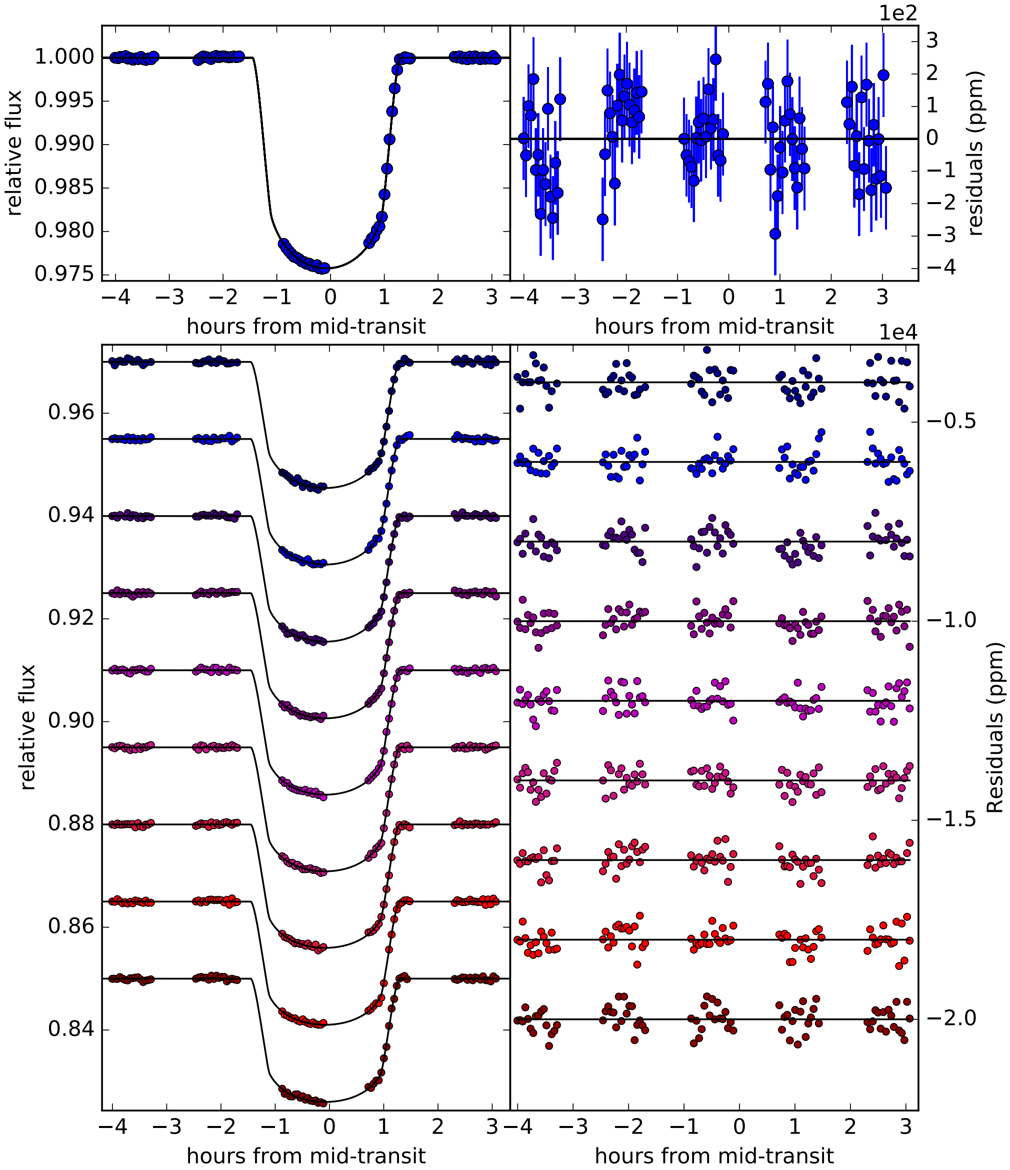

Figure 2.5: G102 white light curve and broadband spectroscopic light curves covering the 0.88-1.14 micron wavelength range for WASP-107b. (a) White light curve relative flux divided by systematics model, with best-fit transit light curve plotted in black. (b) White light residuals and 1σ errors, after removing the combined transit and systematics components of the best-fit model. (c) Points are spectroscopic light curves divided by systematics models, black curves are best-fit transit models, with vertical offsets applied for clarity. (d) Best-fit spectroscopic model residuals with vertical offsets applied for clarity.

2.4.2 Broadband spectroscopic light curve fit

We binned each spectrum into nine spectroscopic channels across the 8 780 - 11 370Å wavelength range, each spanning 10-12 pixels on the detector. The raw light curves can be seen in Figure 2.4. Since the throughput of the G102 grism is wavelength-dependent, the shape of the charge-trapping ramp in each spectroscopic light curve is different. Therefore, for each channel we simultaneously fit for a transit model multiplied by a linear baseline trend and a charge-trap model. To make a template of the intrinsic counts, we took the median cross-dispersion-direction profile of each channel in the same four raw images as used in the white light curve fit. We fixed t_0 to the value found from the white light curve fit. Similarly to the white light curve fit, we fixed the orbital parameters to those derived from Kepler light curves (Dai & Winn 2017), and wavelength-dependent limb darkening coefficients from the ATLAS model. Therefore, for each channel the fitted parameters were $\mathrm{R_P/R_s}$, $\mathrm{c_1}$, $\mathrm{c_0}$, s_{pop}, f_{pop}, δs, δf, and β. We ran MCMC fits for each light curve with emcee, with 80 walkers, 80 000 steps and a burn-in of 800. As a test, we also ran additional fits for the spectroscopic light curves with the stellar limb darkening coefficients as free parameters. The resulting spectrum was consistent with our previous analysis within 1σ. We show the resulting spectroscopic light curves divided by their best-fit systematics models in Figure 2.5, along with their residuals. Table 2.2 reports our median values for the transit depth, $(\mathrm{R_p/R_s})^2$, with 1σ uncertainties calculated from the MCMC chains. We also list the root mean square (RMS) of the residuals for each channel, which range between 1.038-1.198 times the photon noise.

2.4.3 Narrowband spectroscopic light curve fit around 10 830 angstroms

To target the 10 833Å helium triplet, we binned the spectra from 10 590 to 11 150Å into twenty narrowband channels. Each channel spanned 4 pixels on the detector, which is a compromise between the low instrument resolution, signal-to-noise, and the narrowness of the targeted feature. The wavelength coverage of each channel

Wavelength (μm)	Transit depth (%)	Error (%)	RMS residuals (PPM)	RMS /photon noise	Correction factor
8 769 - 9 063	2.0451	0.0084	326	1.178	1.007101
9 063 - 9 356	2.0425	0.0069	276	1.077	1.006785
9 356 - 9 650	2.0514	0.0079	285	1.184	1.006549
9 650 - 9 943	2.0514	0.0064	252	1.083	1.006454
9 943 - 10 237	2.0456	0.0066	264	1.167	1.00634
10 237 - 10 530	2.0448	0.0058	241	1.08	1.006303
10 530 - 10 775	2.0431	0.0065	245	1.048	1.006162
10 873 - 11 142	2.0461	0.007	269	1.152	1.006123
11 142 - 11 386	2.0509	0.0069	298	1.198	1.005945

Table 2.2: Results from broadband transit light curve fits. RMS is the root mean squared of the model residuals in parts per million (PPM); the second-to-last column is the RMS divided by the expected photon noise; the last column is the correction factor we applied to account for stellar variability.

was shifted relative to the adjacent channel by one pixel, so the channels overlap. We note that since the formal resolution of the G102 grism is $\lambda/\Delta\lambda \sim 155$ at 10 400Å[1] (which corresponds to $\Delta\lambda \sim 67$Å, or 2.7 pixel widths), the smallest bins theoretically possible are 3 pixels wide. A resolution of 3 pixels could be achieved if the 10 833Å feature lay in the centre of a pixel, but in our data it lies significantly blue-ward of the centre of its pixel. This means there is some 10 833Å flux in the pixel located two pixels blueward of the 10 833Å line. Indeed, when we tested the 3-pixel case we found that the amplitude of the 10 833Å feature increased by 0.011% from the 4-pixel-bin fit, which is similar to the expected increase of 0.016% if all the 10 833Å flux fell within a central 3-pixel bin. With 3-pixel bins the feature also appeared to have a slight blue wing, which is unlikely to be astrophysical, as such wings would be expected from binning the data to a resolution higher than that of the spectrograph. We therefore used conservative 4-pixel bins. Figure 2.6 shows the spectroscopic light curves divided by their best-fit systematics models, along with their residuals. Table 2.3 shows our median values for the transit depth and their 1σ uncertainties, calculated from the MCMC chains. We also list the RMS of the residuals of each channel, which range from 0.976 to 1.22 relative to photon noise. The resulting transmission spectrum is shown in 2.7. Previous studies (Czesla et al. 2015) have highlighted the importance of considering the effect of

---

[1] WFC3 SMOV proposal 11552: Calibration of the G102 grism, ST-ECF Instrument Science Report WFC3-2009-18, H. Kuntschner, et al. (2009)

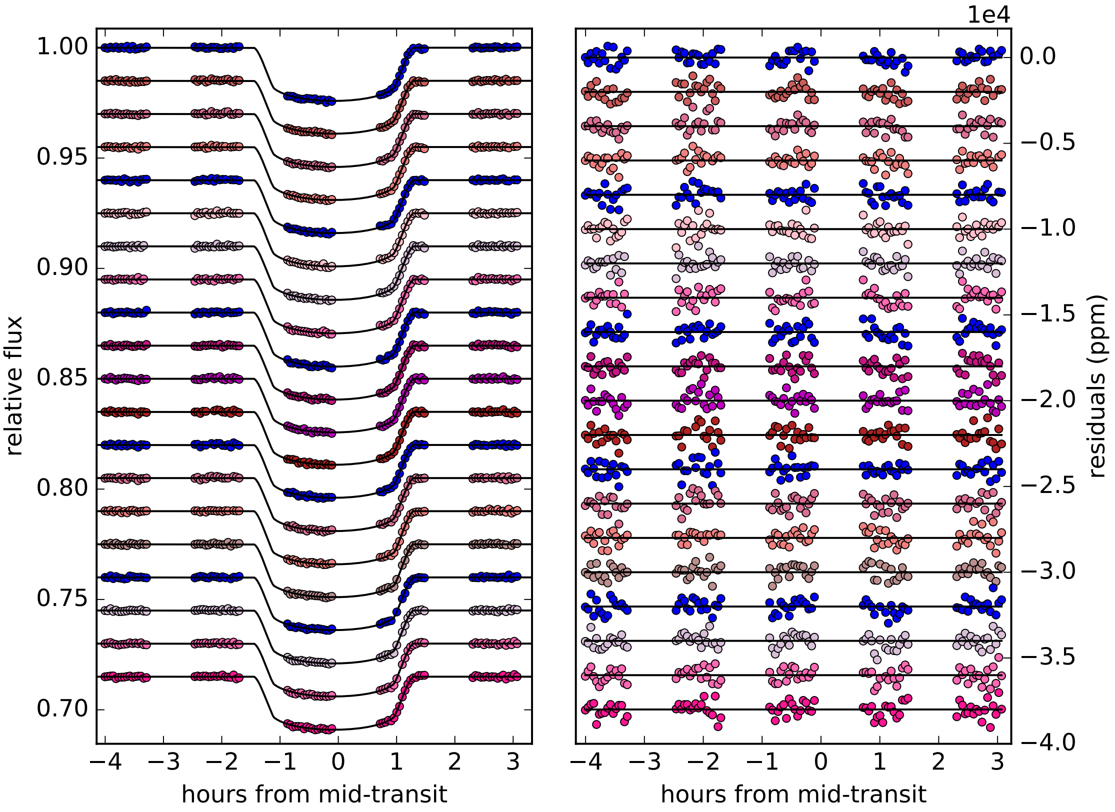

Figure 2.6: Narrow-band (4-pixel-wide) spectroscopic light curves covering the 1.06-1.12 micron wavelength range. (a) Points are light curves divided by systematics models, black curves are best-fit transit models. (b) Best-fit model residuals with vertical offsets applied for clarity. The 5 non-overlapping channels used to measure 10 833Å absorption are highlighted in blue.

stellar limb darkening in stellar absorption lines on exoplanet transmission spectra. To investigate whether this could cause the strong feature at 10 833Å, we re-ran the narrow-band spectroscopic light curve fits whilst fitting for a quadratic limb-darkening law. This produced a transmission spectrum slightly larger uncertainties that was consistent with the fixed limb darkening analysis to within 1 σ (although the final detection of helium was less significant, at a confidence level of 3.2 σ). Strong stellar lines that shift over the edges of pixels can introduce noise to measured transmission spectra (Deming et al. 2013). We checked this effect by smoothing our extracted time series spectra with a Gaussian kernel of FWHM of 4 pixels, and re-running the narrowband spectroscopic light curve fits. Our measured 10 833Å absorption feature remained consistent within 1σ.

Wavelength (μm)	Transit depth (%)	Error (%)	RMS residuals (PPM)	RMS /photon noise	Correction factor
10579 - 10677	2.0634	0.0091	344	0.989	1.00596
10604 - 10701	2.05	0.0088	381	1.102	1.005923
10628 - 10726	2.0604	0.0089	366	1.061	1.006214
10652 - 10750	2.0571	0.0075	336	0.976	1.006167
10677 - 10775	2.0563	0.0082	360	1.043	1.006131
10701 - 10799	2.0643	0.0103	395	1.143	1.006046
10726 - 10824	2.083	0.0094	354	1.023	1.005985
10750 - 10848	2.0964	0.0102	415	1.198	1.005928
10775 - 10873	2.1048	0.0097	391	1.126	1.005923
10799 - 10897	2.0998	0.0084	387	1.117	1.005948
10824 - 10922	2.087	0.0091	390	1.128	1.005949
10848 - 10946	2.0585	0.0095	409	1.183	1.006008
10873 - 10970	2.0546	0.0104	385	1.111	1.005982
10897 - 10995	2.0634	0.0108	423	1.22	1.005973
10922 - 11019	2.0642	0.0098	377	1.087	1.005967
10946 - 11044	2.0543	0.0093	363	1.046	1.005935
10970 - 11068	2.0502	0.0101	375	1.084	1.005962
10995 - 11093	2.0584	0.0103	373	1.082	1.005918
11019 - 11117	2.0564	0.0098	385	1.117	1.005897
11044 - 11142	2.0631	0.0105	414	1.197	1.005891

Table 2.3: Results from narrow-band transit light curve fits. RMS is the root mean squared of the model residuals in parts per million (PPM); the second-to-last column is the RMS divided by the expected photon noise; the last column is the correction factor we applied to account for stellar variability.

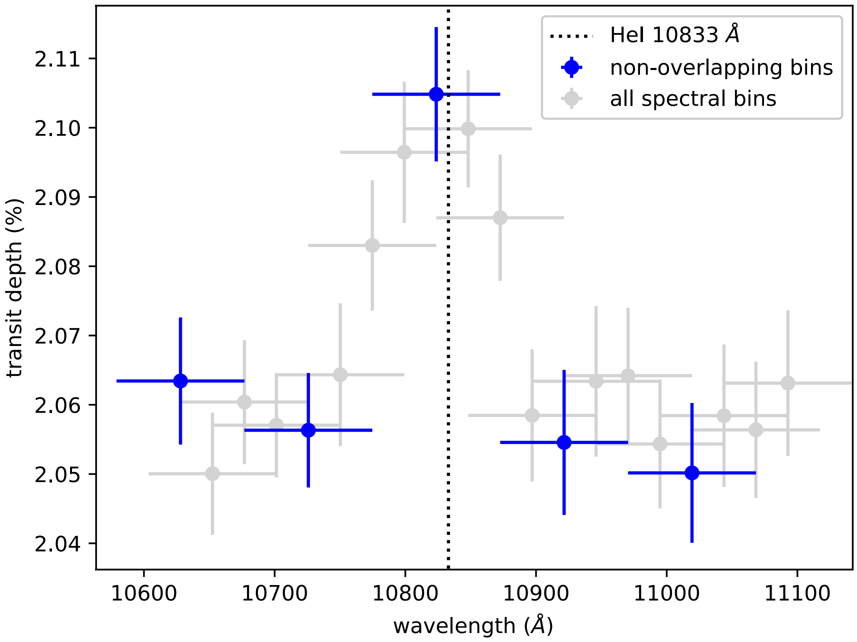

Figure 2.7: Narrow-band transmission spectrum of WASP-107b, centred on 10 833Å. Each spectroscopic channel has been shifted along one pixel from the last. Non-overlapping bins are highlighted in blue. Error bars are 1σ. The peak of the spectrum coincides with the 2^3S helium absorption line at 10 833Å.

2.5 Ground-based photometry and activity correction

2.5.1 MEarth observations

Photometric monitoring observations were gathered using a single telescope (CS 2015) of the MEarth-South array (Nutzman & Charbonneau 2008; Irwin et al. 2015) at Cerro Tololo Inter-American Observatory (CTIO), Chile. Data were obtained on 78 nights from 2017 March 22 (UT) to 2017 August 1 in groups of 4 - 15s exposures, with these exposure groups repeated at a cadence of approximately 30 minutes. A total of 3 096 exposures were gathered over this period. The bandpass of these observations is in the red optical with the blue cutoff defined by RG715 glass at approximately 7 150Å and the red cutoff defined by the decline of the CCD quantum efficiency at approximately 10 000Å. For our data reduction, we applied a standard 2D instrumental signature removal pipeline: cross-talk correction, bias correction, flat fielding and de-fringing. The pipeline is described in detail in (Irwin et al. 2006) and (Irwin et al. 2015). The CCD camera shutter failed on 2017 May 9, which required removal for servicing. This procedure introduces flat-fielding errors not corrected to sufficient precision by standard calibrations, so instead we allow for this explicitly in the analysis by solving for a change in the magnitude zero-points on both sides of the meridian at this date, following standard methods (Irwin et al. 2011). The result of this analysis is a "least-squares periodogram" (shown in Figure 2.8), obtained by simultaneously fitting a periodic modulation, while accounting for the four magnitude zero-points and two additional linear terms describing sources of systematic errors in the photometry (FWHM of the stellar images and the "common mode" as a proxy for the effect of variable precipitable water vapor on the photometry). This procedure would be mathematically equivalent to a Lomb-Scargle periodogram in the absence of these six extra terms. The highest peak in the periodogram and its full width at half-maximum corresponds to a periodicity of 19.7±0.9 days. This is consistent with estimates from Kelper light curves of 17.5±1.4 days (Močnik et al. 2017). We find an amplitude of ∼0.00150 in magnitude.

2.5.2 AIT photometry

We acquired nightly photometric observations of WASP-107 with the Tennessee State University Celestron 14-inch (C14) automated imaging telescope (AIT) located at Fairborn Observatory in southern Arizona (Henry 1999). The observations were made in the Cousins R passband with an SBIG STL-1001E CCD camera. Differential magnitudes of WASP-107 were computed with respect to eight of the most constant comparison stars in the CCD field. Details of our data acquisition, reduction, and analysis can be found in Sing et al. (2015), which describes a similar analysis of the planetary-host star WASP-31. A total of 120 nightly observations (excluding a few observations in transit) were collected between 2017 Feb. 23 and June 28. The nightly differential magnitudes are plotted in panel (a) of Figure 2.9. Panels (b) and (c) show the frequency spectrum of the observations and the phase curve computed with the best frequency. Our frequency analysis is based on least-squares sine fits with trial frequencies between 0.01 and 0.5 per day, corresponding to periods between 2 and 100 days. The goodness of fit at each frequency is measured as the reduction factor in the variance of the original data. Low-amplitude brightness variability is seen at a period of 8.675±0.043 days with a peak-to-peak amplitude of only 0.005 mag. Our period is almost exactly half the 17.5-day rotation period found in Kepler light curves (Močnik et al. 2017) and demonstrates that WASP-107 has spots or spot groups on opposite hemispheres of the star during the epoch of our observations. The WASP-107b discovery team (Anderson et al. 2017) also found periods of around 17 and 8.3 days in their 2009 and 2010 photometry.

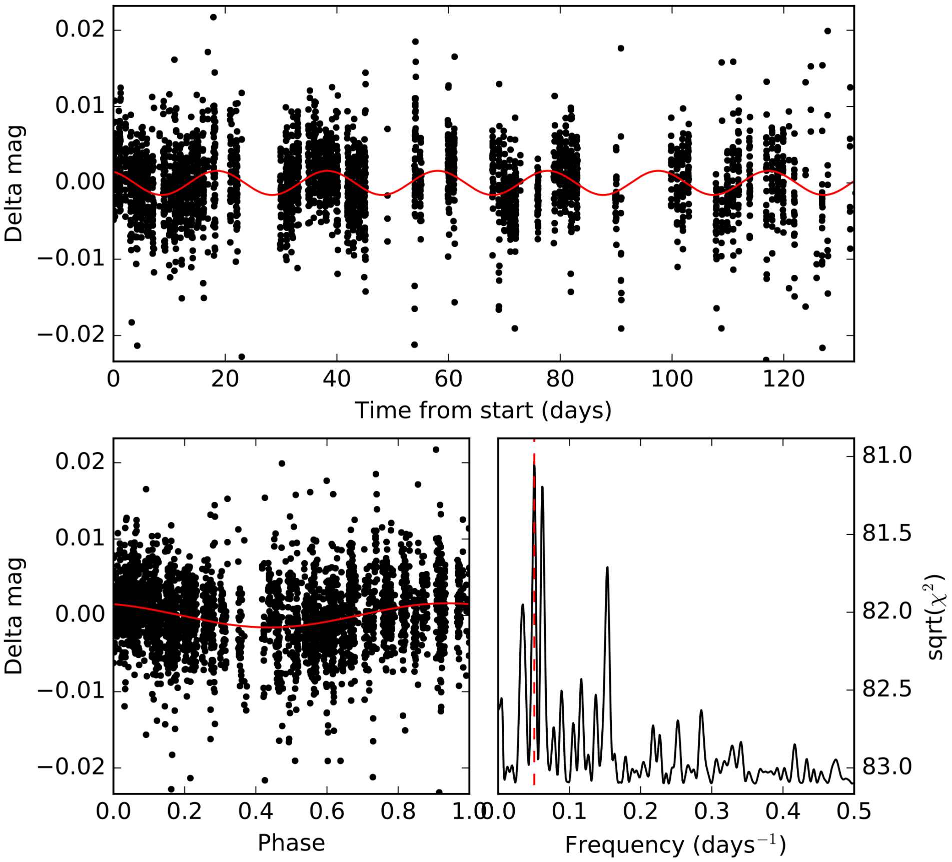

Figure 2.8: Ground-based photometry for WASP-107 from MEarth. We performed a Lomb-Scargle periodogram search and found a best-fit period of 19.7±0.9 days, with a relative amplitude of ∼0.00150 mag.

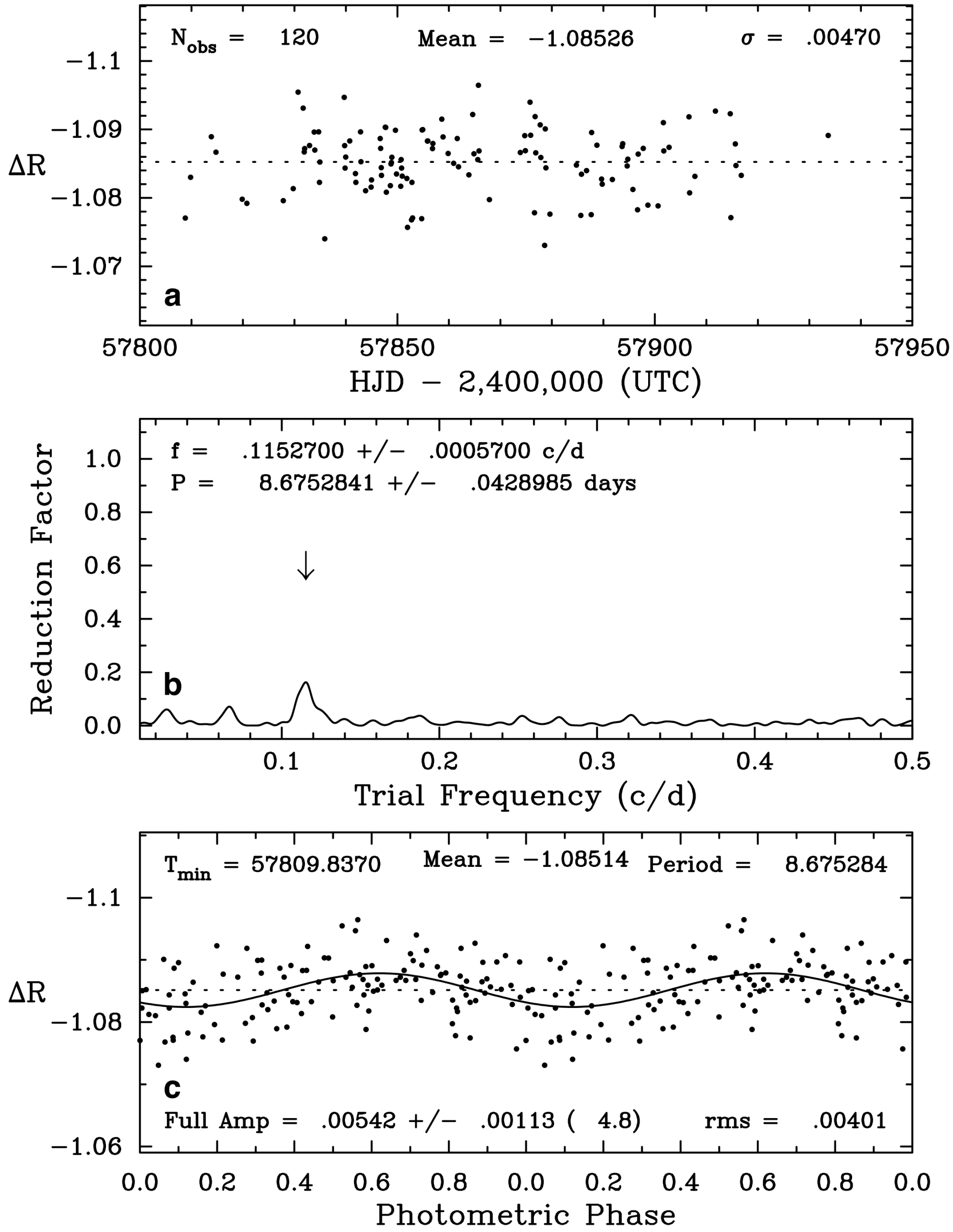

Figure 2.9: Ground-based photometry for WASP-107b from AIT. (a) The nightly photometric observations of WASP-107 in the Cousins R band acquired with the Tennessee State University C14 automated imaging telescope at Fairborn Observatory during the 2017 observing season. (b) The frequency spectrum of the 2017 observations shows low-amplitude variability with a period of 8.675 days. (c) The data phased to the 8.675-day period, has a peak-to-peak amplitude of just 0.005 mag.

2.5.3 Stellar variability correction

To correct for stellar variability between the G141 and G102 epochs, we followed a similar method to previous studies (Aigrain et al. 2012; Huitson et al. 2013), and estimated the flux from the non-spotted stellar surface as $F_{\mathrm{s}} = max(F) + k\sigma$, where F is the photometric light curve, k is a fitted value and σ is the scatter of the light curve. Aigrain et al. (2012) found that $k = 1$ is a good value to use for active stars, so we adopted this value. We used the best-fit period, amplitude and ephemeris from the MEarth photometry to estimate the expected flux dimming correction at the mid-transit times for both data sets. We used the wavelength-dependent spot correction factor developed by Sing et al. (2011) to correct for unocculted spots, and we set the spot temperature to be 3 200K. After the correction, the two spectra align well and appear to share a flat baseline. The one overlapping spectral channel between G102/G141 is consistent within 1σ.

2.6 ATMO Retrieval

For the combined G102 and G141 broadband spectrum corrected for photoshperic variability, we performed an atmospheric retrieval analysis using our one-dimensional radiative transfer code, ATMO (Amundsen et al. 2014; Tremblin et al. 2015, 2016; Wakeford et al. 2017; Evans et al. 2017). We assumed an isothermal temperature-pressure profile, and used MCMC to fit for the following parameters: atmospheric temperature; planetary radius at a pressure of 1 mbar; grey cloud opacity; and the abundances of H_2O, CO_2, CO, CH_4, NH_3, H_2S, HCN and C_2H_2. We assumed solar abundances under chemical equilibrium for other gas species. Note that for this analysis we excluded wavelengths coinciding with the narrowband channel centred on the 10 833Å helium triplet. Our best-fit model is shown in Figure 2.10, with a a χ^2 of 31.4 for 18 degrees of freedom.

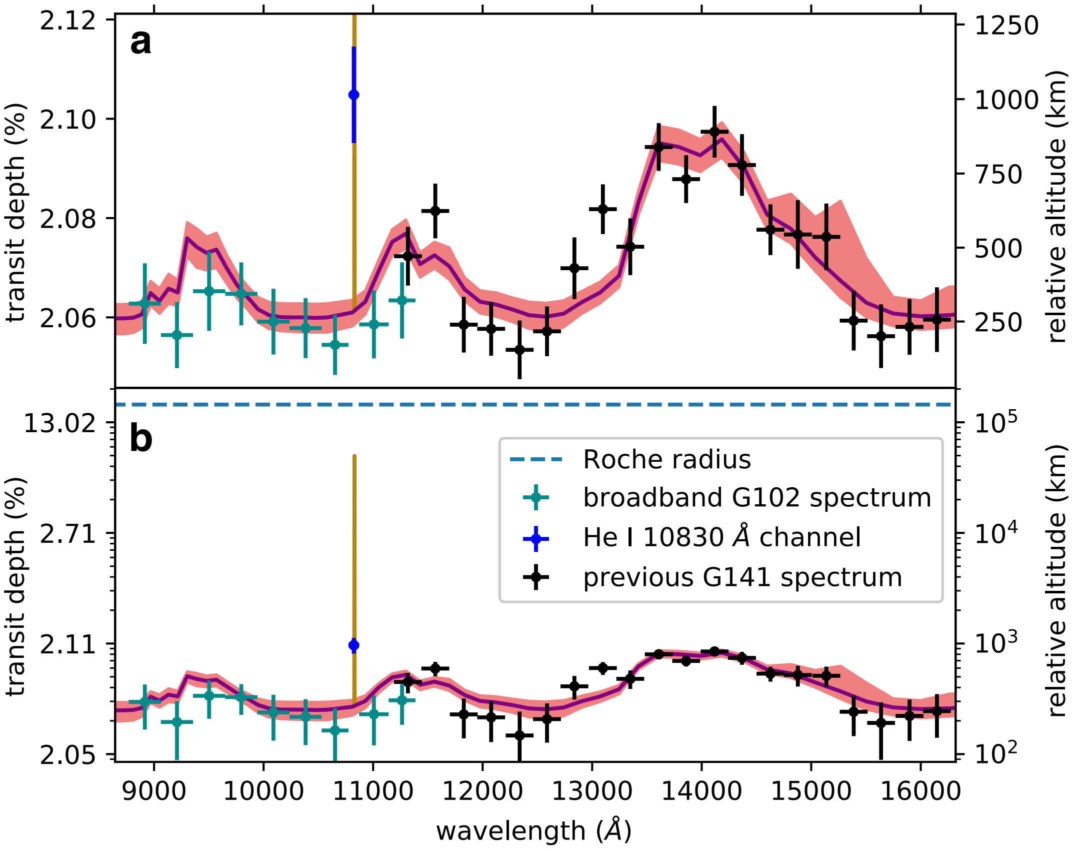

Figure 2.10: Combined near-infrared transmission spectrum for WASP-107b with helium absorption feature. (a) Data plotted on a linear scale. Points with 1σ error bars are from Kreidberg et al. (2018b) and this work, both corrected for stellar activity (see Section 2.5.3). The solid purple line is the best fit lower atmosphere retrieval model from MCMC fits, and the shaded pink areas encompass 68%, 95% and 99.7% of the MCMC samples. The gold line is the best-fit helium 10 830Å absorption profile from our 1-D escaping atmosphere model. (b) Same as (a), on a log scale. The dashed blue line shows the Roche radius.

2.7 Assessing possible causes of the 10 830Å signal

2.7.1 Detector defects and random noise

We checked that the residuals for the pixel columns in each frame do not reveal any obvious anomalies over the narrow 10 833Å helium triplet, which suggests that it is not caused by a detector defects or uncorrected cosmic rays. In addition, the transit depths remained consistent within 0.5σ when we removed 1/3 of the points in the light curves, in several random sub-sets, and re-fit them with the same procedures as described above.

2.7.2 Absorption from other species

The strong absorption line of metastable 2^3S helium at 10 833Å aligns extremely well with the peak of the feature. In the 20Å region surrounding this peak (10 820 to 10 840Å), helium is the only species that contains absorption solely within this wavelength range but nowhere else within the G102 bandpass (8 060 to 11 170Å). There is, for example, a strong silicon absorption line at 10 830Å, and a water line at 10 835Å (vacuum wavelengths) (Kramida 2008), but if either species were the cause of the absorption seen in our transmission spectrum, there would be other similarly strong silicon lines measured at 10 588, 10 606 and 10 872Å , and a water line at 10 929Å, where we see no excess absorption. The other atoms with strong absorption lines near 10 833Å are Np, Cs, Fe, Th, S, Cr, V, Yb, and Cu all of which can be ruled out as they are either radioactive with short half-lives, or have other strong transitions within the the 8 060 to 11 170Å wavelength range that we do not observe. We have also found there to be no species in the ExoMol (Tennyson et al. 2016) or HITRAN/HITEMP (Gordon et al. 2016; Rothman et al. 2010) databases with sufficiently sharp features aligned at 10 833Å. Specifically, we searched the following species: CH_4, CO_2, HCN, NH, CH, OH, PO, NO, VO, TiO, CN, C_2, PH_3,

NH_3, SiO, CaO, H_3^+, CO, H_2CO, C_2H_2, BeH, LiH, HCl, AlO, SO_2, H_2S, PN, KCl, NaCl, CS, CP, PS, MgH, NaH, CrH, CaH, FeH, and ScH. We therefore conclude that absorption by metastable helium at 10 833Å is the most plausible explanation for the signal detected in the narrowband transmission spectrum.

2.7.3 Assessing the Earth's exosphere

Where the Earth's exosphere is illuminated by XUV radiation from the sun, there is metastable helium. At an altitude of ∼500km, HST passes right through the Earths exosphere, and when not in the Earths shadow, will pass through regions containing metastable helium. The change in abundance of the metastable state throughout orbit has been shown to impart time-varying background signal in the 10 833Å line on the timescale of one ∼95 minute spaceraft orbit (Brammer et al. 2014). There is no telluric metastable helium in Earth's shadow, and as expected, there is no significant excess absorption at 10 833 while HST is in Earth shadow (Brammer et al. 2014). It does, however, affect HST measurements at dawn and dusk - i.e. when the spacecraft passes through the solar-illuminated upper atmosphere. The magnitude of the effect is correlated with the solar activity cycle i.e. more activity, more UV, more metastable helium. The effect of spatially-diffuse telluric helium emission on WFC3 slitless spectroscopy is to impart an increased sky background signal across the detector. At the time of the observations, we were approaching solar minimum, and the 10.7 cm radiation (which is a proxy for solar activity) was only 70 solar flux units, sfu (Solar Monitoring Program, Natural Resources Canada). According to the WFC3 instrument report (Brammer et al. 2014) observations only appear significantly affected when the 10.7cm flux is greater than 100 sfu. Nonetheless, to test whether metastable helium at dawn and dusk in the Earth's atmosphere could cause an anomalous absorption feature in our transmission spectrum, we removed the first and last 4 exposures of each orbit which encompasses the initial and final 10 minutes - when HST passed through the illuminated dusk and dawn exosphere, and re-fit the light curves. The results were consistent with previous analysis at less than 1 σ, which indicates that emission from telluric helium is not the cause of the narrowband absorption feature in our data. We note that previous transit spectroscopic studies using G102 (Kreidberg et al. 2015; Wakeford et al. 2018) do not show excess absorption at 10 833Å.

2.7.4 Assessing the stellar chromosphere

We also considered the possibility that the absorption feature we measure at 10 833Å could be a result of stellar activity, since the metastable 2^3S state of helium is formed in the inhomogeneous upper chromospheres and coronae of stars via photoionisation, recombination, and collisional excitation. The planet passing over quiet regions with less 10 833Å helium absorption could in theory increase the relative transit depth at this wavelength and thus mimic an exoplanet atmospheric feature. Theoretical models of chromospheres (Andretta & Giampapa 1995; Andretta & Jones 1997), predict the maximum equivalent width of the 10 833 Angstrom helium line in the spectra of F- to early K-type stars to be ∼0.4Å. Being a K6 star, WASP-107 lies just outside the valid range of spectral types for this model. However, in the following section we show that in order to match our observed transmission spectral feature, the nominal chromospheric absorption at 10 833Å of the WASP-107 host star would need to be five times stronger than any isolated (i.e. non-multiple), main-sequence dwarf star measured to date. After searching the literature for all 10 833Å helium triplet equivalent width measurements of isolated dwarf stars, we found over 300 measurements of over 100 distinct stars, including 23 measurements of 11 different stars of similar spectral type to WASP-107 (K5-K7). We found no measurements greater than 0.409Å (Vaughan & Zirin 1968; Zirin 1982; Zarro & Zirin 1986; Sanz-Forcada & Dupree 2008; Takeda & Takada-Hidai 2011; Andretta et al. 2017; Isaacson & Fischer 2010). We took an additional measurement of the K6 star GJ380 with NIRSpec on Keck, which was found to have an equivalent width of 0.311Å (A. Dupree, private communication). Furthermore, it has been shown (Andretta & Jones 1997; Andretta et al. 2017) that the equivalent width of the 10 833Å line is related to that of another neutral helium absorption line, at 5,876Å. The 5 876Å line is produced by the transition from the 2^3D to the 2^3P state. As such, the 5 876Å line forms in the same regions of the stellar chromosphere as the 10 833Å triplet (which corresponds to the 2^3S to 2^3D transition). Figure 2.11 shows the equivalent width measurements of the 10 833 and 5 876Å lines in a survey of 31 FGK stars (Andretta et al. 2017). A strong correlation is apparent. To investigate the 5 876Å helium line of WASP-107, we co-added high-resolution spectra obtained with the HARPS spectrograph (ESO programme 093.C-0474(A)). These spectra cover a wavelength range of 3 800 to 6 900Å (See Figure 2.11). We fit for the equivalent width of the 5 876Å helium line in the co-added spectrum, with the result indicated on Figure 2.11 as a red shaded region. We find the equivalent width of this feature is similar to that measured for other single dwarf stars, with no evidence of unusual activity. Given the well-established correlation between the equivalent widths of the 5 876 and 10 833Å helium lines noted above, this is further evidence against the WASP-107 host star having an abnormally deep 10 833Å line. In addition, we measured the S-index for WASP-107 from the HARPS spectra, and found a night-averaged value of S_{HK}=1.26±0.03, which is a moderate value for a K6 star (Isaacson & Fischer 2010). We therefore adopt the maximum equivalent width of 0.4Å to estimate an upper limit for the amplitude of a feature that could be caused by un-occulted 10 833Å helium absorption of stellar origin in our 98-Å -wide spectroscopic channel. We consider the limiting case in which WASP-107b occults only quiet regions of the star, where we assume there is no 10 833Å absorption. This is the scenario in which the maximum amount of stellar continuum flux at 10 833Å would be blocked out by the planet, which we treat as a fully opaque disk. We estimate the increased transit depth to be

$$D_{\mathrm{activity}} = \frac{A_{\mathrm{pl}}}{1 - W_{\mathrm{He}}/W_{\mathrm{bin}}} = 2.064 \pm 0.005\% \qquad (2.1)$$

where A_{pl}=2.056±0.005% is the fraction of the stellar area occulted by the planet; W_{He}=0.4Å, is the maximum equivalent width of the stellar absorption feature; and W_{bin} is the width of the spectral bin (i.e. 98Å). This gives an upper limit of the

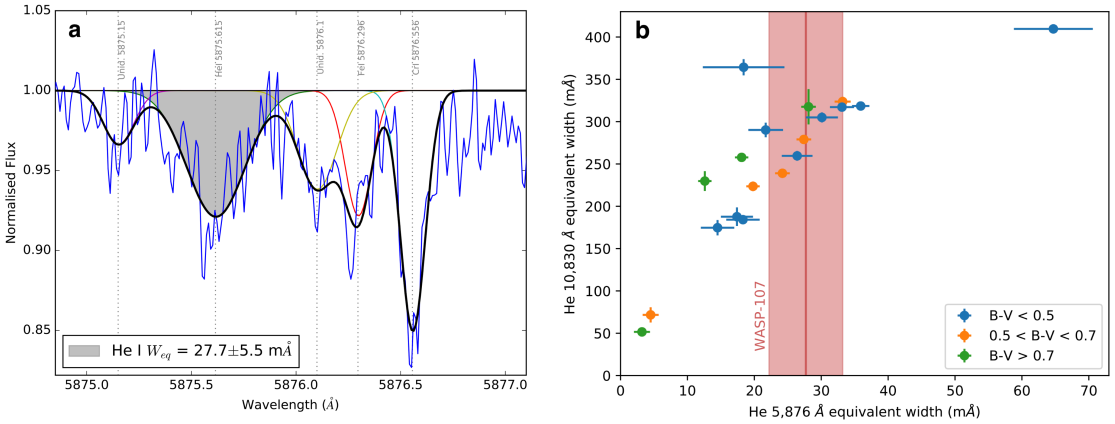

Figure 2.11: Equivalent widths of helium 5 876Å and 10 830Å lines. (a) Measurements for 30 stars of different colour indices, from Andretta et al. (2017). These two helium lines are expected to form in the same regions of stellar atmospheres and their equivalent widths are clearly correlated. Our 5 876Å measurement for WASP-107 is plotted as a red line. Red shaded region shows the 1 σ error. Equivalent width measurement and 1 σ error of the 5 876Å line for WASP-107 (B-V > 0.7) from HARPS spectra is shown as red shaded region. (b) Co-added spectra from HARPS radial velocity campaign for WASP-107 around the 5 876Å line of metastable helium. Lines fit with Gaussian profiles.

feature caused by stellar activity, $\delta D_{\text{activity}} = D_{\text{activity}} - A_{\text{pl}} = 0.008 \pm 0.005\%$, which is less than one fifth of the measured size of the feature ($0.049 \pm 0.011\%$). We therefore conclude that the observed absorption feature cannot be caused by stellar chromospheric spatial inhomogeneity alone.

2.7.5 Resolution-Linked Bias

If an absorption line overlaps in both a stellar and planetary atmosphere spectrum, and the line is unresolved in the measured transmission spectrum, then the planetary absorption can be underestimated. The effect is called Resolution Linked Bias (RLB) (Deming & Sheppard 2017). For the 10 833Å line in the WASP-107 system this dilution effect will compete with the possible over-estimation of the signal from unocculted chromospherically active regions (as described in the Assessing the stellar chromosphere section). The magnitudes of both effects will depend on whether the planet transits in front of active or quiet regions of the star. The RLB effect would be largest if the planet transited only chromospherically active regions (which have the highest 10 833Å absorption). We estimated the magnitude of the RLB effect in this limiting case following the method described in Deming & Sheppard (2017), and assuming an equivalent width of 0.4Å for the 10 833Å stellar line. For a measured absorption excess of 0.049±0.011% in a 98Å bin centred on the 10 833Å line, we could be underestimating the planetary absorption by up to 0.009% (i.e. about one fifth of the measured signal). However, without knowledge of which part of the chromosphere the planet transits; the stellar line profile; and the velocity structure of the planetary helium signature, we cannot accurately estimate the magnitudes of the competing effects.

2.7.6 Stellar flares

The He 10 833Å line appears in emission in solar- (and presumably stellar-) flares (Li et al. 2007), so active stars like WASP-107 could show short-term variability in the line, which may be difficult to disentangle from a transiting planetary signal (Czesla et al. 2015). Flares are unlikely to wholly mimic the signal we detect, since the planet would need to pass in front of flaring regions of the star throughout the duration of the transit. Instead, unocculted flares could dilute He 10 833Å atmospheric absorption. Visual inspection of the raw light curve of the spectroscopic channel centred on 10 833Å shows no evidence of flare events. Additionally, the pre- and post- transit flux levels agree with each other, which would not be the case if there was significant 10 833Å emission from the tail of a flare. As a precaution, we re-produced the narrowband transmission spectrum around the 10 833Å line using different combinations of the out-of transit baseline: firstly with only orbits 2 and 4, then with orbits 1 and 3, and then orbits 2 and 5. All three cases gave a 10 833Å absorption feature consistent to within 1σ of our full fit.

2.7.7 Photospheric spots and faculae

To quantify the effect of a heterogeneous photosphere on the transmission spectrum around 10 833Å, we used a variability modelling method (Rackham et al. 2017, 2018) which uses an ensemble of model stellar photospheres with randomly located active regions to provide estimates of the fraction of the stellar surface covered by photospheric spots and faculae for a given rotational variability amplitude. While variability monitoring traces only the non-axisymmetric component of the stellar heterogeneity and thus provides a lower limit on active region covering fractions (Rackham et al. 2018), this numerical approach provides a more complete understanding of the range of covering fractions that may correspond to an observed variability level. The model describes the integrated full-disk spectrum by the combination of three components: the immaculate photosphere, spots, and faculae. We used three spectra interpolated from the PHOENIX model grid (Husser et al. 2013) with $\log g = 4.5$ and $[M/H] = +0.02$ and different temperatures to represent the three components. Following Rackham et al. (2018), we set the photosphere temperature, $T_{\rm phot}$, to the effective temperature of the star ($T_{\rm eff} = 4\,430$ K; Anderson et al. 2017) and adopt scaling relations for the spot temperature $T_{\rm spot}$ (Berdyugina 2005; Afram & Berdyugina 2015), and faculae temperature $T_{\rm fac}$ (Gondoin 2008). Thus, the temperatures of the three components are $T_{\rm phot} = T_{\rm eff} = 4\,430$ K, $T_{\rm spot} = 0.73 \times T_{\rm phot} = 3\,230$ K, and $T_{\rm fac} = T_{\rm phot} + 100$ K $= 4\,530$ K. WASP-107bs discovery paper (Anderson et al. 2017) reports a 17-day periodic modulation with a 0.4% semi-amplitude (0.8% full-amplitude) for WASP-107. Assuming a typical spot radius[2] of $r_{\rm spot} = 2°$, we find the reported rotational variability could be caused by a spot filling fraction of $f_{\rm spot} = 4^{+9}_{-2}\%$ (1σ confidence interval) if the variability is due to spots alone. In the more realistic case in which spots and faculae are both contributing to the variability, we find $f_{\rm spot} = 8^{+6}_{-3}\%$ and $f_{\rm faculae} = 53^{+15}_{-12}\%$. The covering fractions we report are means over the entire model photosphere. They do

---

[2] Note that we do not know the size of the spots. Decreasing the spot size while maintaining the same filling fraction will reduce the effect of the spots on the transmission spectrum, as the photoshere will appear slightly more homogeneous. We chose to use the relatively large spot radius of 2°, to err on the side of conservatism.

not take into account relative over- or under-abundances of magnetic features on the Earth-facing hemisphere during a transit. Therefore, in the worst case scenario, they could underestimate the hemispheric covering fractions by a factor of 2. However, the 1-σ confidence intervals, which are derived from 100 model realizations with randomly selected active region locations, are deliberately conservative to account for this. Figure 2.12 shows how unocculted photospheric stellar heterogeneities could affect the transmission spectrum, assuming the planet transits a chord of immaculate photosphere. The stellar contamination factor, ε, on the y-axis is multiplied by the true $(R_{\mathrm{p}}/R_{\mathrm{s}})^2$ transit depth to produce the observed transmission spectrum, i.e. $\varepsilon > 1$ means the observed transit depth is deeper than expected from the planetary atmosphere model. The spots+faculae model does not predict an increase in transit depth at 10 833Å . No sharp features around 10 833Å are apparent. Instead, the model predicts transit depths should be inflated by $\sim 1\%$ across the full wavelength range of G102 with perhaps some features apparent at ∼8 500Å and 8 900Å (for this reason we only use the 8 780 - 11 370Å region in our full transmission spectrum, even though the G102 throughput extends down to 8 000Å). The strong absorption feature we measure is therefore unlikely to be caused by photospheric inhomogeneity.

2.8 Upper atmosphere models

2.8.1 1D escaping atmosphere model

Here we give a brief overview of the first model used to investigate the narrowband transmission spectrum at 10 833Å , which is presented and described in more detail in Oklopčić & Hirata (2018). This 1D model is based on the assumption that a thermosphere of a close-in exoplanet can be well represented by the density and velocity profile of an isothermal Parker wind driven by gas pressure (Parker 1958). We assume a composition of atomic hydrogen (90% by number) and helium (10%). We find the solution for the hydrogen ionization balance and the distribution of helium atoms in the ground, excited 2^3S, and ionized states. The physical processes

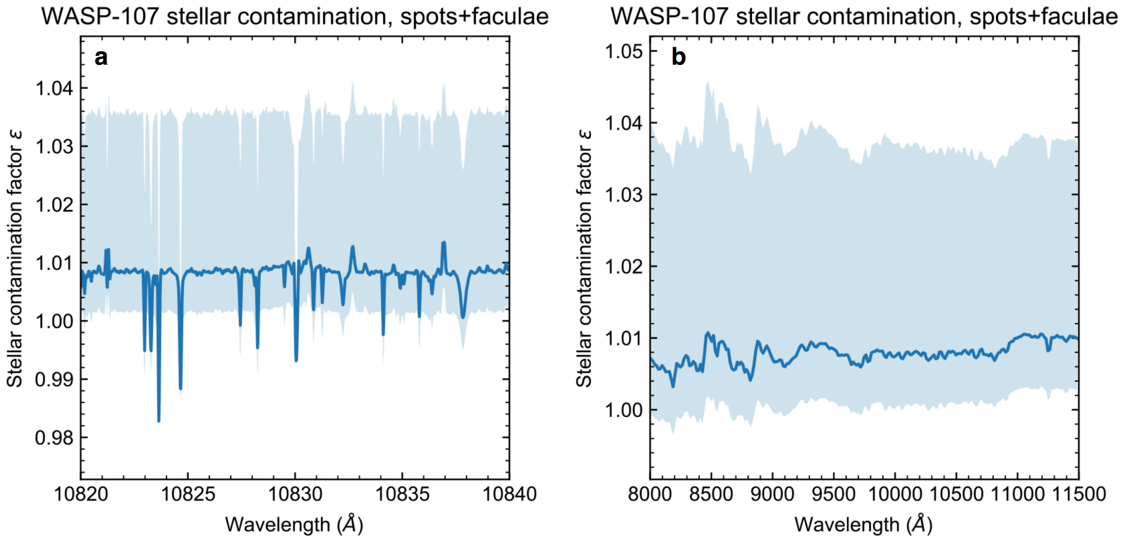

Figure 2.12: The effects of an inhomogeneous photosphere on the transmission spectrum of WASP-107b. Lines show the stellar contamination produced by unocculted spots and faculae. Shaded regions indicate the 1σ uncertainty on the stellar contamination due to the uncertainty on spot and faculae covering fractions. (a) The region around the 10 833Å (vacuum wavelength) helium triplet at the resolution of the PHOENIX spectra (R=500 000). The strong line at 10 830Å is a photospheric silicon line. (b) The full G102 wavelength range in 15Å bins.

taken into account in the helium balance are photoionization from the ground and 2^3S states, recombination to the singlet and triplet states, collisional transitions between the triplet 2^3S state and states in the helium singlet ladder, which includes collisions with both free electrons and neutral hydrogen atoms, and the radiative decay from the 2^3S state to the ground state. The photoionization rates are calculated using the UV stellar flux of a K6 star HD 85512 taken from the MUSCLES survey (France et al. 2016) (version 2.175,76), placed at the orbital distance of WASP 107b The equations used to compute the hydrogen/helium distributions, along with all the relevant reaction rate coefficients and cross sections, are described in Oklopčić & Hirata (2018). We only changed the input parameters such as the mass and radius of the planet and its host star, as well as the input stellar spectrum, so that they match the properties of WASP 107b. Based on the obtained density profile of helium in the 2^3S state, we calculate the optical depth and the in-transit absorption signal at 10 833Å, assuming that a planet with a spherically symmetric thermosphere transits across the center of the stellar disk. For a planet of given mass and radius, the wind temperature and the total mass loss rate are free parameters in the model. Based on the results from Lecavelier des Etangs et al. (2004) and Salz et al. (2016), we explore a temperature range between 5 000 - 13 000 K. In order to produce the absorption signal consistent with our measurement, the required mass loss rate is between 10^{10} and 3×10^{10} g/s. Our best fit model is shown in Figure 2.13.

2.8.2 3D escaping atmosphere model

Our second model has previously been used to interpret the escaping exosphere of the Neptune-mass exoplanet, GJ436b (Ehrenreich et al. 2015; Bourrier et al. 2016). It considers neutral helium atoms that are released from the top of the thermosphere and subjected to planetary and stellar gravity, radiation pressure, and photoionization. We found that the data are well explained by 2^3S helium atoms escaping at a rate of 10^6-10^7 g/s. Stellar radiation pressure on the escaping helium atoms is stronger than the counter-balancing stellar gravity by a factor of approximately 10 and 50 for the weakest and strongest of the 10 833Å triplet lines, respectively. Thus the gas blows away so swiftly as to form a tail nearly aligned with the star-planet axis. Our best fit model is shown in Figure 2.13.

2.9 Discussion

The broadband transmission spectrum is consistent with a previous transmission spectrum for WASP-107b obtained using the WFC3 G141 grism, which covers the 11 000 - 16 000Å wavelength range (Kreidberg et al. 2018b). The latter exhibits a muted water absorption band centred at 14 000Å, with an otherwise flat spectrum implying an opaque cloud deck. After applying a correction for stellar activity variations between the G102 and G141 observation epochs, the G102 spectrum aligns with the cloud deck level inferred from the G141 spectrum (Figure 2.10). The helium triplet has an expected width of approximately 3Å, whereas the resolution of the G102 grism is 67Å (∼3 pixels) at 10 400Å (Kuntschner et al. 2009). Therefore, to make a finely-sampled transmission spectrum, we shifted each of the 20 narrowband

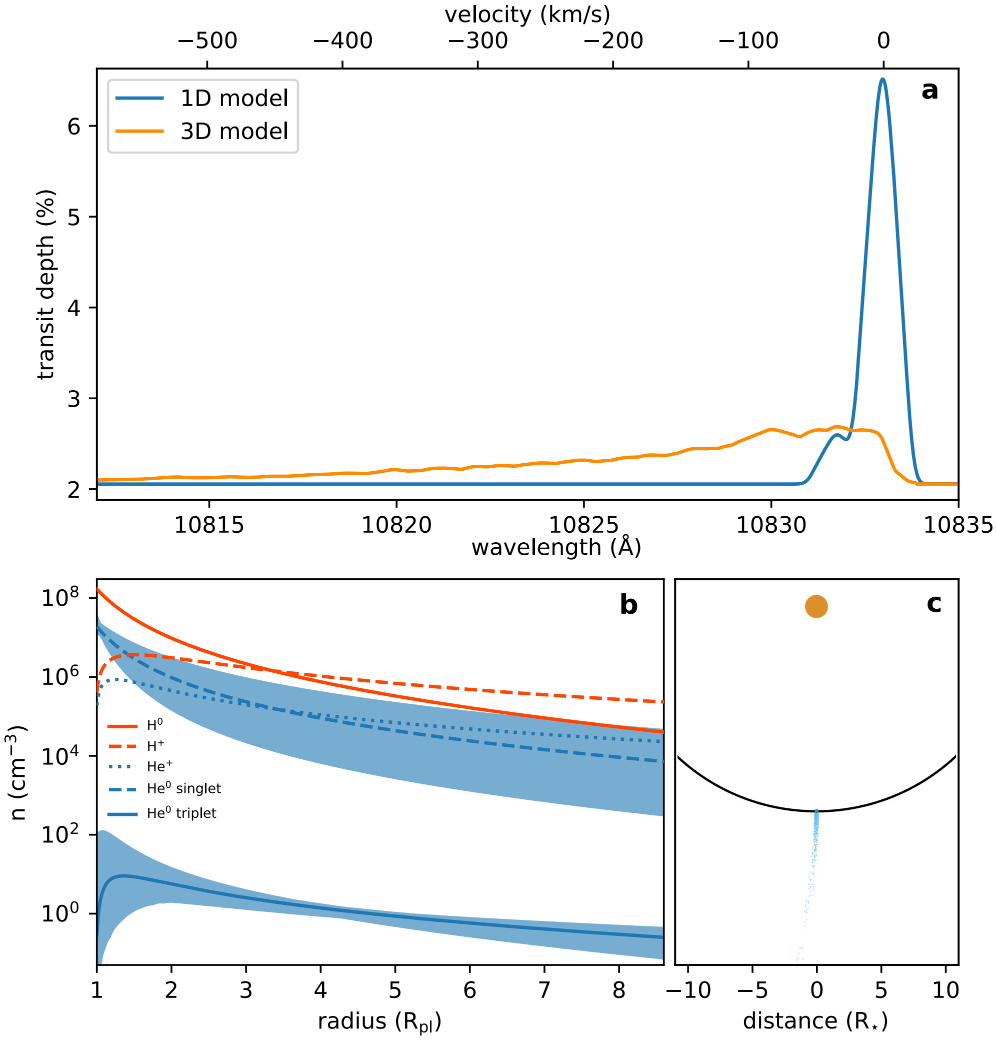

Figure 2.13: Results from two models of WASP-107b's upper atmosphere. (a) Best-fit absorption profiles of the helium 10 833Å triplet line from the 1-D (blue), and 3-D (orange) models. Both reproduce the measured excess absorption of 0.049±0.011% in a 98Å bin. Higher-resolution observations will resolve the profile shape, and further constrain the velocity of the planetary wind. (b) Radial number density profiles of different atmospheric species from the 1-D model, shaded blue regions are 1σ errors. (c) Top-down view of the planetary system from the 3-D model, showing a comet-like tail of 2^3S helium shaped by stellar radiation pressure.

channels by 1 pixel with respect to the adjacent channel along the wavelength axis. The narrowband transmission spectrum peaked when the binning was most closely centred at 10 833Å (Figure 2.7), as expected if absorption by helium in the planetary atmosphere was responsible for the signal. To estimate the amplitude of the absorption feature, we focussed on 5 non-overlapping channels centred on 10 833Å. All but one of the channels were consistent with a baseline transit depth level of 2.056 ± 0.005 %. The single exception is the channel centred on the 10 833Å helium triplet, for which the transit is visibly deeper than for the surrounding channels, as shown in Figure 2.14, and we obtained $(\mathrm{R_p}/\mathrm{R_s})^2$=2.105 ± 0.010 %. We ruled out various alternative explanations for the signal, including other absorbing species, helium in the Earth's atmosphere, and the occultation of inhomogeneities in the stellar chromosphere and photosphere.

The metastable helium probed by 10 833Å absorption forms high up, at μbar - mbar pressures in planetary atmospheres, where stellar XUV radiation is absorbed (Christie et al. 2013). On the other hand, absorption of the neighbouring continuum occurs deeper in planetary atmospheres, at mbar - bar pressures. Therefore, to interpret the broadband (continuum) and narrowband (∼10 833Å) transmission spectra, we used separate lower- and upper- atmosphere models. For the combined G102 and G141 broadband spectrum (with the 10 775 - 10 873Å range removed), we performed an atmospheric retrieval analysis using our one-dimensional radiative transfer code, ATMO (Amundsen et al. 2014; Tremblin et al. 2015) (see Figure 2.10). We found the broadband data were well explained by a grey absorbing cloud deck across the full 8 780 - 11 370Å wavelength range, in addition to H_2O absorption. We obtained a volume mixing ratio for H_2O of 5×10^{-3} - 4×10^{-2}, consistent with previous estimations (Kreidberg et al. 2018b). We investigated the narrowband transmission spectrum using two numerical models for the upper atmosphere of WASP-107b. Our first, 1D model (Oklopčić & Hirata 2018) solves for the level populations of a H/He Parker wind, and suggests that WASP-107b is losing its atmosphere at a rate of 10^{10} - 3×10^{11} g/s, corresponding to ∼0.1 - 4% of its total mass every billion years. Our second, 3D model (Ehrenreich et al. 2015; Bourrier

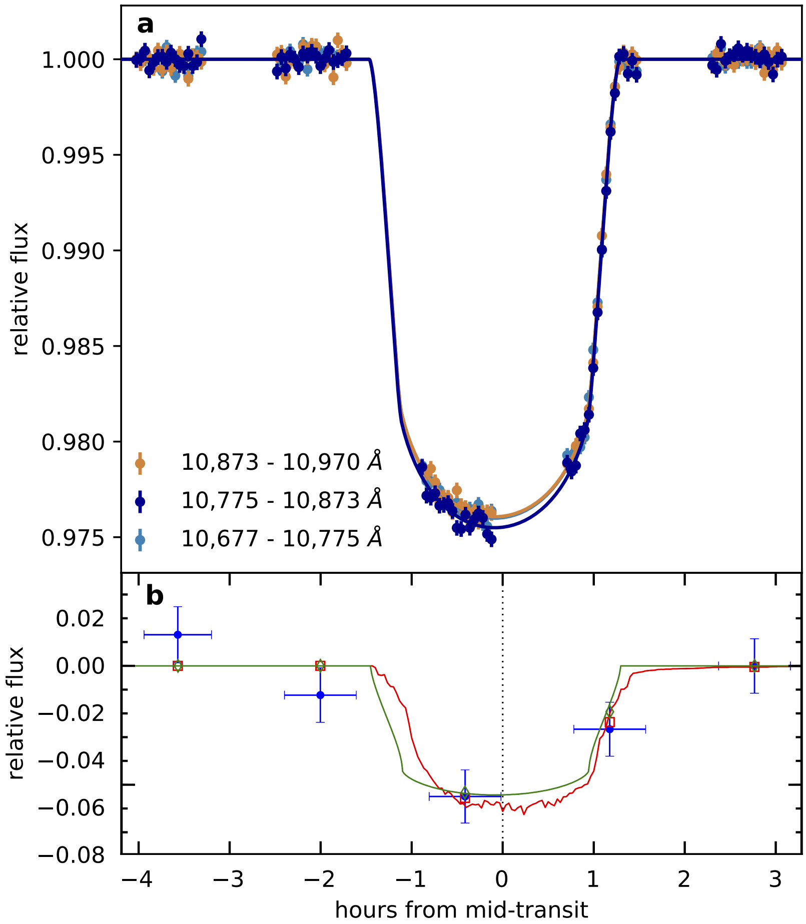

Figure 2.14: Transit light curves for three 98Å -wide spectroscopic channels. (a) Dark blue points are from the channel centred on the He I 10 833Å line, gold and light blue points are from the two adjacent channels. All have 1σ error bars. The transit depth of the blue light curve is visibly deeper. (b) Binned difference between the 10 775 - 10 873Å channel light curve, and the average of the two adjacent channels (blue points, 1σ errors), highlighting the excess absorption. It is well explained by both our 1D (green line) and 3D (red line) escaping atmosphere models.

et al. 2016) suggests an escape rate for metastable helium of 10^6 - 10^7 g/s (for comparison, the 1D model gives an escape rate of $\sim 10^5$ g/s for 2^3S helium). It also suggests that stellar radiation pressure blows away the escaping helium atoms so swiftly as to form a tail nearly aligned with the star-planet axis, which could explain the lack of post-transit occultation detected in our data (Figure 2.14). The radiation pressure should also blue-shift the absorption signature over hundreds of km/s, which may be observable at higher spectral resolution (Figure 2.13). Atmospheric mass-loss can substantially alter the bulk composition of a planet. For example, there is evidence that atmospheric escape is responsible for the observed dearth of highly-irradiated super-Earth and sub-Neptune exoplanets with sizes between 1.6 and 2 Earth radii (Lopez et al. 2012; Owen & Wu 2013; Jin et al. 2014; Chen & Rogers 2016; Fulton et al. 2017). In order to calibrate theories of planet formation, and assess whether these planets have substantial H/He envelopes, it is necessary to understand how atmospheric mass-loss affects the subsequent evolution of bodies that start with significant atmospheres. Empirical constraints such as the one presented here for WASP-107b are therefore crucial for retracing evolutionary pathways and interpreting the present day population of planets (Lopez & Fortney 2014). To date, extended atmospheres have been detected a handful of exoplanets by targeting absorption lines in the UV (Vidal-Madjar et al. 2003; Lecavelier Des Etangs et al. 2010; Kulow et al. 2014; Fossati et al. 2010; Vidal-Madjar et al. 2004; Bourrier et al. 2016), and the optical H-alpha line Jensen et al. (2012); Yan & Henning (2018). Our observations of WASP-107b in the 10 833Å line provide not only the first detection of helium on an exoplanet, but also the first detection of an extended exoplanet atmosphere at infrared wavelengths. This result demonstrates a new method to study extended atmospheres which is highly complementary to the previously detected absorption lines.

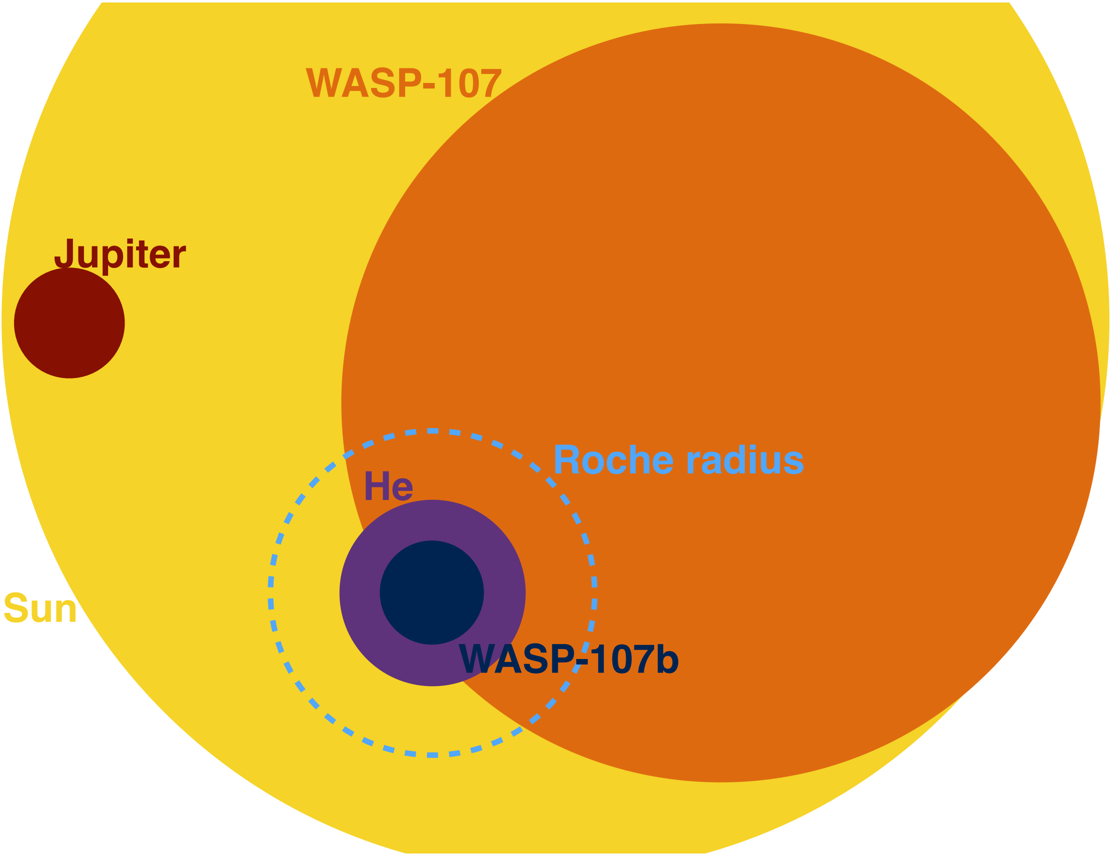

Figure 2.15: Cartoon showing relative size of WASP-107b and its host star compared to Jupiter and the sun. If the helium absorption were in an opaque disk it would reach up to around 1.6 Jupiter radii, indicated by the blue disk. This falls inside the Roche radius, indicated by the dashed circle.

2.10 Confirmation

Observations targeting the 10 833Å helium triplet are possible from the ground with existing high-resolution infrared spectrographs, and a flurry of ground-based detections have already been made (Allart et al. 2018; Salz et al. 2018; Nortmann et al. 2018). Our detection of WASP-107b's extended helium atmosphere has been confirmed by Allart et al. (2019) using CARMENES (see Figure 2.16). The CARMENES data are at high enough resolution to resolve the double-peaked shape of the line line triplet. The peak of the absorption feature measured by CARMENES corresponds to a transit depth of around 7±1%, which is consistent with our inferred depth of 6±1% in the core of the line (see Figure 2.17). We did not observe a significant blueshift, which suggests that the 3D atmosphere model discussed in Section 2.8.2 may be missing important physical processes, like hydrodynamical interactions

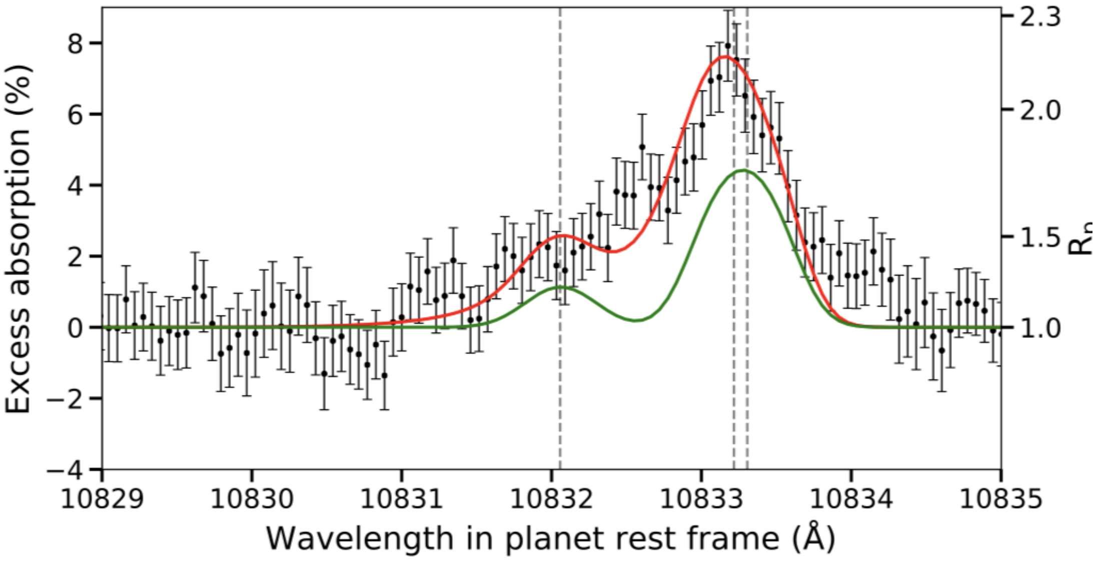

Figure 2.16: High-resolition transmission spectrum for WASP-107b measured by CARMENES, a ground-based telescope (Allart et al. 2019). The 10 830Å line is resolved, and the absorption peaks at around 7%, consistent with our HST observations.

of the flow.

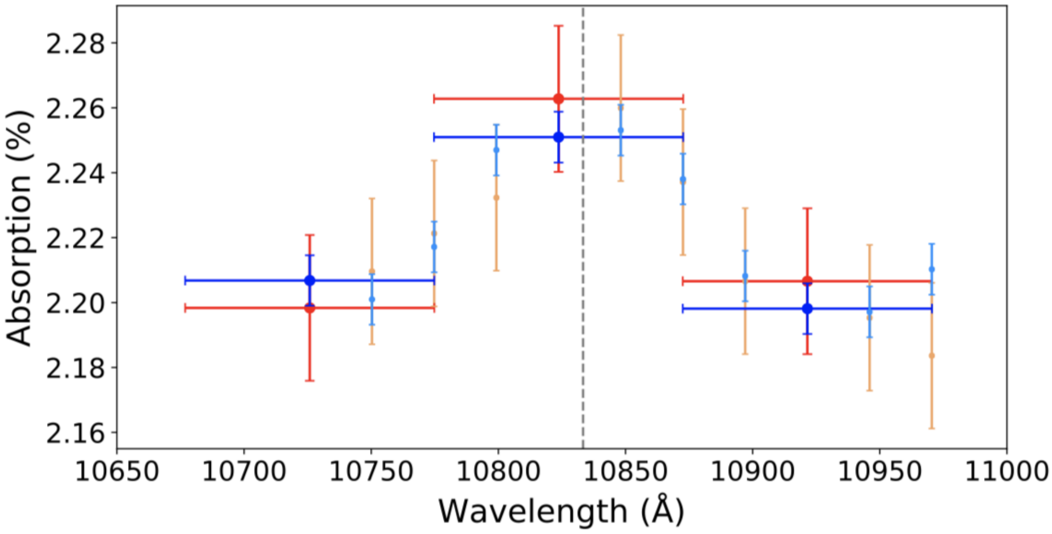

Figure 2.17: Comparison between the HST/WFC3 dataset of discussed here in blue with the degraded high-resolution CARMENES dataset from (Allart et al. 2019) in red. Light blue points are CARMENES data binned to 98Å , orange points are HST data supersampled to 98Å The vertical grey dashed line is the helium triplet transition. Figure from (Allart et al. 2019).

Chapter 3

The hot: near-infrared phase-curve of the ultra-hot WASP-19b

3.1 Statement of contribution

For the work covered in this Chapter, J. J. Spake led the analysis of data from HST proposal GO-13431 (PI Huitson). T. Evans provided a reduction code for WFC3 that was adapted by J. J. Spake.

3.2 Introduction

We observed a near-infrared (1.0 - 1.7 μm) phase curve of the hot Jupiter WASP-19b using HST's WFC3, in order to investigate how heat is transported around the planet's atmosphere at pressures of around 1 bar. WASP-19b is an ideal target for phase curve observations with WFC3 for several reasons. Firstly, it is one of the shortest-period gas giant planets known, with an orbital period of 0.789 days (Hellier et al. 2011), so relatively few HST orbits are required to observe its phase curve. Secondly, its proximity to its host star means that WASP-19b has a relatively high equilibrium temperature of around 2 050 K; meaning its dayside should have a favourable flux contrast with its host star in the near-infrared - indeed it has one of the deepest secondary eclipses measured in H band (which is centred on $\sim 1.6\mu$m), at $0.259^{+0.046}_{-0.044}\%$ (Anderson et al. 2010). We can therefore expect a large phase curve amplitude in the WFC3 bandpass. Additionally, a previous observation of WASP-19b's transit taken with WFC3 shows a transmission spectrum dominated by water absorption, and little evidence for grey opacity sources at NIR wavelengths, like clouds (Huitson et al. 2013). The lack of clouds, at least at the planet's terminator, suggests that observations in the WFC3 wavelength range are able to penetrate deeper into the planet's atmosphere than has previously been achieved, to a region expected to be dominated by convective (rather than radiative) processes (Showman & Guillot 2002).

Wong et al. (2016) observed two phase curves of WASP-19b, one each in the 3.6 and 4.5 μm channels of Spitzer's IRAC. For WASP-19b, radiation emitted at these wavelengths is expected to originate mainly from high altitudes in the atmosphere, corresponding to pressures between 10^{-2} and 10^{-4} bar. This can be seen in the contribution functions from 1D radiative transfer models, as shown in Figure 3.1.

The 3.6 and 4.5 μm phase curves both show large day-night temperature contrasts of around 1 000K, and small but statistically significant hotspot offsets of $10.5 \pm 4.0°$ and $12.9 \pm 3.6°$, respectively. The phase curve data and best-fitting models from Wong et al. (2016) are shown in Figure 3.2. These observations are consistent with predictions from GCM models from Kataria et al. (2016), for pressures of 1 mbar. WASP-19b is a hot, tidally locked exoplanet - which means it should have strong, equatorial winds - but the GCM models and Spitzer observations both suggest that its upper atmosphere radiates away much of its heat before it is moved around the planet. As Figure 3.1 shows, our WFC3 observations likely probe deeper in the atmosphere, where the radiative-to-advective timescale ratio is expected to be higher.

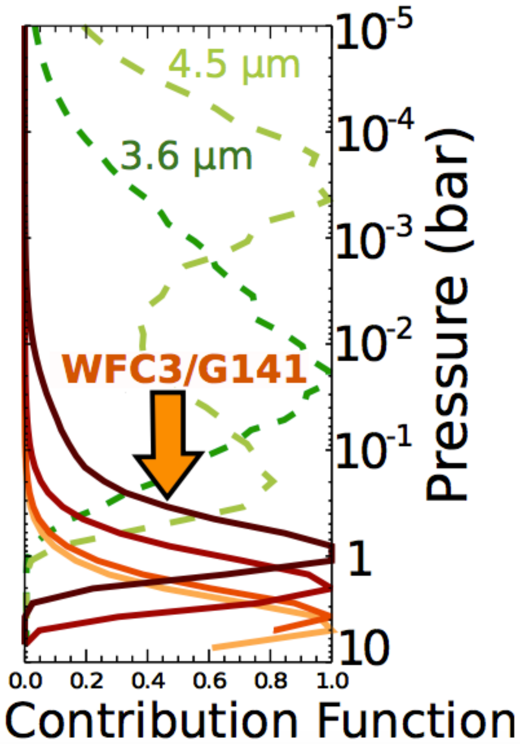

Figure 3.1: Normalized contribution functions for different bands at different pressures from a 1D radiative-transfer model for WASP-19b, assuming a solar-composition atmosphere. Figure from T. Kataria (private communication, 2018).

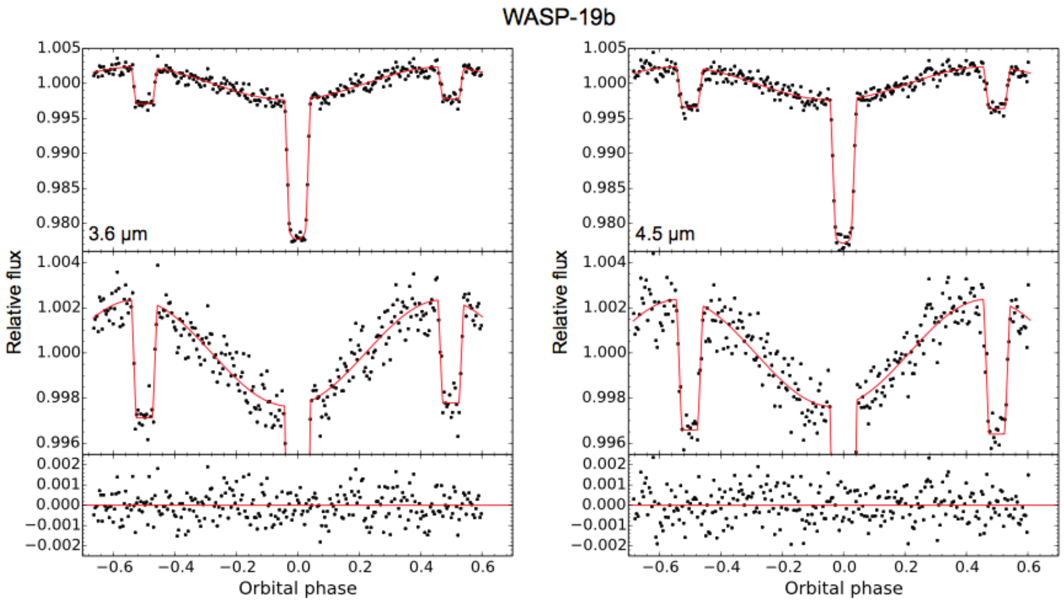

Figure 3.2: Previous Spitzer phase curve observations of WASP-19b from Wong et al. 2016

The aim of taking a spectroscopic phase curve with WFC3 was to simultaneously probe different pressures of WASP-19b's atmosphere. For example, radiative transfer models suggest that for a cloud-free atmosphere we can expect that wavelengths around 1.2 - 1.3 μm - which fall between water absorption bands, which are themselves weaker than 3 - 5 μm water bands - will correspond to photospheric pressures of around 10 bar. Conversely, emission from the 1.4 - 1.5 μm range, where water opacities are stronger, should predominantly originate from pressures around 1 bar (e.g. Fortney 2005; Fortney et al. 2008, 2010, see Figure 3.1). However, the analysis discussed here focuses on the broad-band phase curve encompassing the entire 1.0 - 1.7 μm range.

3.3 Observations and data reduction

We observed WASP-19 during three visits, each visit containing five consecutive orbits. The three visits were shifted in phase to cover 70% of the orbital period, including one transit and one eclipse event. This partial phase curve covered the region of the expected hotspot and was significantly easier to schedule than a full orbit phase curve. We scheduled overlap between the three visits to facilitate their combination onto a consistent baseline.

We used WFC3's G141 grism, in spatial scan mode. We used a 512×512 pixel subarray of the detector to reduce overheads. For every observation we used an exposure time of 46.7 seconds, and we took 26 integrations per HST orbit, which gave 390 spectra in total. We used a scanning rate of 0.02 arcsec/second. The maximum count rate in every spectrum was no more than 30 000 counts per pixel, which was well within the observed linear regime of the detector (non-linearity is observed to begin at $\sim$ 42 500 counts).

We followed the same procedure as described in Chapter 2 for the data reduction. Namely: the raw frames were first reduced with the automatic CalWF3 pipeline. The 1-D spectra were then extracted following standard methods (Evans et al. 2016): building up flux counts by summing the difference between successive non-destructive reads. We removed the background from each read difference by subtracting the median of a box of pixels uncontaminated by the spectrum. We found the flux-weighted centre of each scan and set to zero all pixels more than 20 rows away from the centre in the cross-dispersion axis, which removes many cosmic rays. The remaining cosmic rays were flagged by finding 4 σ outliers relative to the median along the dispersion direction. We replaced each flagged pixel with the median along the dispersion direction, re-scaled to the count rate of the cross-dispersion column. Since the scans are visibly tilted from the dispersion axis, we used the IRAF package Apall to fit the trace of the 2-D scans and extract 1-D spectra. We found the wavelength solutions by cross-correlating the extracted spectra with an ATLAS model stellar spectrum (Castelli & Kurucz 2004) which most closely matches WASP-19 ($T_{\rm eff}$ = 5 500 K, log g = 4.5 cgs) modulated by the G141 grism throughput.

To make white light curves we summed the total counts in the individual 1D spectra. Figure 3.3 shows the raw light curves for the three visits.

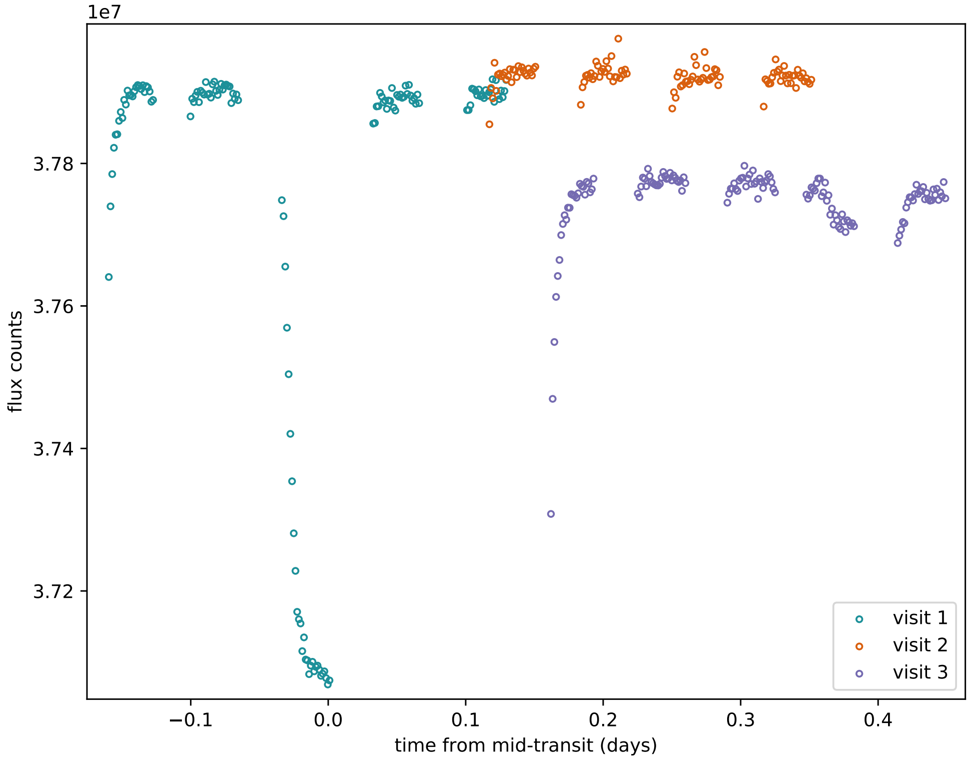

Figure 3.3: Raw white light curves for each of the three visits for WASP-19b. The three visits were taken several days apart, but here they are shown on a time scale relative to the mid-transit time for each visit.

3.4 Phase curve fitting

3.4.1 Phase curve model

To model the shape of the phase curve we used the PYTHON package SPIDERMAN[1] (Louden & Kreidberg 2018). SPIDERMAN is the first open-source code that can quickly model exoplanet phase curves and secondary eclipses consistently, so it can be used to directly fit the data to a physical model. Previous works have frequently fit phase curve and secondary eclipse data to non-physical models like sine curves modulated by an independent eclipse model (e.g. Cowan & Agol 2008). SPIDERMAN projects a specified temperature map onto the visible sphere of a model planet, and directly calculates the secondary eclipse and phase curve simultaneously. It can model arbitrary temperature maps, but we chose to use its implementation of Zhang & Showman (2017)'s physically-motivated, analytical model of the 3D temperature distribution of exoplanet atmospheres. It is a fairly simple, cloud-free, kinematic model which nevertheless closely replicates the temperature distributions of computationally-expensive GCMs with only 3 free parameters. The three parameters are: the temperature of the night side of the planet, T_{n}; the difference in temperature between the dayside and the night side, ΔT; and the ratio between the advective and radiative timescales of the atmosphere, ξ. We justify chosing this model by noting that Huitson et al. (2013) see no evidence for near-infrared opacity sources - i.e. clouds - in their transmission spectrum of WASP-19b. Considering the difficulty of teasing information from small-amplitude exoplanet phase-curve data, using a consistent, cloud-free model may provide us with basic insights into the physical nature of WASP19b's atmosphere.

3.4.2 Fitting procedure

We first constructed the white light curve for each of the three visits by summing all of the counts in the individual 1D spectra, then normalising each the light curve

---

[1] Freely available at https://github.com/tomlouden/spiderman

by the median values outside of the transit and eclipse.

To correct for WFC3's systematics, we followed the procedure used in Chapter 2 and used a physically-motivated systematics model, the RECTE model (Zhou et al. 2017), which accounts for two populations of charge traps in individual pixels of the detector and successfully replicates the ramp-like features that dominate the systematics. For each visit this gives four parameters for the charge trapping model - the initial number of populated slow and fast traps s_{pop} and f_{pop}, and the changes in the two populations between each orbit, δs and δf. We also fit for a constant offset between the flux level of each dataset and the model baseline, which gives 3 additional free parameters: F_1, F_2, and F_3.

SPIDERMAN does not compute primary transit lightcurves, so to model the observed transit (which occurs at an orbital phase of 0), support from BATMAN (Kreidberg 2015) was needed. The combined power of BATMAN and SPIDERMAN was enough to subsume the entire planet into a model which included a phase curve, secondary eclipse, and primary transit. The free parameters in the transit model were the planet-to-star radius ratio, $R_{\mathrm{p}}/R_{\mathrm{s}}$ and the mid-transit time, $t_{0,1}$. We fixed the orbital parameters a/R_{s}, i, e, ω and the period using the values published in (Hellier et al. 2011) - these are shown in Table 3.1. To model the stellar limb darkening we fitted a four-parameter non-linear limb darkening law (Claret 2000) to the ATLAS stellar model (Castelli & Kurucz 2004) that best matches WASP-19 ($T_{\mathrm{eff}} = 5\,500$ K, $\log g = 4.5$ cgs).

WASP-19b has a low measured eccentricity (0.0046±0.004, Hellier et al. 2011), so we allow the mid-time of our secondary eclipse measurement, $t_{0,2}$, to be a free parameter in our fit to see how the retrieved mid-eclipse time affects the other physical parameters in the model. Combined with the three physical parameters of the phase curve model, this means there are 21 free parameters in our white light curve fit: F_1, F_2, F_3, $t_{0,1}$, $t_{0,2}$, $R_{\mathrm{p}}/R_{\mathrm{s}}$, T_{n}, ΔT, ξ, plus four systematics parameters for each of the three visits (s_{pop}, f_{pop}, δs and δf).

We used the Markov chain Monte Carlo (MCMC) package emcee (Foreman-Mackey et al. 2013) to marginalise over the parameter space of the model likelihood distribution. We used 100 walkers and ran chains for 10 000 steps, discarding the first 1 000 as burn-in before combining the walker chains into a single chain. The best-fit model is shown in Figures 3.4 and 3.5, with the physical parameter values and 1 σ uncertainties reported in Table 3.1. Figure 3.6 shows the posterior distribution for the MCMC fit.

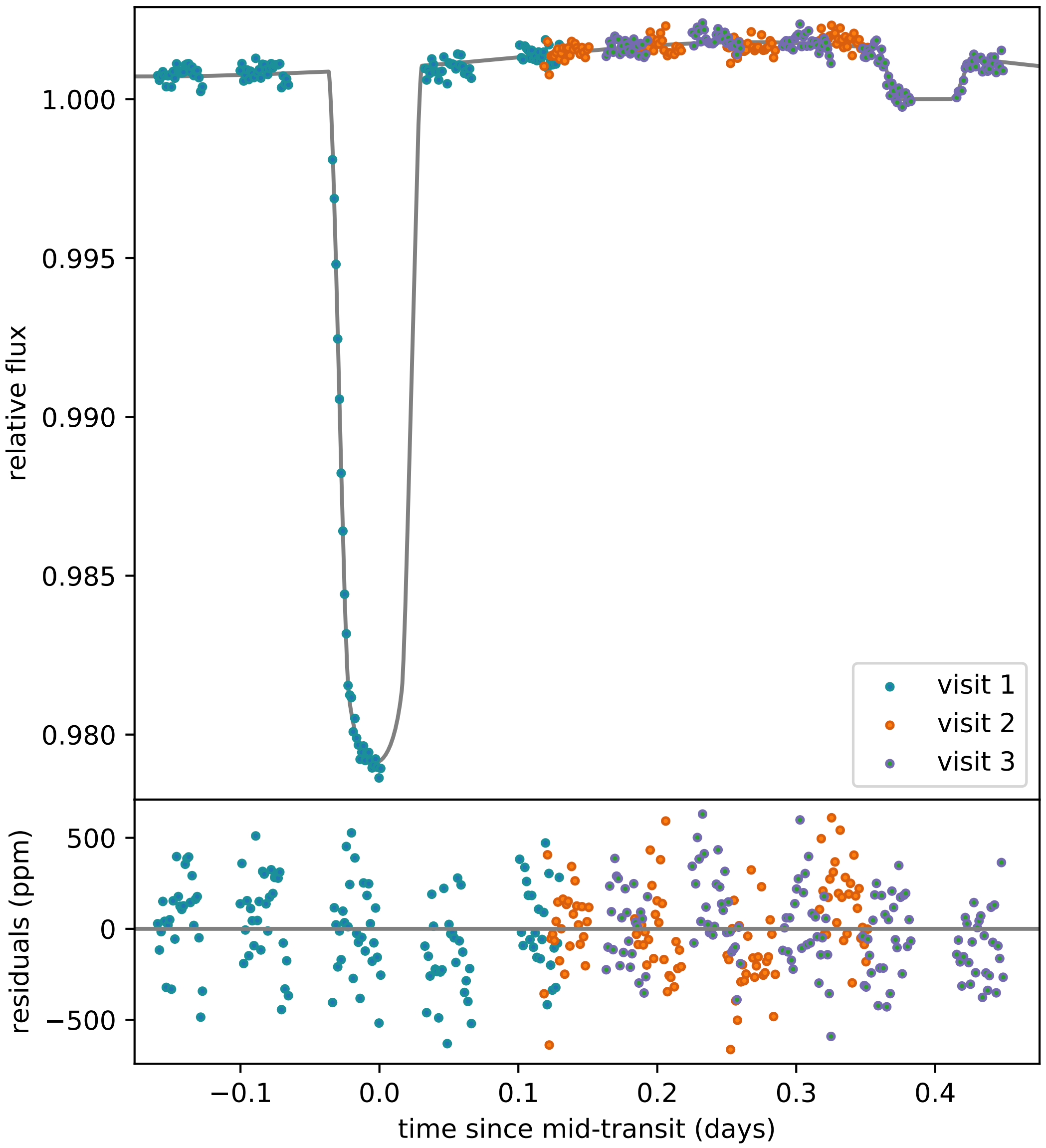

Figure 3.4: Full white light curve phase curve fit using SPIDERMAN and BATMAN. The different colour points represent data from three different visits, and the gray line is the best-fit model.

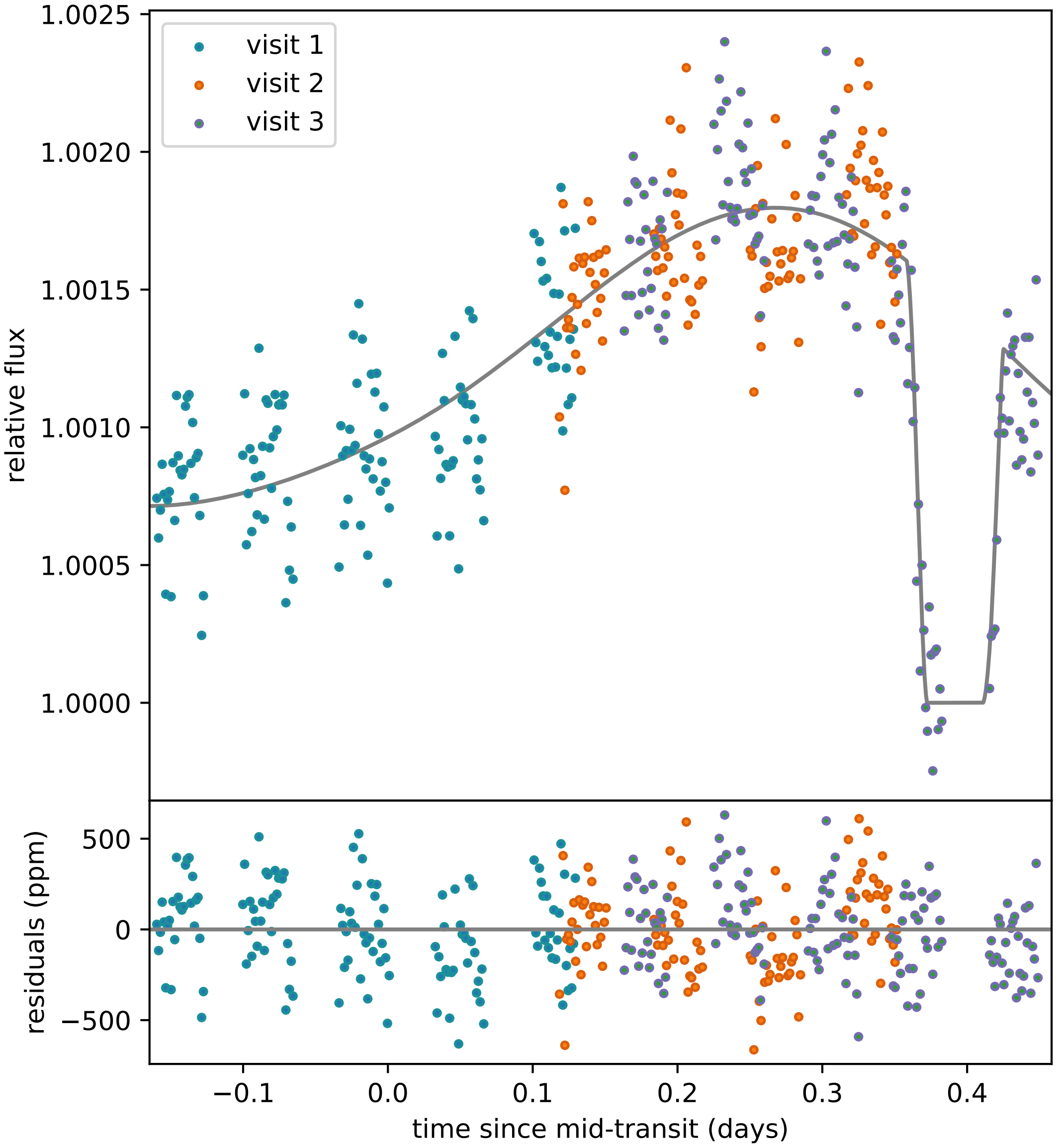

Figure 3.5: Zoomed-in version of the phase curve fit in Figure 3.4. The different colour points represent data from three different visits, and the grey line is the best-fit model.

3.5 Results and Discussion

The fitted timing offsets from the expected mid-transit and mid-eclipse times were -0.0039±0.0008 and -0.0032±0.0008 days respectively. Since they are both consistent within their error bars we were unable to place better constraints on WASP-19b's orbital eccentricity than that reported by Hellier et al. (2011). We note that their measured eccentricity for WASP-19b is small (0.0046±0.0044).

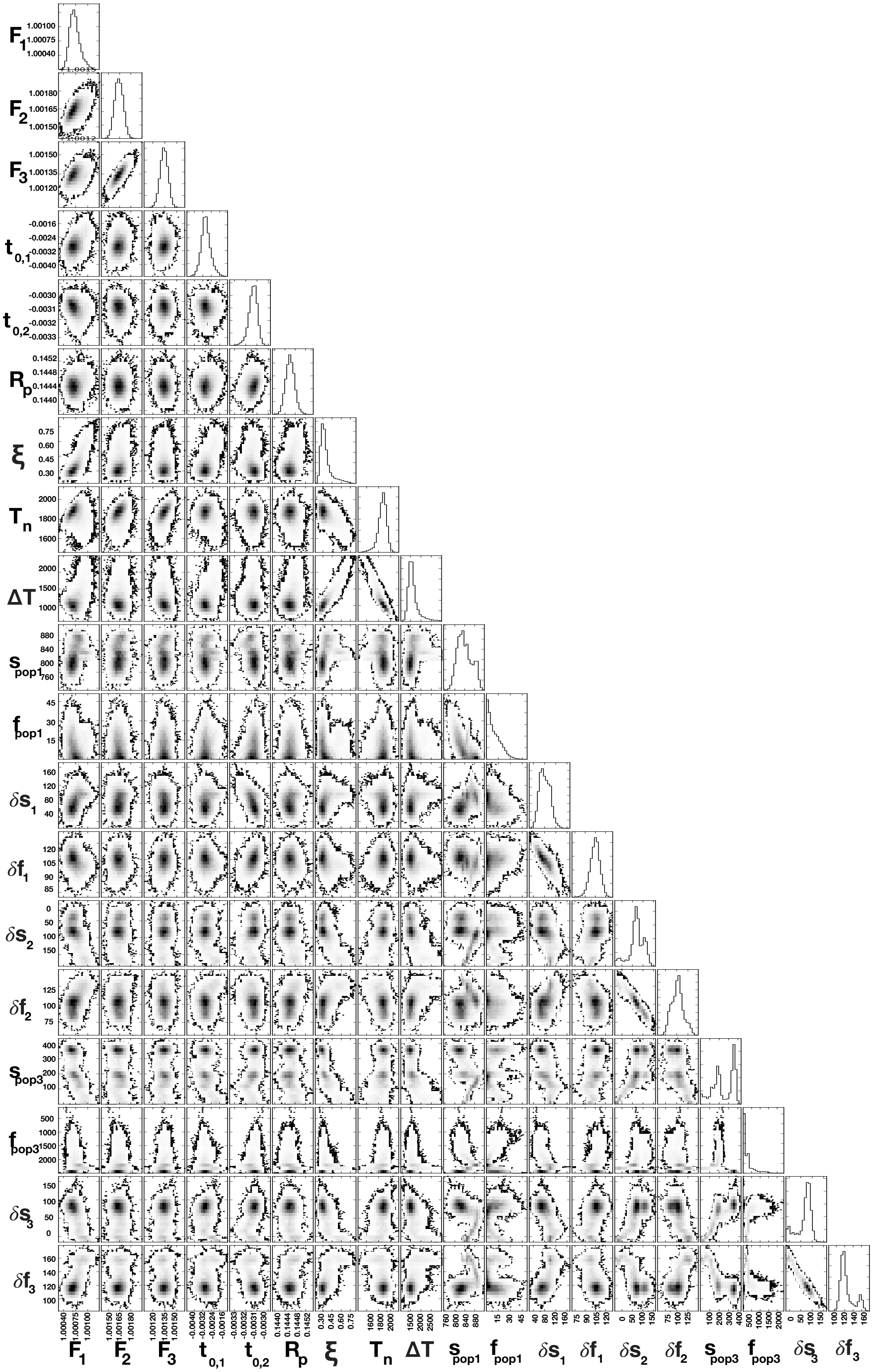

Figure 3.6: Posterior distributions for MCMC fit of WASP-19b's white light curve.

Parameter	Symbol	Result
Orbital period	P (days)	0.7884^a
Distance/stellar radius	a/R_s	3.60^a
Orbital inclination	$i(^\circ)$	79.4^a
Orbital eccentricity	e	0.0046^a
Argument of Periastron	$\omega(^\circ)$	3^a
Night-side temperature	T_n (K)	$1\,850^{+180}_{-200}$
Day-night temp. contrast	ΔT (K)	$1\,490^{+500}_{-300}$
Rad/Adv timescale ratio	ξ	$1.32^{+0.21}_{-0.06}$
Planet-to-star radius	$R_\mathrm{p}/R_\mathrm{s}$	0.1442 ± 0.0003
Mid-transit time	$t_{0,1}$ (days)	-0.0039 ± 0.0008
Mid-eclipse time	$t_{0,2}$ (days)	-0.0032 ± 0.0008

Table 3.1: Summary of phase curve fit for WASP-19b. ^{a}values fixed from Hellier et al. (2011)

Figure 3.5 shows a large offset in the peak of the phase curve relative to the sub-stellar point (the middle of the secondary eclipse). We measured the position of the hotspot offset to be 56^{+21}_{-16} degrees eastwards in longitude, by finding where the peak of the best-fitting phase curve model occurred, with 1 σ uncertainties estimated by finding the range of offsets between which 68% of the MCMC samples were contained. The result is consistent with the results of GCM calculations performed by Kataria et al. (2016) for WASP-19b at a pressure of 1 bar, shown in Figure 3.7, which have an offset of 65°. This suggests that our observations probe a region of the atmosphere that is dominated by convection, and has a strong, eastward equatorial jet.

Additionally, we measured A_F, the relative phase curve amplitude, to be $0.60^{+0.06}_{-0.08}$. This measure of the day-to-night brightness temperature contrast is defined as the difference between the maximum and the minimum of the phase curve, relative to the base of the secondary eclipse (described in Section 1.3.2). Again, our 1 σ uncertainties were the range of values which contained 68% of the MCMC samples. A_F should range from 0 to 1, where 0 would mean perfect re-distribution of heat around the planet (an unlikely scenario for tidally locked hot Jupiters), and A_F=1 would mean no heat re-distribution, so our relatively low amplitude of $0.60^{+0.06}_{-0.08}$ suggests that heat has been efficiently recirculated around the planet, which is consistent with WASP-19b's large hotspot offset and likely strong equatorial jet.

Table 3.2: Summary of WFC3 phase curve observations

Planet	T_{eq} (K)	Offset (°)	A_F	Reference.
WASP-43b	1440	12.3±1.0	1.005±0.013	Stevenson et al. (2014)
WASP-19b	2050	57^{+21}_{-16}	$0.60^{+0.06}_{0.08}$	This work
WASP-18b	2400	4.5±0.5	> 0.93	Kreidberg et al. (2018a)
WASP-103b	2500	-0.3±0.1	0.91±0.01	(Kreidberg et al. 2018a)

The best-fitting analytical atmosphere model gives a temperature difference between the dayside and the night side of $\Delta T = 1\,490^{+500}_{-300}$ K, and a night-side temperature of $1\,850^{+180}_{-200}$K, which suggests a dayside temperature of $3\,340^{+680}_{-500}$K. The day side temperature is higher than predicted by the general circulation models (GCMs) of Kataria et al. (2016) at pressures of 1 bar (see Figure 3.7), and is also higher than the day side temperature measured by Anderson et al. (2010) of 2 540±180K. On the other hand, we note that the measurement of Anderson et al. (2010) was taken from a secondary eclipse observation in the H band, which has a slightly redder wavelength range than our WFC3 observations (13 000 - 19 000Å vs 11 000 - 17 000Å , respectively). Therefore our observations may be probing hotter, deeper layers of WASP-107b's atmosphere.

The uncertainties on the day side temperature are large, at 500K or greater. Our observations only cover a small fraction of the baseline of the secondary eclipse (which measures the day side emission of the planet), which could be the reason for the large errors. There is also relatively little baseline after the secondary eclipse - less than one HST orbit - and so our measurement is highly dependent on an accurate de-trending of this orbit. These factors may be contributing to our higher-than-expected day side temperature.

Three exoplanet phase curves measured with WFC3 have previously been published; WASP-43b (Stevenson et al. 2014); WASP-103b (Kreidberg et al. 2018a); and WASP-18b (Arcangeli et al. 2019). They all show significantly smaller hotspot offsets than WASP-19b, and these are summarised in Table 3.3. As discussed in 1.3.2, there is no clear evidence for simple trends in equilibrium temperature with observable quantities (like hotspot offsets), which depend on many interrelated physcal processes (like 3D hydrodynamics, rotation rates, surface gravity, and clouds), especially with so few observations. Nonetheless we provide the measurements to give some context to our observations of WASP-19b. With an equilibrium temperature of 1 440K, WASP-43b belongs to a cooler class of exoplanets than WASP-19b. Two different works which ran GCM models for WASP-43b using different treatments of clouds, metallicity, turbulence and computational grids suggest eastwards hotspot offsets of 10 - 45° (Kataria et al. 2015; Mendonça et al. 2018) at pressures corresponding to the WFC3 bandpass (∼1 bar), which are broadly consistent with the observations of Stevenson et al. (2014). Therefore, models and observations of both planets suggest that WASP-43 has a more moderate equatorial jet compared to WASP-19, although questions remain about WASP-43b's atmospheric metalicity and clouds.

Both WASP-103b and WASP-18b have higher equilibrium temperatures than WASP-19b, by several hundred degrees. It has been suggested that the two hot planets belong to a class of 'Ultra Hot Jupiters' (UHJs) which, with equilibrium temperatures greater than around 2 500K, have fundamentally different atmospheric chemistry than cooler exoplanets. The temperatures are expected to be high enough for significant thermal dissociation of molecules and ionisation of atoms (Mendonça et al. 2018). Bell et al. (2017) and Arcangeli et al. (2019) see evidence of Rayleigh scattering from atomic hydrogen in their emission spectra of the UHJs WASP-12b and WASP-103b, which would suggest that significant dissociation of molecular hydrogen is indeed happening on those planets. If the ionisation fractions in the atmospheres of the UHJs are high enough, and the planets have moderate magnetic fields (∼10 G), then magnetic braking of waves in the dayside atmosphere could impede the formation of an equatorial jet and lead to smaller hotspot offsets than those predicted without considering magnetic effects (Perna et al. 2010). Perhaps this partly explains why WASP-18b and WASP-103b have smaller hotspot offsets than the cooler WASP-19b? However, the answer is likely to be complicated. Bell & Cowan (2018) modeled the effects of H_2 dissociation on the dayside of UHJs, and its subsequent recombination on the night-side, and showed that hydrogen can act as a latent heat source and efficiently re-distribute heat around the planet, leading to

Table 3.3: Summary of WFC3 phase curve observations

Planet	T_{eq} (K)	Offset (°)	A_F	Reference.
WASP-43b	1440	12.3±1.0	1.005±0.013	Stevenson et al. (2014)
WASP-19b	2050	57^{+21}_{-16}	$0.60^{+0.06}_{-0.08}$	This work
WASP-18b	2400	4.5±0.5	> 0.93	Kreidberg et al. (2018a)
WASP-103b	2500	-0.3±0.1	0.91±0.01	(Kreidberg et al. 2018a)

lower day-night contrasts and larger hotspot offsets. No models which include both the H_2 dissociation-transport-recombination process and magnetic braking have yet been published.

Maybe the reason WASP-19b has a significantly larger offset than planets both cooler and hotter than itself, in the same bandpass, is because it is hot enough to drive strong winds around its equator, but not hot enough for significant ionisation and magnetic breaking. Or perhaps we are actually probing different atmospheric pressures in the different planets - maybe because WASP-19b is in fact partly cloudy. In any case, WASP-19b's large hotspot offset and relatively low phase curve amplitude paint a consistent picture of an atmosphere dominated by strong, planet-wide winds which efficiently re-distribute heat around the planet at the pressures probed by WFC3. At present, WASP-19b is the only exoplanet to show such an extreme hotspot offset in its phase curve.

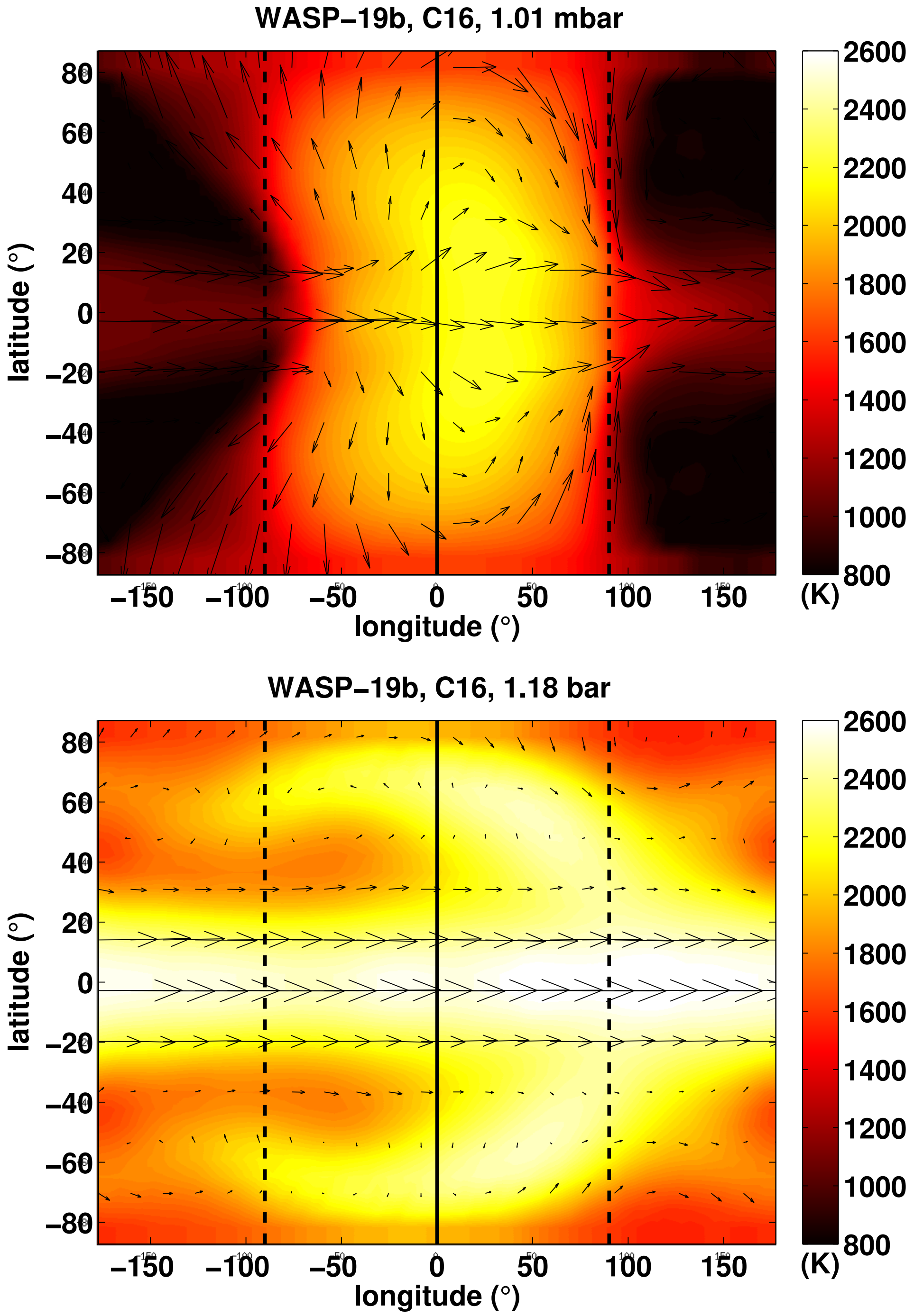

Figure 3.7: Two slices of a GCM output from the models described in Kataria et al. (2016), showing temperature maps of WASP-19b, at pressures of 1.01 mbar and 1.18 bar respectively. The lower-pressure model shows an eastward hostspot offset of around 10°, which is consistent with Spitzer phase curve measurements from Wong et al. (2016). The deeper model has a strong equatorial jet giving a large offset of around 60°. This is consistent with our WFC3 phasecurve, although our inferred brightness temperatures appear inconsistent with the model. Figure from T. Kataria (private communication, 2018).

Chapter 4

The puffy: sodium, potassium, water, and carbon-bearing species in WASP-127b

4.1 Statement of contribution

For the work covered in this Chapter, J. J. Spake led the HST telescope time proposal (GO-14619), designed the observations, led the data analysis, and performed a preliminary retrieval analysis. N. Nikolov provided reduced STIS spectra, T. Evans provided reduced Spitzer photometry, and a reduction code for WFC3 that was adapted by J. J. Spake.

4.2 Introduction

WASP-127b is a sub-Saturn mass exoplanet from the SuperWASP survey (Lam et al. 2017). It has the largest expected atmospheric scale height of any planet yet discovered, at ∼2 350km. This, combined with the favorable brightness of its host star (V∼10.2, J∼9.1), means WASP-127b is a standout target for atmospheric characterization. With HST and Spitzer, it is possible to measure a transmission spectrum rivaling the quality of even the canonical planets HD 209458b and HD 189733b. Importantly, with a mass of only 0.19M_J, WASP-127b is the most accessible planet in a sparsely populated regime at the low-mass end of gas-giant exoplanets (see Figure 4.1). Evidence of sodium, lithium, potassium and haze has been reported by Palle et al. (2017) and Chen et al. (2018) using the ground-based NOT and GTC telescopes, respectively. They also report an intriguingly sharp rise in WASP-127b's transmission spectrum shortwards of 0.4μm, which they attribute to a mystery UV absorber. Until now, there have been no observations of WASP-127b's near-infrared transmission spectrum.

We carried out a joint HST and Spitzer programme to observe the full optical to infrared transmission spectrum of WASP-127b. The combined wavelength coverage of the programme from 0.3 to 5μm includes strong molecular absorption features from water and carbon-bearing species in the infrared, along with sodium and potassium absorption features, and Rayleigh scattering caused by high-altitude aerosols and H_2 in the optical region. Using HST transmission spectra and Spitzer/IRAC transit photometry, Sing et al. (2016) devised an effective metric for distinguishing between different atmosphere types, and classifying a planet as clear or cloudy. We aimed, with this study, to apply the same methodology to classify WASP- 127b as cloudy or cloud-free, and measure the abundances of important gaseous species such as H_2O, Na and K.

In the future, WASP-127b will likely become a focus of intensive JWST observations. The characterization described here will allow the community to optimize scientific objectives, instrument setup, and phase coverage for these future JWST observations.

4.3 Observations and data reduction

All observations were made as part of a joint HST/Spitzer programme GO:14619 (PI: Spake). We observed five transits of WASP-127b using different instrument

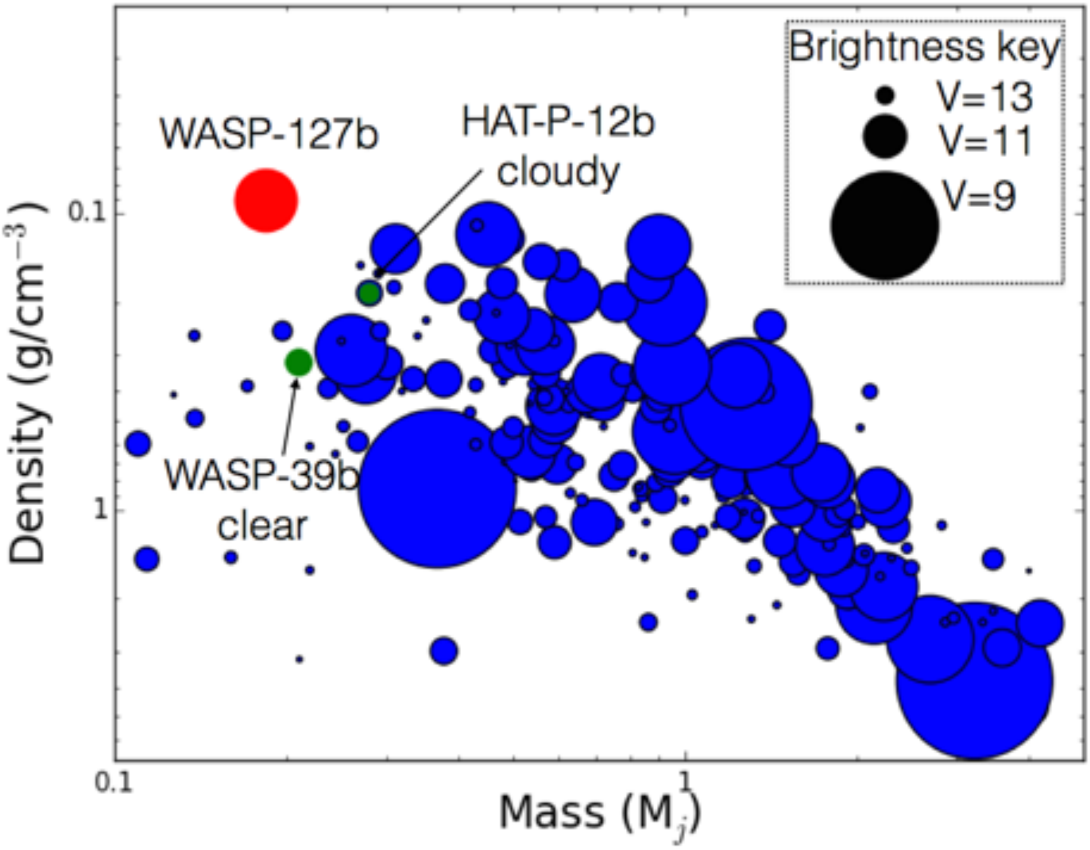

Figure 4.1: Mass as a function of density for known transiting exoplanets with masses greater than 0.1 M_J (from exoplanets.eu), and densities less than 7g/cm^3. WASP-127b is the lowest density giant planet known to science.

setups with HST and Spitzer, in order to build a transmission spectrum covering the 0.3 - 5 μm wavelength range. A summary of the observations is given in Table 4.1.

4.3.1 STIS

We observed two transits with HST/STIS, one each with the G430L and G750L grisms. We followed an observing strategy proven to produce high signal-to-noise spectra (e.g. Brown et al. 2001, Sing et al. 2011, Huitson et al. 2012, Nikolov et al. 2015). The data were taken on 2018-06-23 and 2018-02-18, covering wavelengths of 2 900−5 700 and 5 240−10 270Å, respectively. Visits 1 and 2 both lasted 4.5 spacecraft orbits each. One HST orbit lasts $\sim$ 96 minutes during which WASP-127b is visible for $\sim$ 45 minutes, leaving $\sim$ 45 minute gaps in the data as the spacecraft passes through the Earth's shadow. WASP-127b has a long transit duration ($\sim$3.5 hours, compared to $\sim$2 hours for a typical hot Jupiter, e.g. HD 209458b). We scheduled each visit such that 2 orbits fell fully inside a transit and 1.5 fell either side of it, in order to accurately measure the baseline stellar flux. We used integration times of 280 and 180 seconds, resulting in a total of 48 and 58 low-resolution spectra ($\Delta\lambda/\lambda = 500$) for the G430L and G750L visits respectively. We used 52" x 2" slits to minimise slit losses, and minimised the data-acquisition overheads by reading out a smaller portion of the CCD (128 x 128 pixels).

Our data reduction method for STIS follows previous works such as Sing et al. (2013), Huitson et al. (2013), and Nikolov et al. (2014, 2015). We used the most recent version of the CALSTIS automatic reduction pipeline (Katsanis & McGrath 1998) included in IRAF[1] (Tody 1993) to reduce the raw STIS data (which involves bias-, dark-, and flat-correction). Similarly to Nikolov et al. (2015), we corrected the G750L spectra for fringing effects with the method described in Goudfrooij & Christensen (1998). Further, we used the method described in Nikolov et al.

---

[1] IRAF is distributed by the National Optical Astronomy Observatories, which are operated by the Association of Universities for Research in Astronomy, Inc., under cooperative agreement with the National Science Foundation.

(2013) to correct the data for cosmic rays and bad pixels flagged by the CALSTIS pipeline. We then extracted 1D spectra from the reduced data frames using IRAF's APALL. We used aperture widths ranging from 3.5 to 10.5 pixels, in 1-pixel steps, and found the aperture width for each visit that gave the lowest residual scatter in the white light curve (see Section 4.4.1). The selected aperture widths were 9.5 and 10.5 for G430L and G750L, respectively. Finally, the wavelength solutions for each spectrum were obtained from the *x*1*d* files from CALSTIS, and the spectra were then cross-correlated with the median of the out-of-transit spectra to place them on a common wavelength scale, which helps to account for sub-pixel shifts in the dispersal direction.

WFC3

We observed one spectroscopic transit of WASP-127b using HST/WFC3 with the G141 grism. The observations spanned the approximate wavelength range of 11 000 – 17 000Å , which covered a broad band of water absorption lines centred on 14 000Å . We used HST's spatial scan mode and a scan rate of 1 pixel per second for 15 observations of 120 seconds each, which spread WASP-127's spectrum over 120 pixels. The maximum number of electron counts per pixel was 29 000 - which is about 40% of the saturation limit of the detector. The raw frames were first reduced with the automatic CalWF3 pipeline. The 1-D spectra were then extracted following standard methods (e.g Evans et al. 2017): building up flux counts by summing the difference between successive non-destructive reads. We removed the background from each read difference by subtracting the median of a box of pixels uncontaminated by the spectrum. We found the flux-weighted centre of each scan and set to zero all pixels more than 80 rows away from the centre in the cross-dispersion axis, which removes many cosmic rays. The remaining cosmic rays were flagged by finding 4σ outliers relative to the median along the dispersion direction. We replaced each flagged pixel with the median along the dispersion direction, re-scaled to the count rate of the cross-dispersion column. We used the IRAF package Apall to fit the trace of the 2-D scans and extract 1-D spectra. We found the wavelength solutions by cross-correlating the extracted spectra with an ATLAS model stellar spectrum (Castelli & Kurucz 2004) which most closely matches WASP-127 ($T_{\mathrm{eff}} =$ 5 500 K, log g = 4.0 cgs); modulated by the G141 grism throughput. Following standard methods (Kreidberg et al. 2018b) we interpolated each spectrum onto the wavelength range of the first to account for shifts in the dispersion axis over time.

4.3.2 Spitzer/IRAC photometry

We observed WASP-127b during two primary transits using the sub-array mode with Spitzer/IRAC channels 1 and 2, using 2 second integration times, for 9 hours each visit, with the duration set to include the 3.5 hour transit and a baseline equally as long to precisely measure the transit depth (plus some extra time as insurance). WASP-127's expected flux is 75 mJy/52 mJy for 3.6/4.5 μm, and our 2-second exposure time was short enough to stay well below saturation. The sub-array mode allowed for high cadence observations which aids in removing the detector intra-pixel sensitivity, and reduces data storage overheads. Each visit could only be done at a single wavelength requiring two transits to observe at 3.6 and 4.5 μm, as cycling between the two channels greatly exacerbates the intra-pixel sensitivity noise. Each observation began with a recommended Pointing Calibration and Reference Sensor peak-up mode of 30 minutes, which locates the star into the sub-array pixel "sweet spot" and helps mitigate the intra- pixel sensitivity effects providing <100 parts per million accuracies.

For both Spitzer channels, we followed the data reduction and photometry procedures of Evans et al. (2015). We reduced the Basic Calibrated Data (BCD) frames for each light curve using a publicly-available PYTHON pipeline[2], which does the following: first, it calculates the background level and locates the stellar centroid in each BCD frame. It estimates the background from the median pixel value of four 8 × 8 pixel subarrays at the corners of each frame, and then subtracts that value from each pixel in the array. It finds the centroid coordinates by taking the

---

[2] from www.github.com/tomevans

Table 4.1: Summary of transit observations of WASP-127b.

Instrument	Start date (UTC)	Wavelength range (Å)	Duration (hours)
HST/STIS+G430L	2018-06-23	2 900−5 700	6.8
HST/STIS+G750L	2018-02-18	5 240−10 270	6.8
HST/WFC3+G141	2018-04-09	11 000−17 000	6.8
Spitzer/IRAC Ch1	2017-04-02	3 550	9
Spitzer/IRAC Ch2	2017-04-06	4 490	9

flux-weighted mean of a 7 × 7 pixel subarray centred on the star. The pipeline computes exposure mid-times in Barycentric Julian Date Coordinated Universal Time (BJDUTC) using the $BMJD_OBS$ and $FRAMTIME$ header entries. It flags bad frames by identifying frames whose centroid coordinates or pixel counts deviate by 5σ from those of the 30 frames immediately preceding and following each frame. We removed bad frames from the analysis. We iterated this bad-frame identification twice, and discarded less than 5 % of the frames.

The pipeline performed photometry on each remaining frame by summing the pixel counts within circular apertures of various sizes between 1.5 and 6 pixels, in increments of 0.5 pixels. Because the IRAC point spread function (PSF) is undersampled, we linearly interpolated the pixel array on to a 10 × 10 supersampled grid, which has previously been done by Stevenson et al. (2010), for example. We counted the interpolated subpixels towards the aperture sum if their centres fell within the aperture radius. Our selected photometric light curves are shown in Figures 4.14 and 4.16, and we discuss how the apertures were chosen in Section 4.4.2.

4.4 Light curve fitting

4.4.1 HST: STIS and WFC3

We followed the same light-curve fitting procedure for all three of the STIS and WFC3 visits, but here describe the process for one visit.

White light curve fit

We first created the white light curve by summing the counts of each 1D spectrum, across all wavelengths. The resulting time-series flux measurements show the transit signal modulated by systematic trends which correlate with HST phase, and the changing position of the spectrum on the detector. Such trends are commonly reported in STIS time-series data (e.g. Brown et al. 2001, Huitson et al. 2013, Nikolov et al. 2014). Since we do not know the functional form of the systematic trends for STIS, Gibson et al. (2012) suggest treating the lightcurve as a Gaussian Process (GP). Therefore, we follow the implementation of GPs for the STIS lightcurves pioneered by Evans et al. (2013, 2018), except we use the Python library for GP regression, George (Ambikasaran et al. 2014) rather than the custom code used by Evans et al. We also use the same method to analyse the WFC3 data, with the aim of improving upon the precision reached for the WASP-107b data (see Chapter 2). Similarly to Evans et al. (2013, 2018), we used a squared- exponential kernel for the GP covariance matrix. We used three GP input variables - the HST orbital phase (ϕ), the position of the spectrum in the spatial direction on the detector (x), and the position in the dispersion direction (y). This gave four free GP parameters: the covariance amplitude (A), and a correlation length scale for each of the four input variables: L_{ϕ}, L_{x}, and L_{y} for HST phase, x, and y respectively. We used the BATMAN Python package (Kreidberg 2015) to model the transit light curve signal, and fit for the planet-to-star radius ratio (R_{p}/R_{*}) and mid-transit time (t_0), fixing the remaining orbital parameters to the values given in Table 4.3. To model the stellar limb darkening we fitted a four-parameter non-linear limb darkening law (Claret 2000) to the ATLAS stellar model (Castelli & Kurucz 2004) which most closely matches WASP-127 ($T_{\mathrm{eff}} = 5\,500$ K, log $g = 4.0$ cgs). We also fit for the gradient (c_1) and y-intercept (c_0) of a linear trend in the out-of-transit baseline. Therefore, for the white light curve, we fit for 8 free parameters overall: R_{p}/R_{*}, t_0, c_1, c_0, A, L_{ϕ}, L_{x}, and L_{y}. We used the Markov chain Monte Carlo (MCMC) package emcee (Foreman-Mackey et al. 2013) to marginalise over the parameter space of the model likelihood distribution. We used 80 walkers and ran chains for 500 steps, discarding

Parameter	Value
Transit depth (%)	$1.034^{+0.006}_{-0.005}$
Mid-time (JD)	$2\,458\,293.2528^{+0.0005}_{-0.0005}$
Period (day)	4.178^{a}
a/R_*	8.044^{a}
Inclination (°)	88.7^{a}
Eccentricity	0^{a}
Arg. of Periastron	90^{a}
LD coefficients (u_{1-4})	0.5466^{b}, -0.3781^{b}, 1.2964^{b}, -0.5955^{b}

Table 4.2: Results from white light curve fit for WASP-127b using HST/STIS+G430L. ^{a} planet parameters fixed to values from (Lam et al. 2017). ^{b} Limb darkening parameters fixed from ATLAS models (Castelli & Kurucz 2004).

Parameter	Value
Transit depth (%)	$1.013^{+0.009}_{-0.006}$
Mid-time (JD)	$2\,458\,167.9226^{+0.0008}_{-0.0027}$
Period (day)	4.178^{a}
a/R_*	8.044^{a}
Inclination (°)	88.7^{a}
Eccentricity	0^{a}
Arg. of Periastron	90^{a}
LD coefficients (u_{1-4})	0.7017^{b}, -0.5462^{b}, 1.1008^{b}, -0.5233^{b}

Table 4.3: Results from white light curve fit for WASP-127b using HST/STIS+G750L. ^{a} planet parameters fixed to values from (Lam et al. 2017). ^{b} Limb darkening parameters fixed from ATLAS models (Castelli & Kurucz 2004).

the first 100 as burn-in before combining the walker chains into a single chain. The best-fit results for the transit depth $[(R_{\mathrm{p}}/R_*)^2]$ and t_0 are given in Tables 4.2, 4.3 and 4.4 for the G430L, G750L and WFC3 visits respectively. Similarly, Figures 4.2, 4.4 and 4.6 show the best-fit white light curves and their residuals for each visit. Figures 4.3, 4.5, and 4.7 show corner plots of the MCMC chains, which illustrate the posterior distributions for each of the fits. The posterior distributions appear well sampled, and there are no problematic correlations between R_{p}/R_* and the other fitted parameters.

Spectroscopic light curve fit

We used the same spectroscopic light curve procedure for each of the three visits. First, we binned each individual spectrum into spectroscopic channels (the wavelength ranges are given in Tables 4.7, 4.8 and 4.9), to make the spectroscopic light

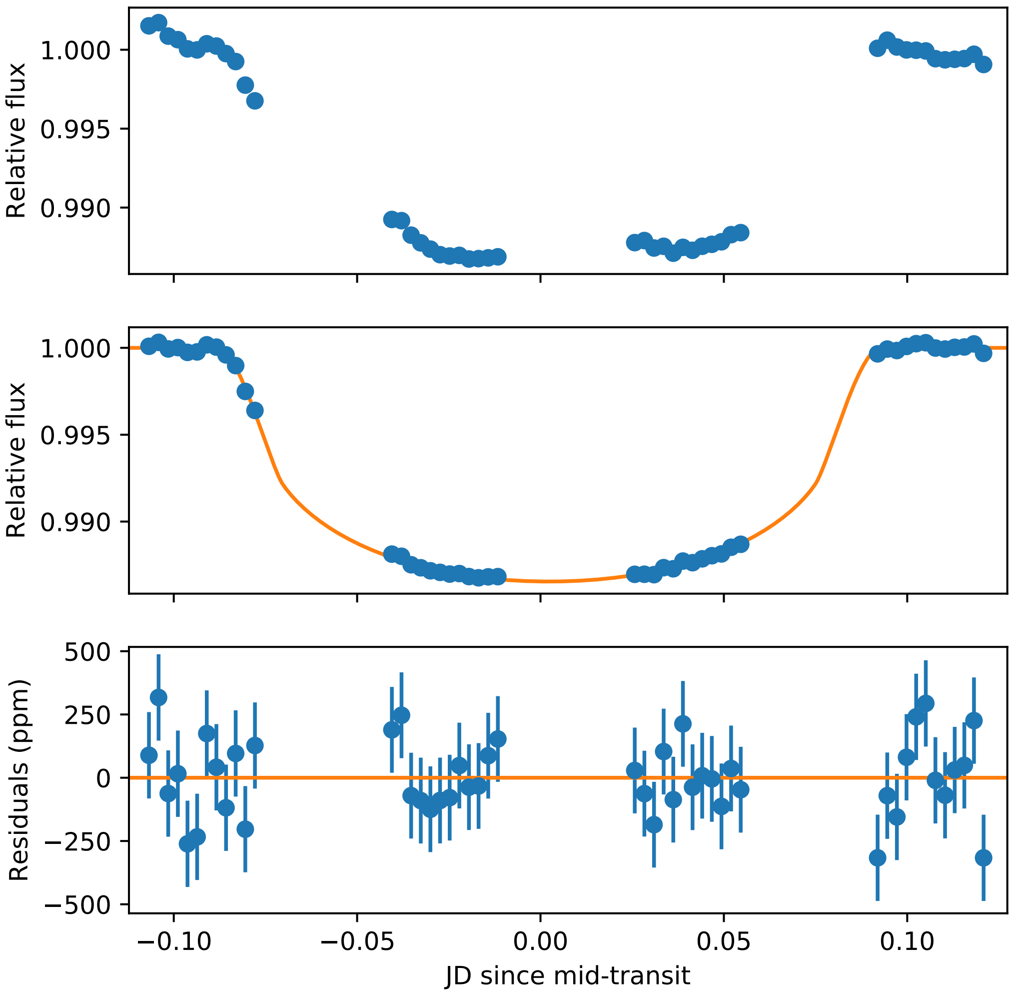

Figure 4.2: White light curve fit for WASP-127b using HST/STIS+G430L, covering the entire 2 900−5 700Å wavelength range. Top panel: raw flux before de-trending, divided by the median of the out-of-transit data. Middle panel: points are data divided by systematics model, curve is the best-fit transit model. Bottom panel: best-fit model residuals.

Parameter	Value
Transit depth (%)	$0.996^{+0.011}_{-0.011}$
Mid-time (JD)	$2\,458\,218.0484^{+0.0017}_{-0.0015}$
Period (day)	4.178^{a}
a/R_*	8.044^{a}
Inclination (°)	88.7^{a}
Eccentricity	0^{a}
Arg. of Periastron	90^{a}
LD coefficients (u_{1-4})	0.5944^{b}, 0.0707^{b}, -0.1204^{b}, 0.0202^{b}

Table 4.4: Results from white light curve fit for WASP-127b using HST/WFC3+G141. [a] planet parameters fixed to values from (Lam et al. 2017). [b] Limb darkening parameters fixed from ATLAS models (Castelli & Kurucz 2004).

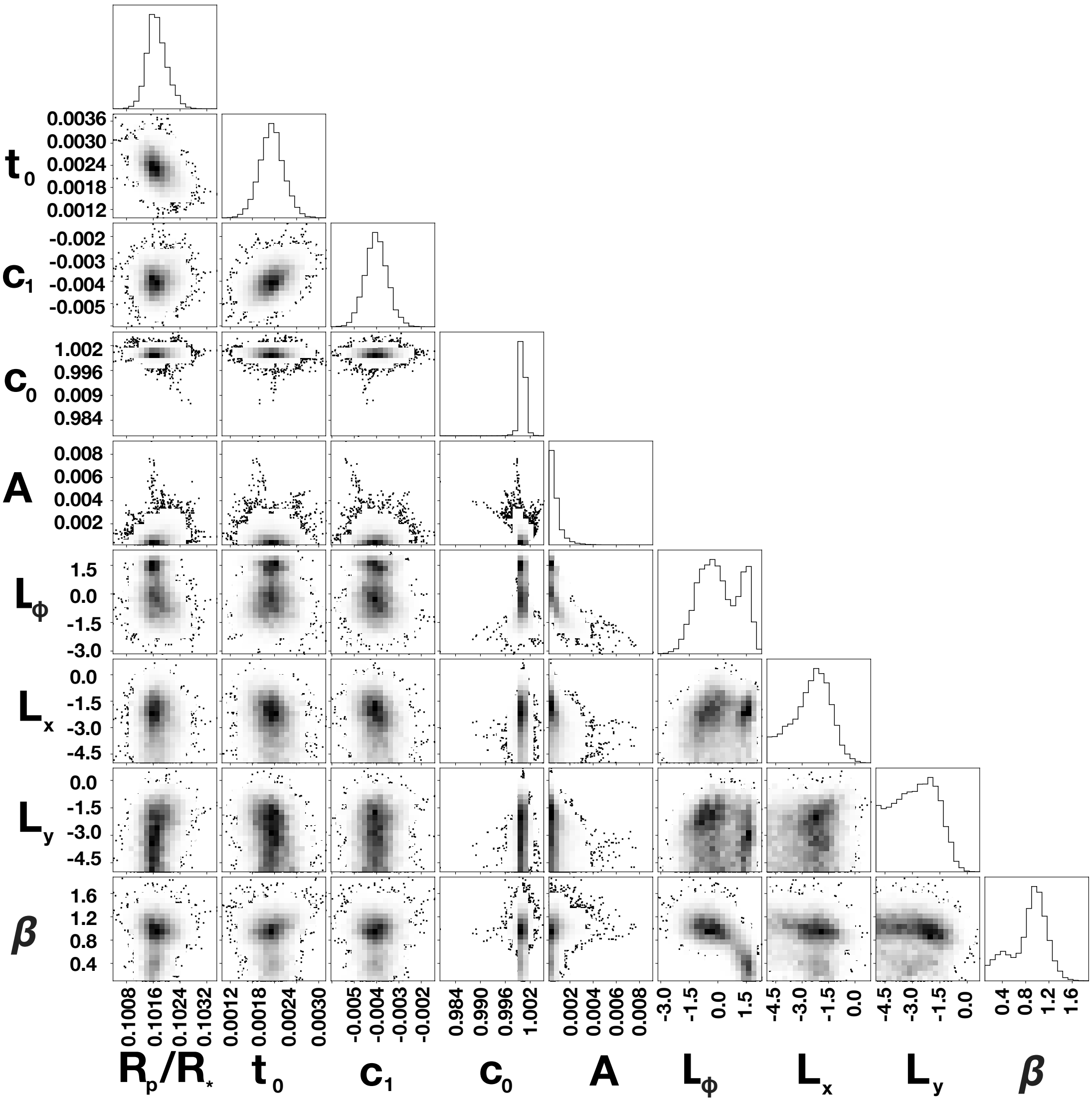

Figure 4.3: Posterior distributions for white lightcurve MCMC fit for WASP-127b, using HST/STIS+G430L.

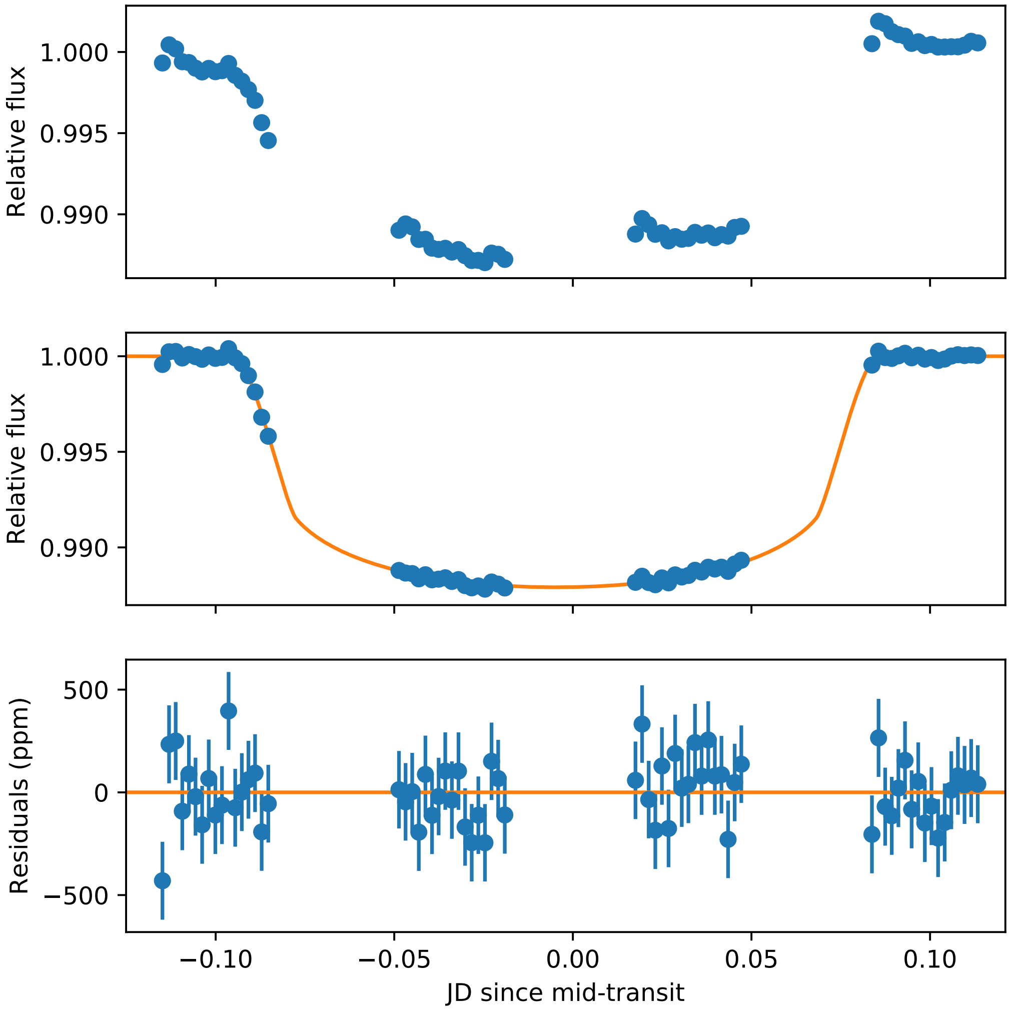

Figure 4.4: White light curve fit for WASP-127b using HST/STIS+G750L, covering the entire 5 240−10 270Å wavelength range. Top panel: raw flux before de-trending, divided by the median of the out-of-transit data. Middle panel: points are data divided by systematics model, curve is the best-fit transit model. Bottom panel: best-fit model residuals.

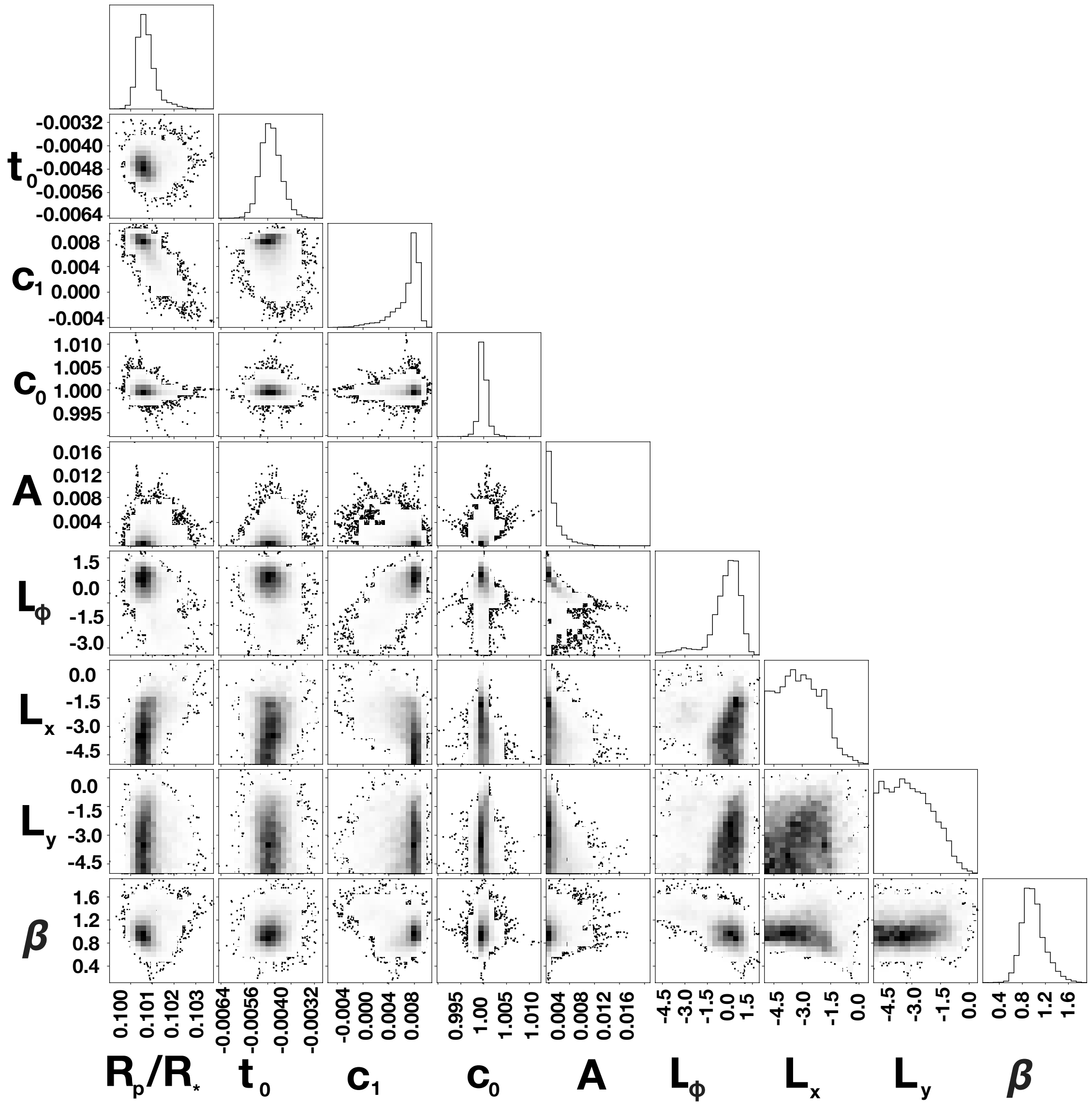

Figure 4.5: Posterior distributions for white lightcurve MCMC fit for WASP-127b, using HST/STIS+G750L.

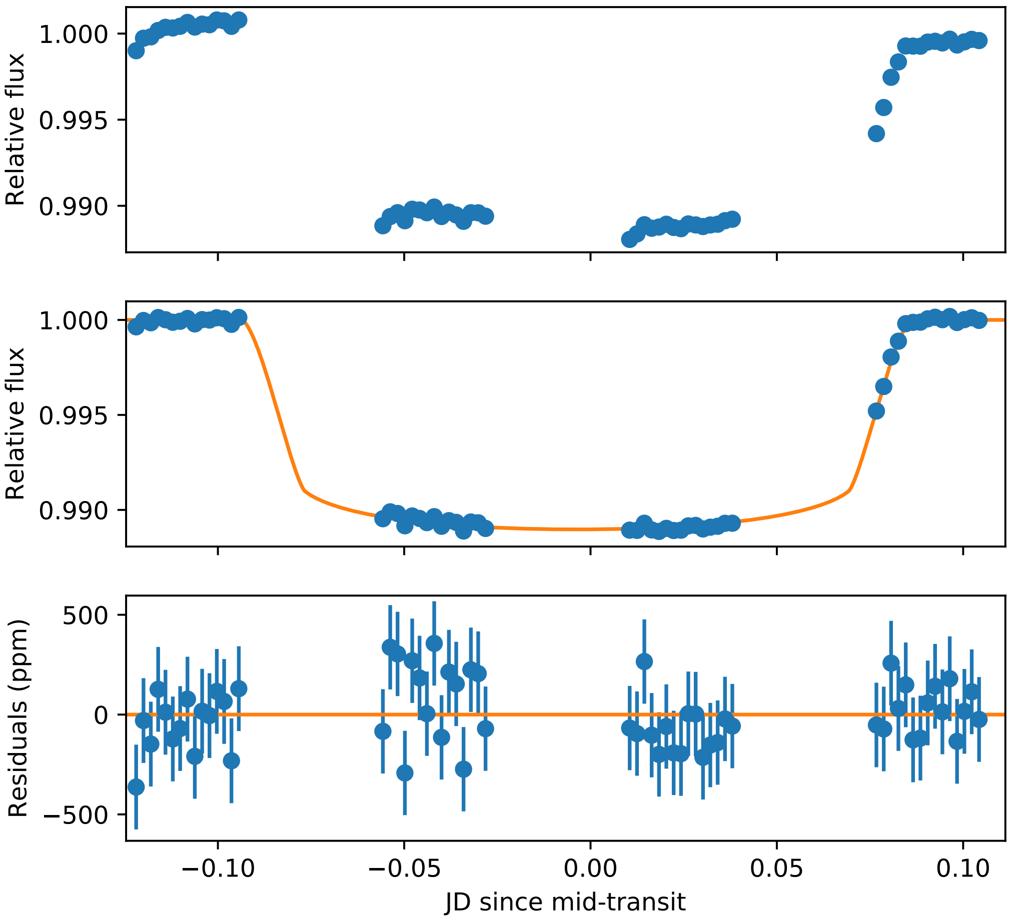

Figure 4.6: White light curve fit for WASP-127b using HST/WFC3+G141, covering the entire 11 000 - 17 000Å wavelength range. Top panel: raw flux before de-trending, divided by the median of the out-of-transit data. Middle panel: points are data divided by systematics model, curve is the best-fit transit model. Bottom panel: best-fit model residuals.

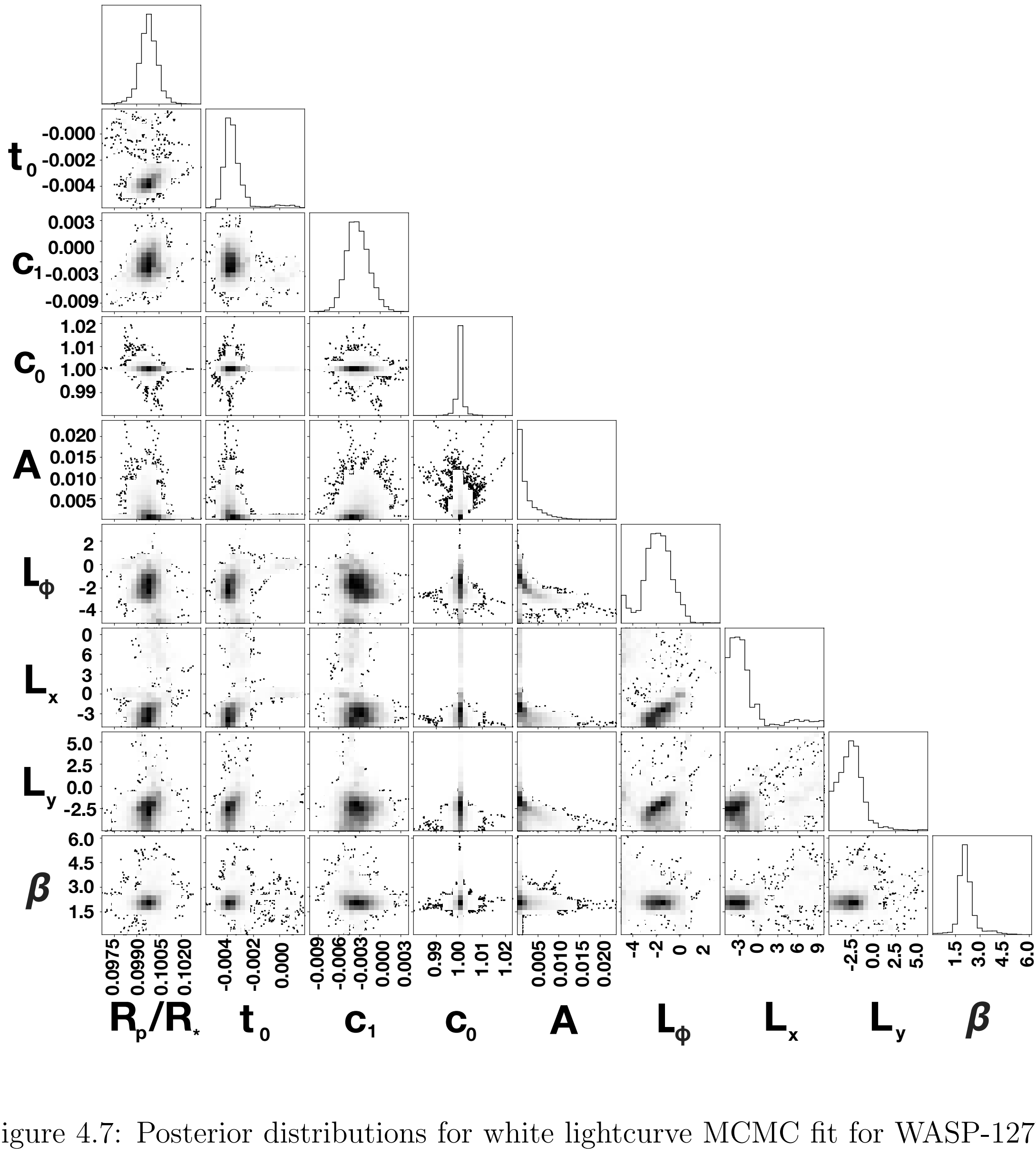

Figure 4.7: Posterior distributions for white lightcurve MCMC fit for WASP-127b, using HST/WFC3+G141.

curves. In our fits, we fixed t_0 to the value found from the white light curve fit. Similarly to the white light curve fit, we fixed the orbital parameters to those derived from Anderson et al. (2017), and wavelength-dependent limb darkening coefficients from the same ATLAS model which best describes WASP-127. Therefore, for each spectroscopic channel the fitted parameters were R_{p}/R_{*}, c_1, c_0, A, L_{ϕ}, L_{x}, and L_{y}. We used the Markov chain Monte Carlo (MCMC) package emcee (Foreman-Mackey et al. 2013) to marginalise over the parameter space of the model likelihood distribution. We used 80 walkers and ran chains for 500 steps, discarding the first 100 as burn-in before combining the walker chains into a single chain. The best-fit transit depths are given in Tables 4.7, 4.8 and 4.9 for the G430L, G750L and WFC3 visits respectively. The best fit spectroscopic lightcurves and their residuals are shown in Figures 4.8, 4.10 and 4.12. Example posterior distributions for individual spectroscopic light curves are shown in Figures 4.9, 4.11 and 4.13. The posterior distributions appear well sampled, and there are no problematic correlations between R_{p}/R_{*} and the other fitted parameters.

4.4.2 Spitzer

We used the same light curve fitting procedure for both Spitzer/IRAC channels. Spitzer photometry is prone to large intra-pixel systematics (e.g. Deming et al. 2005). To correct for this we fit for a two-dimensional quadratic trend in the photometry with the x and y position of WASP-127's centroid (measured using the pipeline discussed in Section 4.3.2). The function has the form

$$F = c_{2,\mathrm{x}} \times x^2 + c_{2,\mathrm{y}} \times y^2 + c_{1,\mathrm{x}} \times x + c_{1,\mathrm{y}} \times y + c_{\mathrm{xy}} \times xy, \tag{4.1}$$

and we fit for the following five free parameters: $c_{2,\mathrm{x}}$, $c_{1,\mathrm{x}}$, $c_{2,\mathrm{y}}$, $c_{1,\mathrm{y}}$ and $c_{\mathrm{x,y}}$. We used BATMAN to model the transit light curve, and fit for R_{p}/R_{*} and the transit mid-time, t_0. We also fit for the gradient (c_1) and linear trend (c_0) in the baseline in the photometry. In total there were 9 free parameters in the light curve fit. We used

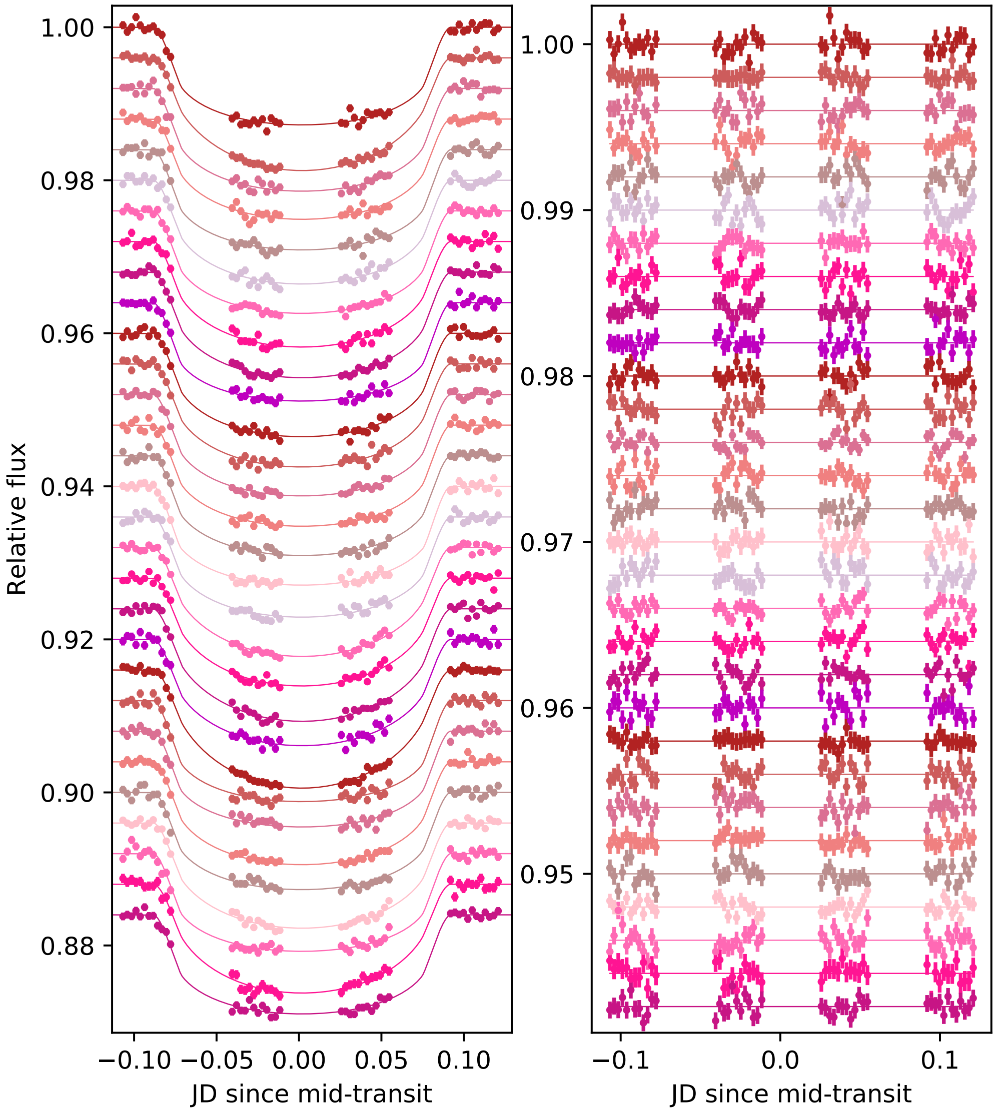

Figure 4.8: Spectroscopic light curves for WASP-127b using HST/STIS+G430L, covering the 2 900−5 700Å wavelength range. (a) Points are light curves divided by systematics models, curves are best-fit transit models. (b) Best-fit model residuals. Arbitrary vertical offsets applied for clarity.

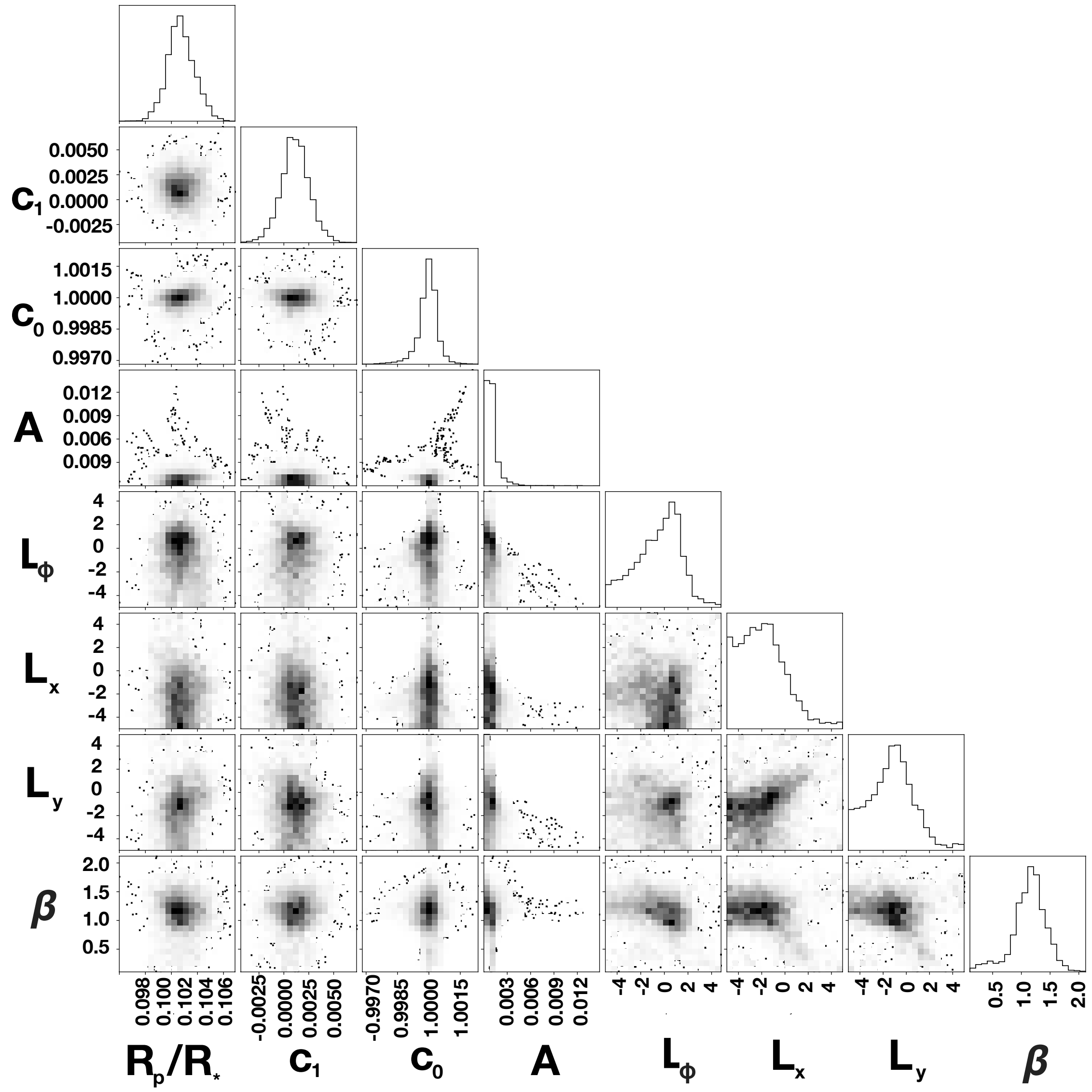

Figure 4.9: Typical posterior distributions for spectroscopic lightcurve MCMC fits for WASP-127b, using HST/STIS+G430L.

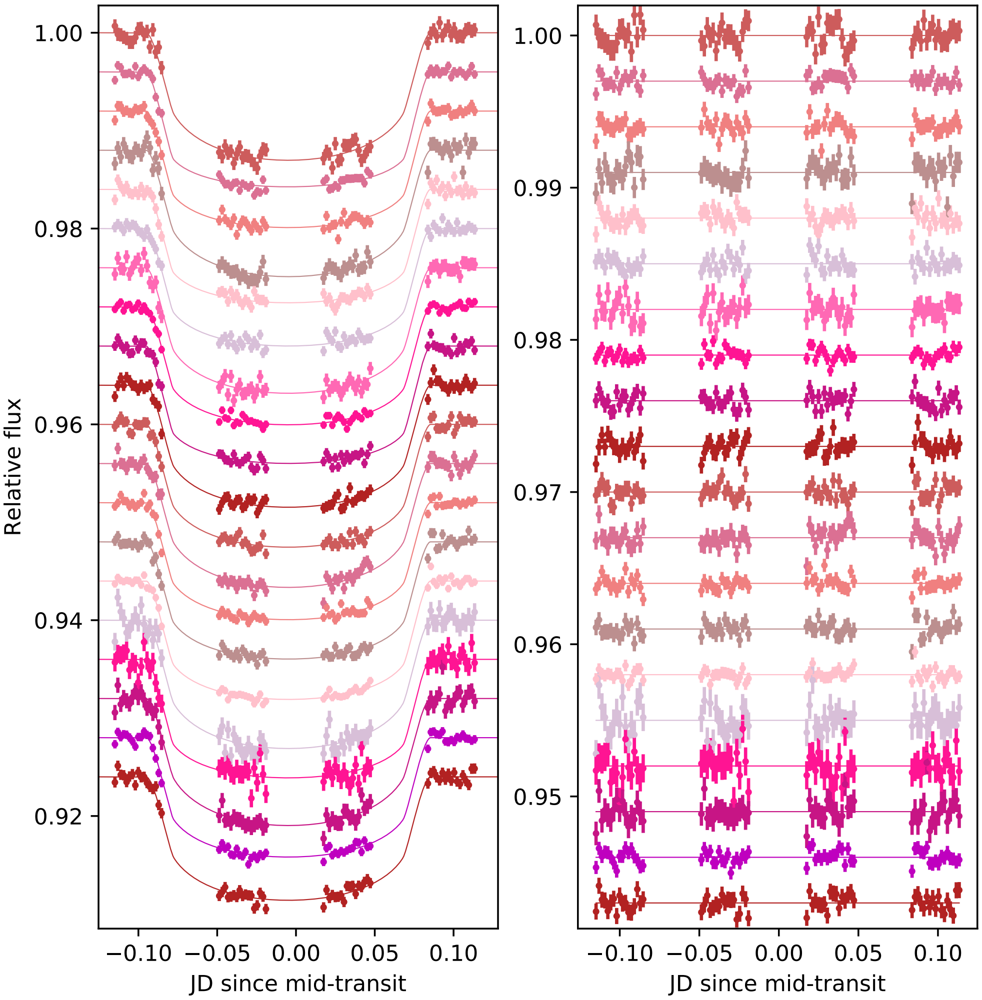

Figure 4.10: Spectroscopic light curves for WASP-127b using HST/STIS+G750L, covering the 5 240−10 270Å wavelength range. (a) Points are light curves divided by systematics models, curves are best-fit transit models. (b) Best-fit model residuals. Arbitrary vertical offsets applied for clarity.

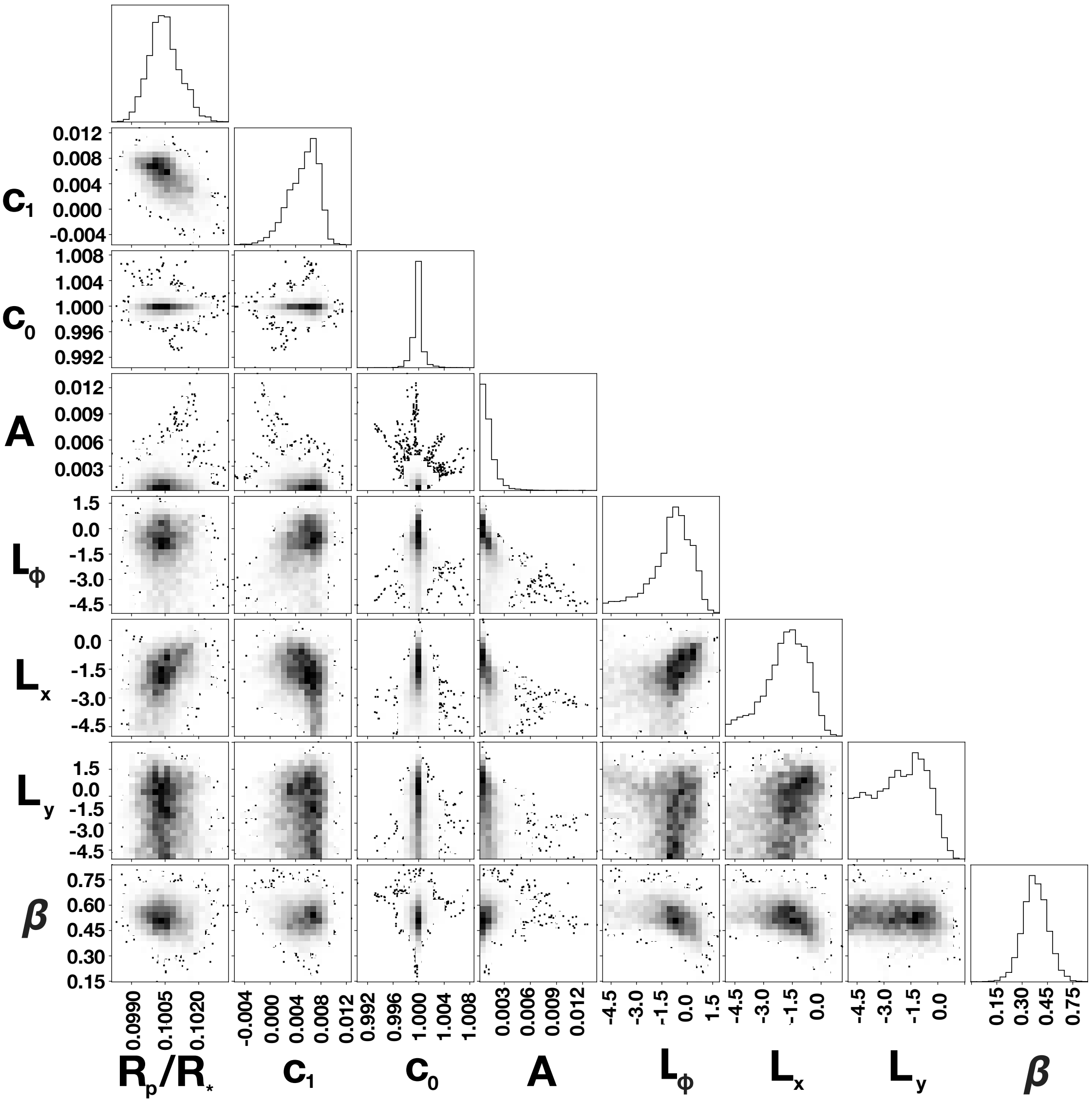

Figure 4.11: Typical posterior distributions for spectroscopic lightcurve MCMC fits for WASP-127b, using HST/STIS+G750L.

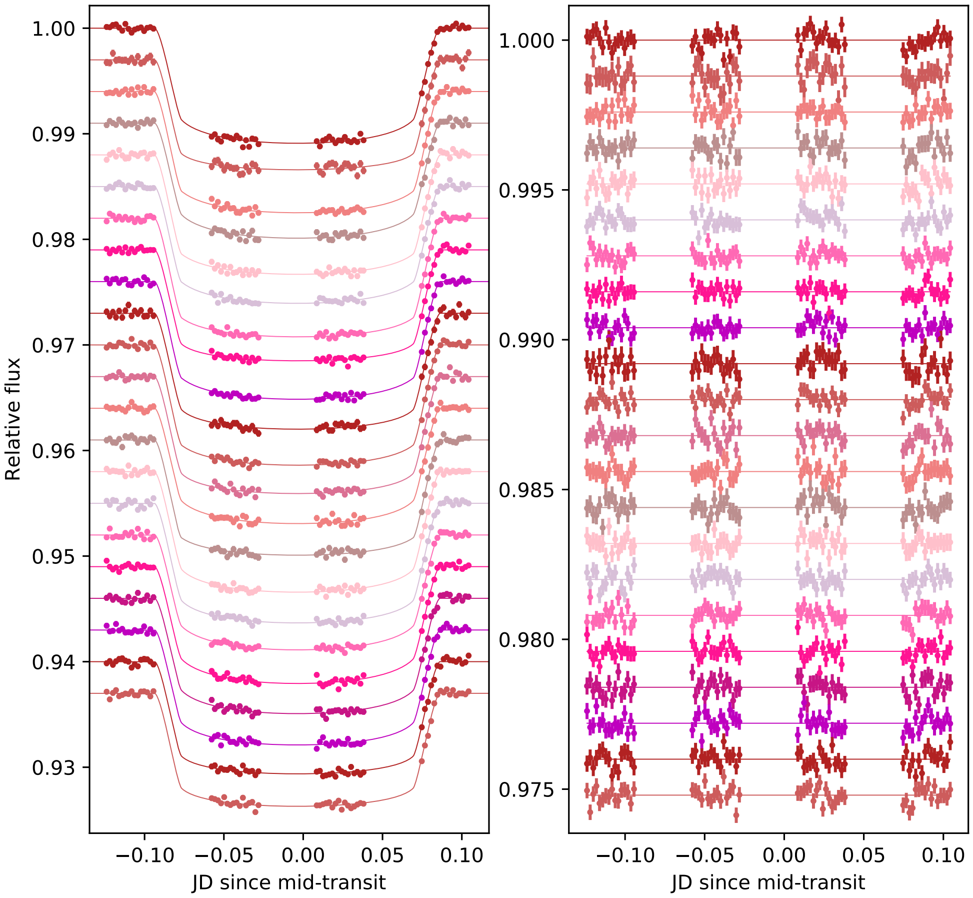

Figure 4.12: Spectroscopic light curves for WASP-127b using HST/WFC3+G141, covering the 11 000-17 000Å wavelength range. (a) Points are light curves divided by systematics models, curves are best-fit transit models. (b) Best-fit model residuals. Arbitrary vertical offsets applied for clarity.

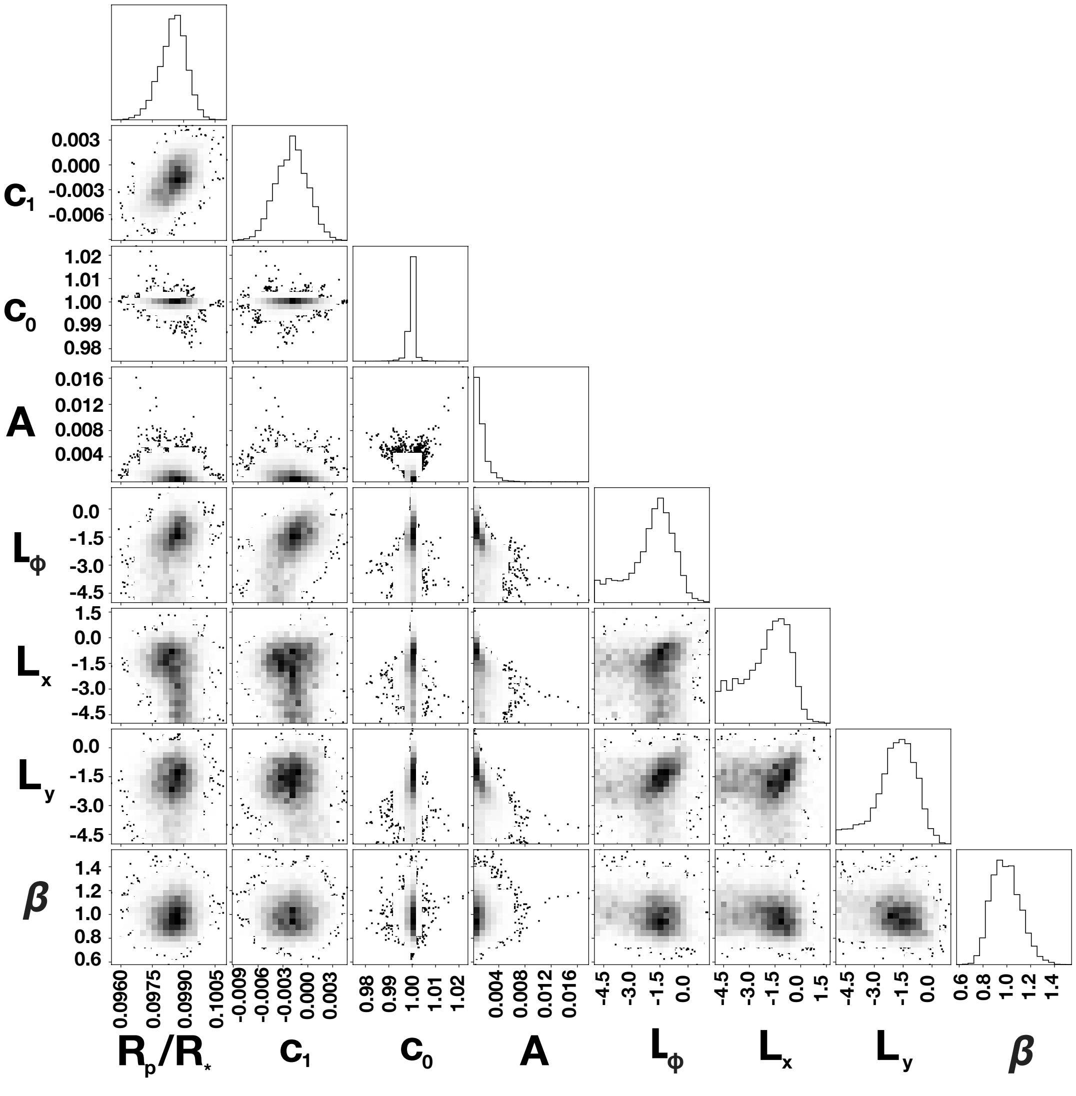

Figure 4.13: Typical posterior distributions for spectroscopic lightcurve MCMC fits for WASP-127b, using HST/WFC3+G141.

Parameter	Value
Transit depth (%)	$0.993^{+0.005}_{-0.005}$
Mid-time (JD)	$2\,457\,846.19996^{+0.00004}_{-0.00003}$
Period (day)	4.178^{a}
a/R_*	8.044^{a}
Inclination (°)	88.7^{a}
Eccentricity	0^{a}
Arg. of Periastron	90^{a}
LD coefficients ($u_{1,2}$)	0.0626^{b}, 0.1734^{b}

Table 4.5: Results from light curve fit for WASP-127b using Spitzer/IRAC 3.6μm channel. [a] planet parameters fixed to values from (Lam et al. 2017). [b] Limb darkening parameters fixed from ATLAS models (Castelli & Kurucz 2004).

the Markov chain Monte Carlo (MCMC) package emcee (Foreman-Mackey et al. 2013) to marginalise over the parameter space of the model likelihood distribution. We used 100 walkers and ran chains for 5 000 steps, discarding the first 1 000 as burn-in before combining the walker chains into a single chain. We followed this procedure for each of the photometric lightcurves that we produced, which used varying aperture sizes from a radius of 1.5 to 6 pixels, in increments of 0.5 pixels. Here we quote the results from the lightcurve which had the lowest model residuals after the fitting process. For the 3.6 μm channel the optimum aperuture radius was 3.0 pixels, and for the 4.5 μm channel it was 2.5 pixels. Tables 4.5 and 4.6 show our best-fit transit depths and mid-transit times for each channel. Figures 4.14 and 4.16 show the light curves with their best-fit models and residuals, and Figures 4.15 and 4.15 show the posterior distributions of these fits.

Our results were consistent with those inferred by a more sophisticated treatment of Spitzer's systematics. Deming et al. (2015) use a technique that involves modelling the light curves of individual pixels to correct for Spitzer's intra-pixel variations, called Pixel Level Decorrelation (PLD). The measured transit depths using both PLD and the light-curve fitting procedure described above are shown in Figure 4.18. For both channels they are consistent within 1σ.

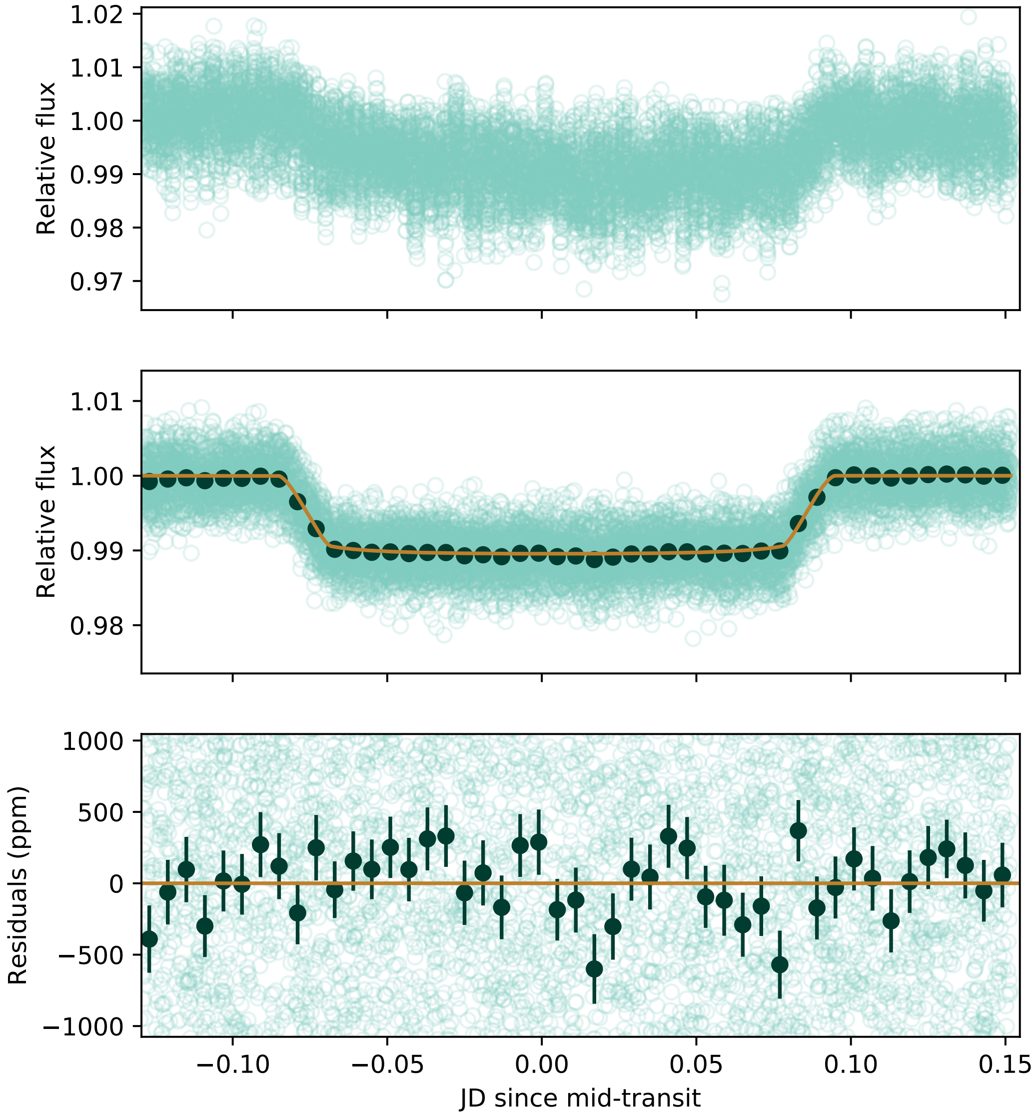

Figure 4.14: Light curve fit for WASP-127b using Spitzer/IRAC's 3.6μm channel. Top panel: light green points are raw data. Middle panel: light green points are data divided by systematics model, dark green points are data in 9-minute bins for clarity, beige curve is the best-fit transit model. Bottom panel: Best-fit model residuals.

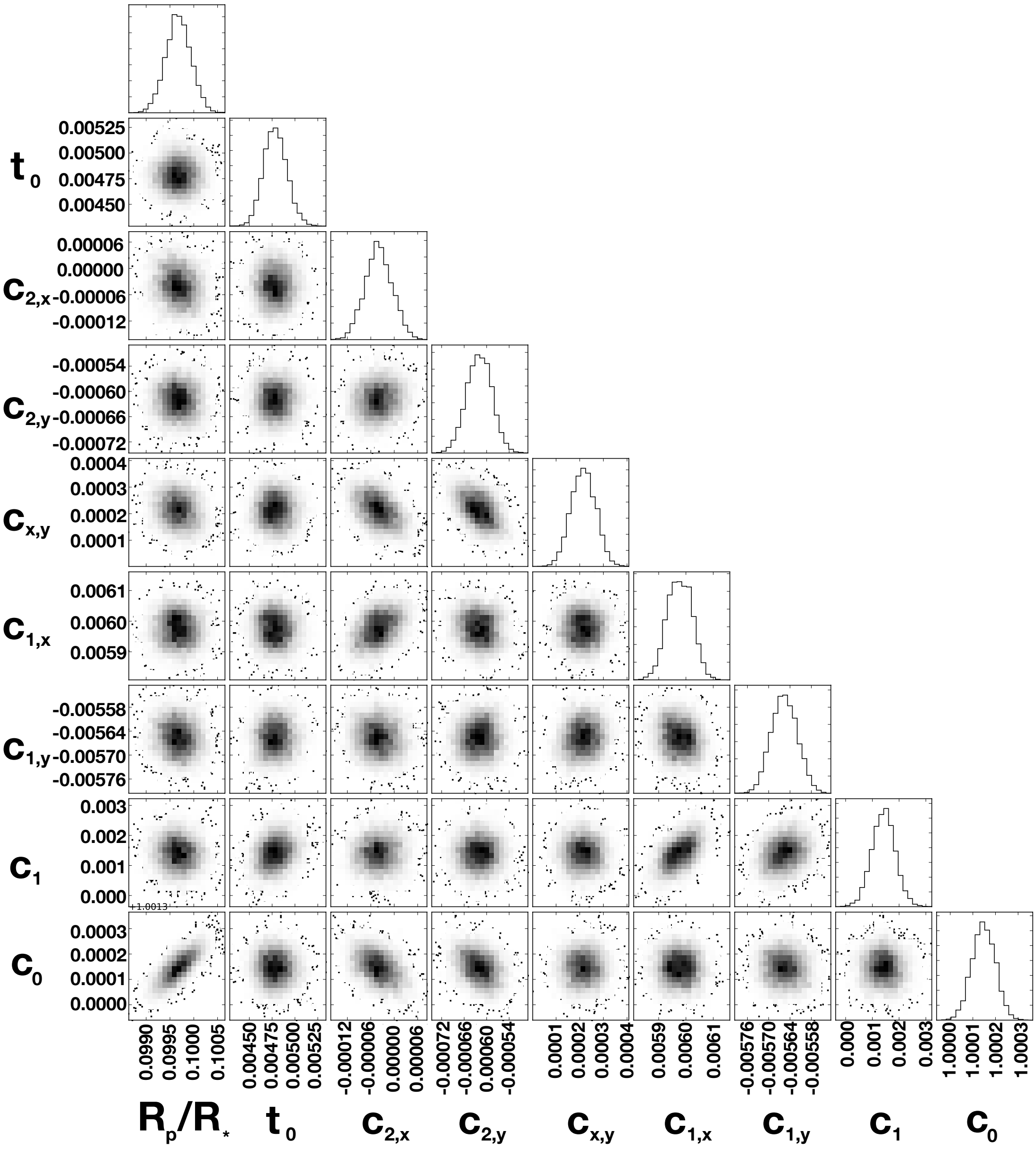

Figure 4.15: Posterior distributions for lightcurve MCMC fits for WASP-127b, using Spitzer/IRAC's 3.6μm channel.

Parameter	Value
Transit depth (%)	$1.073^{+0.006}_{-0.006}$
Mid-time (JD)	$2\,457\,850.37968^{+0.00001}_{-0.00001}$
Period (day)	4.178^{a}
a/R_*	8.044^{a}
Inclination (°)	88.7^{a}
Eccentricity	0^{a}
Arg. of Periastron	90^{a}
LD coefficients ($u_{1,2}$)	0.0639^{b}, 0.1374^{b}

Table 4.6: Results from light curve fit for WASP-127b using Spitzer/IRAC 4.5μm channel. ^{a} planet parameters fixed to values from (Lam et al. 2017). ^{b} Limb darkening parameters fixed from ATLAS models (Castelli & Kurucz 2004).

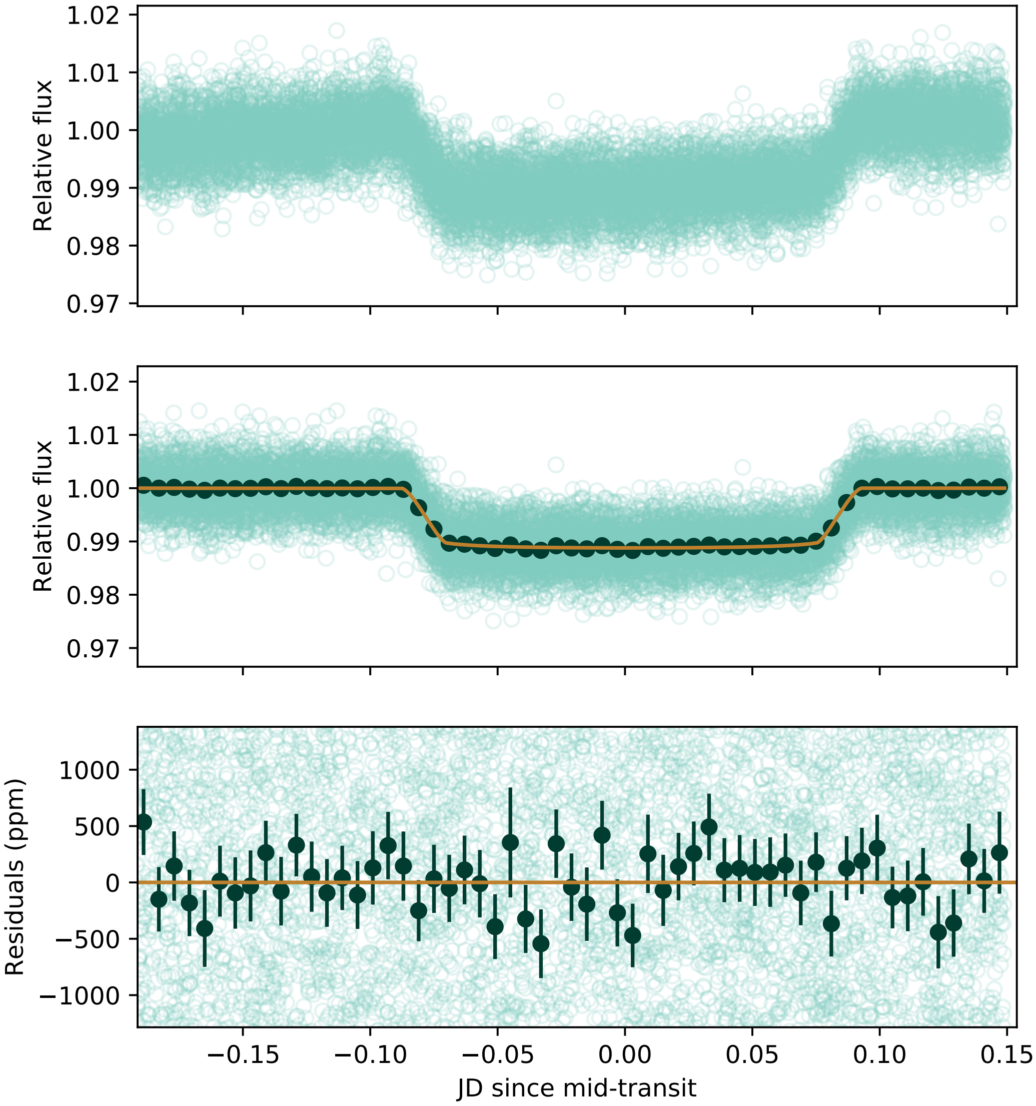

Figure 4.16: Light curve fit for WASP-127b using Spitzer/IRAC's 4.5μm channel. Top panel: light green points are raw data. Middle panel: light green points are data divided by systematics model, dark green points are data in 9-minute bins for clarity, beige curve is the best-fit transit model. Bottom panel: Best-fit model residuals.

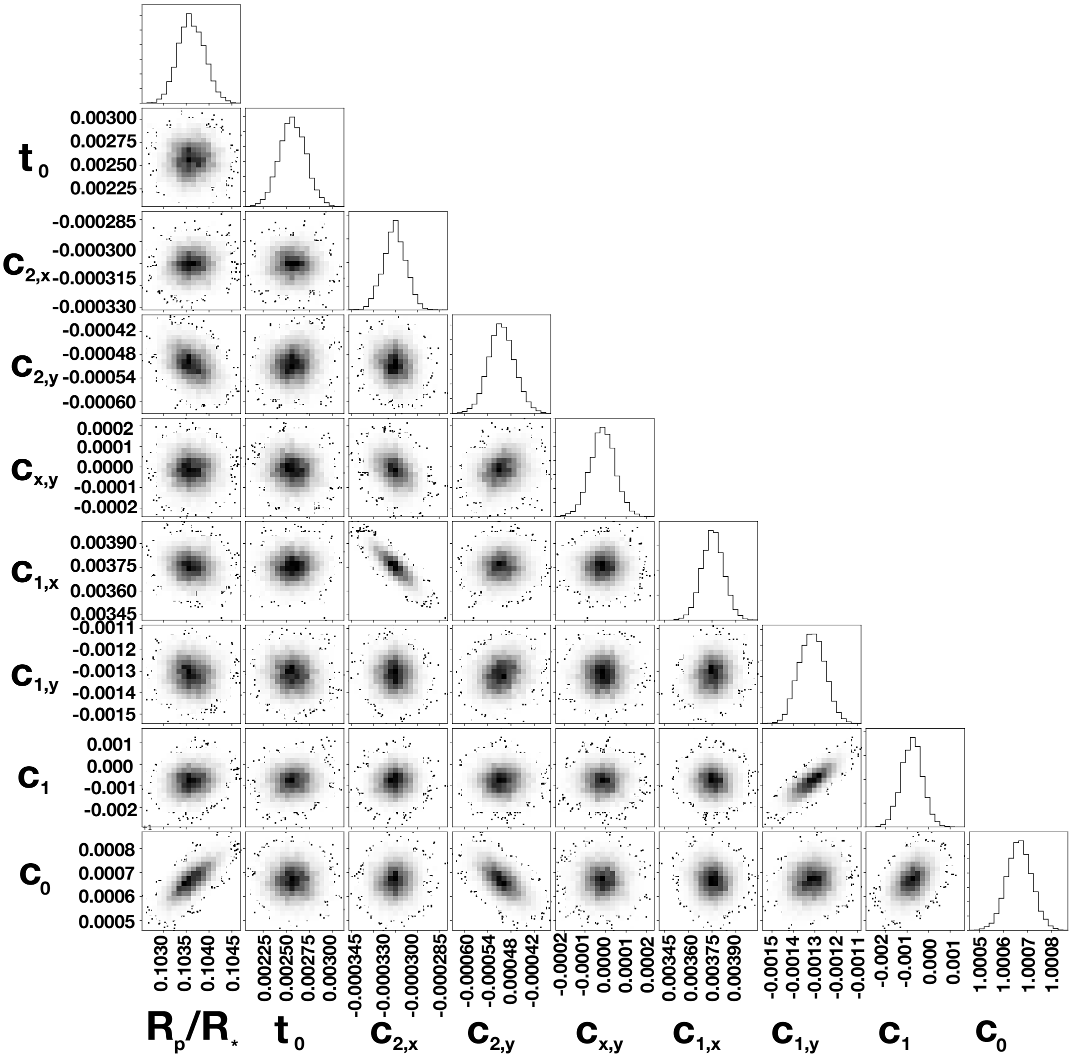

Figure 4.17: Posterior distributions for lightcurve MCMC fits for WASP-127b, using Spitzer/IRAC's 4.5μm channel.

Bin start (Å)	Bin end (Å)	Transit depth (%)	u_1	u_2	u_3	u_4
2 898	3 499	$1.014^{+0.018}_{-0.017}$	0.4877	-0.8372	2.061	-0.7622
3 499	3 700	$1.052^{+0.032}_{-0.027}$	0.5554	-0.8364	2.0977	-0.877
3 700	3 868	$1.041^{+0.016}_{-0.016}$	0.7829	-1.4337	2.4824	-0.8826
3 868	4 041	$1.031^{+0.020}_{-0.020}$	0.6708	-0.9563	1.9288	-0.7115
4 041	4 151	$0.999^{+0.017}_{-0.016}$	0.4952	-0.5838	1.7669	-0.7562
4 151	4 261	$1.027^{+0.018}_{-0.017}$	0.5475	-0.692	1.7829	-0.7211
4 261	4 371	$1.033^{+0.017}_{-0.015}$	0.6388	-0.795	1.7496	-0.6939
4 371	4 426	$1.039^{+0.019}_{-0.017}$	0.5841	-0.68	1.6741	-0.6779
4 426	4 481	$1.042^{+0.024}_{-0.022}$	0.4825	-0.3207	1.3397	-0.6041
4 481	4 536	$1.030^{+0.013}_{-0.014}$	0.4209	-0.0918	1.0989	-0.5366
4 536	4 591	$1.030^{+0.012}_{-0.013}$	0.4257	-0.0758	1.0615	-0.5223
4 591	4 646	$1.030^{+0.015}_{-0.017}$	0.4461	-0.1254	1.1036	-0.5395
4 646	4 701	$1.016^{+0.015}_{-0.017}$	0.4527	-0.1473	1.1347	-0.5582
4 701	4 756	$1.041^{+0.016}_{-0.016}$	0.4636	-0.1446	1.1079	-0.5491
4 756	4 811	$1.022^{+0.021}_{-0.020}$	0.4473	-0.0651	1.0019	-0.5109
4 811	4 921	$1.017^{+0.017}_{-0.017}$	0.5049	-0.183	1.1063	-0.563
4 921	4 976	$1.024^{+0.017}_{-0.015}$	0.4939	-0.1499	1.043	-0.5248
4 976	5 030	$1.025^{+0.016}_{-0.016}$	0.5452	-0.2836	1.1569	-0.5588
5 030	5 085	$1.036^{+0.012}_{-0.011}$	0.5259	-0.2426	1.1354	-0.5611
5 085	5 140	$1.032^{+0.018}_{-0.019}$	0.5533	-0.3454	1.255	-0.6062
5 140	5 195	$1.062^{+0.036}_{-0.038}$	0.6351	-0.5715	1.4359	-0.6527
5 195	5 250	$1.065^{+0.018}_{-0.016}$	0.5824	-0.3658	1.2123	-0.5817
5 250	5 305	$0.998^{+0.019}_{-0.019}$	0.5917	-0.3491	1.1553	-0.5552
5 305	5 360	$1.029^{+0.021}_{-0.020}$	0.5743	-0.2918	1.0939	-0.538
5 360	5 415	$1.054^{+0.023}_{-0.019}$	0.5772	-0.2965	1.0937	-0.5395
5 415	5 469	$1.028^{+0.012}_{-0.013}$	0.5728	-0.2814	1.0784	-0.5375
5 469	5 524	$1.003^{+0.017}_{-0.015}$	0.5945	-0.3392	1.1278	-0.553
5 524	5 579	$1.035^{+0.033}_{-0.034}$	0.5909	-0.3093	1.0808	-0.5368
5 579	5 634	$1.016^{+0.023}_{-0.018}$	0.5988	-0.3263	1.0897	-0.5401
5 634	5 688	$1.023^{+0.017}_{-0.016}$	0.6094	-0.3448	1.0904	-0.5355

Table 4.7: Results from spectroscopic light curve fits for WASP-127b, using HST/STIS+G430L. Fixed, four-parameter limb darkening law coefficients denoted by u_i

Bin start (Å)	Bin end (Å)	Transit depth (%)	u_1	u_2	u_3	u_4
5 500	5 600	$1.044^{+0.020}_{-0.020}$	0.5963	-0.3281	1.1005	-0.5429
5 600	5 700	$1.024^{+0.017}_{-0.015}$	0.6029	-0.3282	1.0782	-0.5331
5 700	5 800	$1.014^{+0.025}_{-0.020}$	0.5987	-0.2994	1.0337	-0.5182
5 800	5 878	$1.042^{+0.017}_{-0.020}$	0.593	-0.2704	0.9903	-0.5042
5 878	5 913	$0.993^{+0.032}_{-0.026}$	0.6326	-0.3954	1.1143	-0.5468
5 913	6 070	$1.015^{+0.017}_{-0.018}$	0.6126	-0.3129	1.0114	-0.5113
6 070	6 200	$1.046^{+0.020}_{-0.019}$	0.6537	-0.4235	1.0947	-0.5342
6 200	6 300	$1.009^{+0.015}_{-0.012}$	0.6632	-0.4382	1.094	-0.5331
6 300	6 450	$1.037^{+0.023}_{-0.027}$	0.6696	-0.455	1.0978	-0.5349
6 450	6 600	$1.020^{+0.014}_{-0.014}$	0.6986	-0.4715	1.0601	-0.5246
6 600	6 800	$1.031^{+0.016}_{-0.015}$	0.6883	-0.5005	1.1059	-0.5346
6 800	7 000	$1.017^{+0.017}_{-0.017}$	0.7015	-0.5355	1.1128	-0.5306
7 000	7 200	$0.996^{+0.014}_{-0.012}$	0.732	-0.6214	1.1791	-0.551
7 200	7 450	$0.996^{+0.018}_{-0.014}$	0.7449	-0.658	1.1933	-0.5537
7 450	7 645	$1.019^{+0.016}_{-0.015}$	0.7339	-0.6262	1.1383	-0.5317
7 645	7 720	$1.061^{+0.024}_{-0.024}$	0.7356	-0.6251	1.115	-0.5196
7 720	8 100	$1.028^{+0.028}_{-0.025}$	0.749	-0.6699	1.1521	-0.5322
8 100	8 485	$1.036^{+0.025}_{-0.023}$	0.7713	-0.7465	1.2143	-0.555
8 485	8 985	$1.011^{+0.015}_{-0.013}$	0.7557	-0.7033	1.1225	-0.5143
8 985	10 235	$1.024^{+0.013}_{-0.016}$	0.7199	-0.6087	0.9679	-0.4452

Table 4.8: Results from spectroscopic light curve fits for WASP-127b, using HST/STIS+G750L. Fixed, four-parameter limb darkening law coefficients denoted by u_i

4.5 ATMO Retrieval

For the combined STIS, WFC3 and Spitzer spectrum of WASP-127b, we performed an atmospheric retrieval analysis using a one-dimensional radiative transfer code for planetary atmospheres, ATMO (Amundsen et al. 2014; Tremblin et al. 2015, 2016). ATMO solves the radiative transfer equation for a given set of opacities, temperature-pressure (TP) profile, and chemical abundances. The code can also solve for the TP profile that satisfies hydrostatic equilibrium and conservation of energy, but we do not use this function for the initial analysis presented here. ATMO includes a relatively simple treatment of clouds and hazes, and the following description is based on a that from Goyal et al. (2018): ATMO does not consider the type or distribution of condensate particles. Instead, the scattering effects on the transmission spectrum are paramaterised as follows. Scattering by haze is implemented

Bin start (Å)	Bin end (Å)	Transit depth (%)	u_1	u_2	u_3	u_4
11 225	11 409	$1.029^{+0.012}_{-0.012}$	0.6515	-0.4064	0.6627	-0.3206
11 409	11 594	$1.026^{+0.010}_{-0.012}$	0.6312	-0.3375	0.5764	-0.2851
11 594	11 779	$0.998^{+0.011}_{-0.012}$	0.6281	-0.3166	0.544	-0.2745
11 779	11 963	$0.981^{+0.007}_{-0.009}$	0.6205	-0.287	0.5009	-0.2564
11 963	12 148	$0.975^{+0.012}_{-0.012}$	0.6093	-0.2483	0.4502	-0.2362
12 148	12 333	$0.981^{+0.009}_{-0.009}$	0.5884	-0.162	0.3459	-0.1968
12 333	12 517	$0.971^{+0.011}_{-0.014}$	0.5787	-0.1206	0.2867	-0.1716
12 517	12 702	$0.985^{+0.009}_{-0.012}$	0.5727	-0.0874	0.2388	-0.1533
12 702	12 887	$0.975^{+0.012}_{-0.010}$	0.5709	-0.0386	0.1613	-0.1299
12 887	13 071	$0.978^{+0.010}_{-0.011}$	0.554	0.006	0.1075	-0.0997
13 071	13 256	$1.023^{+0.009}_{-0.010}$	0.5476	0.0484	0.0384	-0.0685
13 256	13 441	$0.980^{+0.007}_{-0.008}$	0.5386	0.1046	-0.0462	-0.0321
13 441	13 625	$0.993^{+0.012}_{-0.011}$	0.5338	0.1452	-0.1094	-0.0057
13 625	13 810	$1.020^{+0.009}_{-0.010}$	0.5332	0.1813	-0.1788	0.0266
13 810	13 995	$0.977^{+0.008}_{-0.009}$	0.5265	0.2444	-0.2789	0.0708
13 995	14 179	$0.961^{+0.010}_{-0.011}$	0.5238	0.2836	-0.3521	0.1059
14 179	14 364	$1.032^{+0.008}_{-0.008}$	0.5301	0.2999	-0.4012	0.1308
14 364	14 549	$0.972^{+0.009}_{-0.009}$	0.5418	0.3015	-0.431	0.1464
14 549	14 733	$0.983^{+0.009}_{-0.010}$	0.5518	0.3122	-0.4668	0.1632
14 733	14 918	$1.003^{+0.008}_{-0.009}$	0.567	0.29	-0.4699	0.1709
14 918	15 102	$1.009^{+0.011}_{-0.013}$	0.5795	0.2891	-0.5072	0.1952
15 102	15 287	$1.030^{+0.009}_{-0.010}$	0.5983	0.31	-0.585	0.2369
15 287	15 472	$1.010^{+0.012}_{-0.014}$	0.631	0.2627	-0.5741	0.2409
15 472	15 656	$1.026^{+0.012}_{-0.015}$	0.6489	0.2307	-0.5607	0.2408
15 656	15 841	$0.953^{+0.011}_{-0.010}$	0.6836	0.13	-0.4668	0.2097
15 841	16 026	$0.980^{+0.013}_{-0.012}$	0.7076	0.0634	-0.4054	0.19
16 026	16 210	$0.968^{+0.010}_{-0.012}$	0.7347	0.0371	-0.4274	0.21
16 210	16 395	$0.967^{+0.011}_{-0.010}$	0.7468	0.0085	-0.4018	0.2017

Table 4.9: Results from spectroscopic light curve fits for WASP-127b, using HST/WFC3+G141. Fixed, four-parameter limb darkening law coefficients denoted by u_{i}

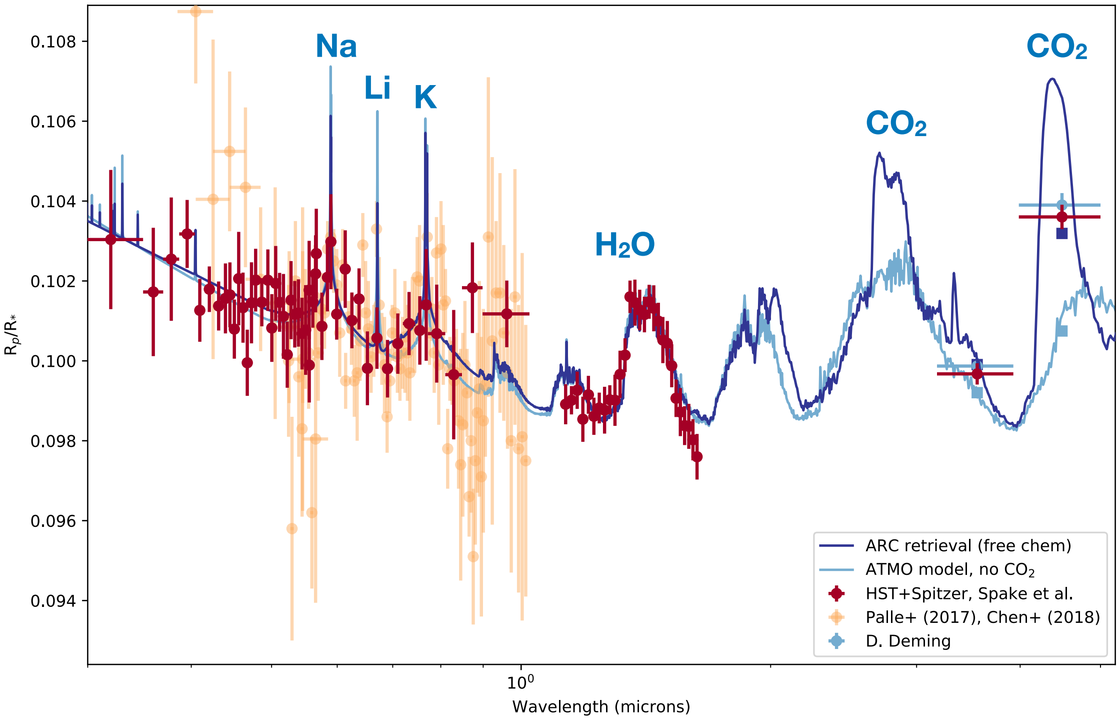

Figure 4.18: Transmission spectrum for WASP-127b. Red data points are from this work, blue data points are from an independent analysis of the Spitzer light curves from D. Deming. Yellow points are previously published data from Palle et al. (2017) and Chen et al. (2018) using ground-based telescopes. Dark blue line is are our best-fit retrieval models using ARC and MPFIT, light blue line is same model with CO_2 abundance set to zero. Square points show models binned to the resolution of the Spitzer data.

as enhanced Rayleigh scattering, presented as

$$\sigma(\lambda) = \alpha_{\mathrm{haze}}\sigma_0(\lambda), \tag{4.2}$$

where $\sigma(\lambda)$ is the total scattering cross-section of the haze, α_{haze} is an empirical enhancement factor, and $\sigma_0(\lambda)$ is the scattering due to all other gases at a particular wavelength (ATMO considers multigas scattering). The strength of grey scattering caused by large-particled clouds is represented by

$$\kappa(\lambda)_{\mathrm{c}} = \kappa(\lambda) + \alpha_{\mathrm{cloud}}\kappa_{\mathrm{H2}}, \tag{4.3}$$

where $\kappa(\lambda)_{\mathrm{c}}$ is the total scattering opacity, $\kappa(\lambda)$ is the scattering opacity due to nominal Rayleigh scattering, α_{cloud} is an empirical factor governing the strength of the grey scattering, and κ_{H2} is the scattering opacity due to H_2 at 3 500Å.

We performed a retrieval using the Atmo Retrieval Code (ARC) previously described in Wakeford et al. (2017) and Evans et al. (2017). We assumed an isothermal temperature-pressure profile, and used the IDL MCMC implementation of Eastman et al. (2013) to find a best fit model for the following parameters: atmospheric temperature; planetary radius at a pressure of 1 mbar; α_{cloud}; α_{haze}; and the relative abundances of H_2O, CO_2, CO, NH_4, Na, Li, and K. We assumed solar abundances under chemical equilibrium for other gas species. We ran 12 MCMC chains for 30 000 steps, discarding the first 3 000 steps as burn-in. Table 4.10 gives our best-fitting model parameters and 1 σ uncertainties (which correspond to the range of parameters which contain 68% of the MCMC samples). Our best-fitting model is shown in Figure 4.18, and the posterior distributions of the MCMC fit are shown in 4.19.

4.6 Results and Discussion

The transmission spectrum of WASP-127b shows evidence of wavelength-dependent scattering in the optical; absorption by sodium and potassium; a grey absorber in the infrared which mutes the molecular absorption features; water absorption; and evidence of CO_2 (see Figure 4.18). We do not see the sharp rise blueward of 5 600Å that Chen et al. (2018) report from the ground-based NOT data. Instead, we find a shallower slope, presumably caused by scattering off some kind of haze made from small ($< 1\mu m$) particles, which slopes down into the near-infrared. We note that ground-based optical transmission spectra frequently suffer from differential atmospheric extinction problems at $< 0.4\mu m$.

Our free retrieval favours strong absorption by CO_2 - the best-fit model gives a natural log of the fractional abundance of -5.7±0.7. To highlight the evidence for CO_2 in the transmission spectrum, in Figure 4.18 we show a model atmosphere with all the same parameters as the best fit model, except the CO_2 abundance, which is set to zero. The strong absorption feature centred on the 4.5 μm Spitzer channel disappears. However, Heng & Lyons (2016) suggest that CO should be

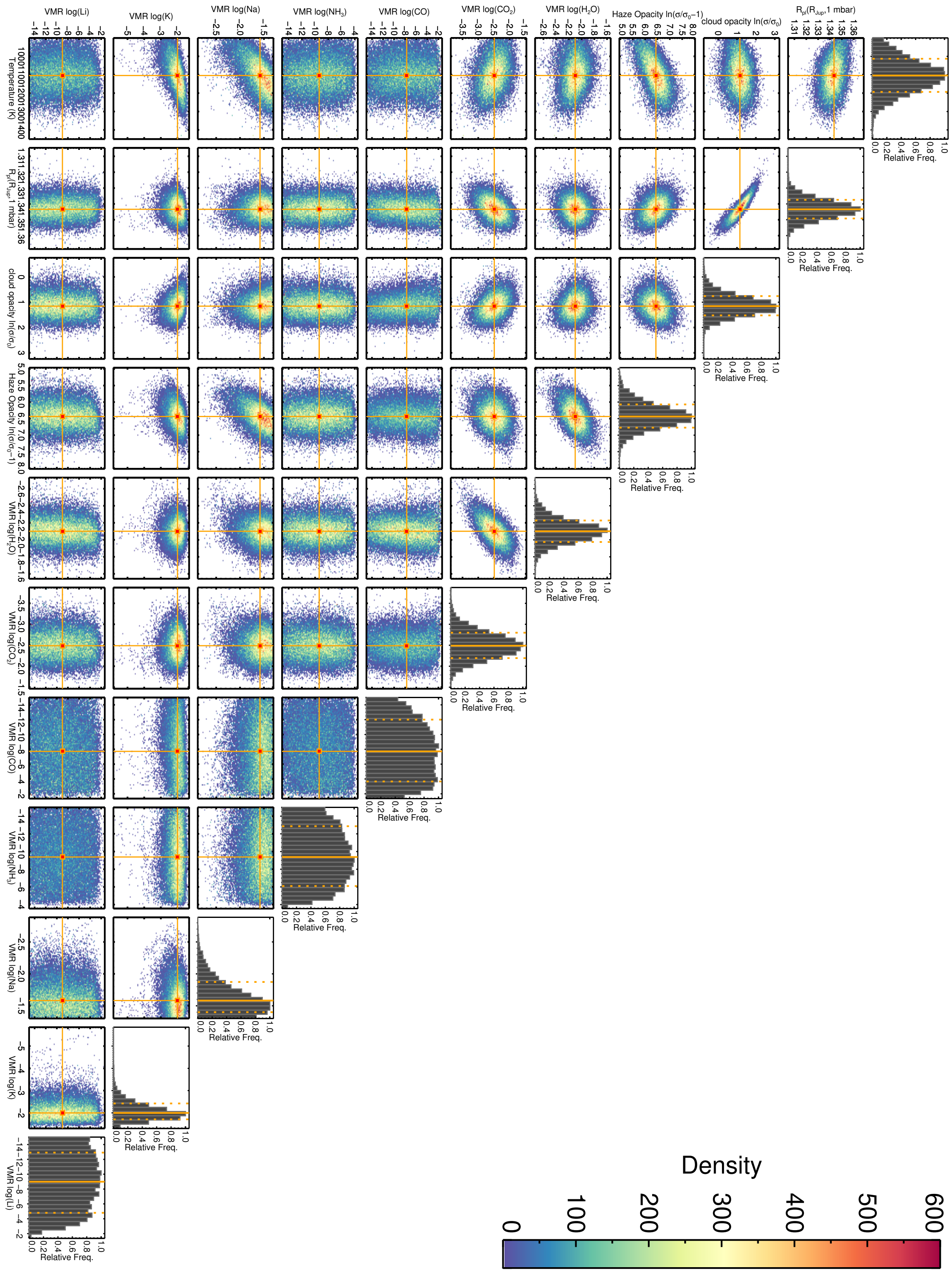

Figure 4.19: Posterior distributions for atmospheric retrieval MCMC fit for WASP-127b. Colours represent density of MCMC samples; solid orange lines show median values; dashed orange lines contain 68% of samples.

the dominant carbon-bearing molecule for hydrogen-dominated atmospheres above 1 000K. WASP-127b is expected to have an equilibrium temperature of 1 400K, but on the other hand, our best fit temperature is only 1107±91K. There is a CO feature at the ~4.5 micron that may explain the increased opacity there (e.g. Goyal

Parameter	Value
T_{eff} (K)	1107±91
$R_{P,1bar}$ (R_J)	1.343±0.005
Cloud[a]	1.16±0.38
Haze[a]	6.44±0.35
H_2O[b]	-4.8±0.3
CO_2[b]	-5.7±0.7
CO[b]	-17.7±9.7
NH_3	-21.6±8.1
Na[b]	-3.6±0.5
K[b]	-4.5±0.8
Li[b]	-20.5±9.2

Table 4.10: Results from ATMO retrieval MPFIT to WASP-127b's transmission spectrum. [a]The cloud and haze strengths are defined in Section 4.5. [b]The units of chemical composition are natural log of the fractional abundances for each molecule.

et al. 2019). But with only one data point, it is almost impossible to say which species is causing the extra absorption. Further transmission spectroscopy observations of WASP-127b with the James Webb Space Telescope will clarify which is the dominant carbon-bearing molecule in WASP-127b's atmosphere, and allow stronger constraints to be placed on its carbon-to-oxygen ratio.

Overall, we have observed evidence of strong absorption features from several atomic and molecular species, which means that the level of hazes of clouds in WASP-127b is not so strong as to prevent the determination of its atmospheric composition. This evidence, combined with a long transit duration, means that WASP-127b is the ideal benchmark exoplanet for measuring chemical abundances of exoplanet atmospheres and should be one of the prime targets for James Webb Space Telescope (JWST, see Chapter 5). In particular, the hint of a large absorption feature around 4.5μm is strong evidence that future observations of WASP-127b with JWST will be able to measure the abundances of carbon-bearing species in its atmosphere.

Chapter 5

Conclusion

5.1 Summary of Thesis Achievements

This work is comprised of three observational projects on three different transiting exoplanets. The first was a near-infrared transmission spectrum of the relatively cool gas giant WASP-107b using HST/WGC3+G102. The overall shape of the spectrum was relatively flat, which suggests clouds are evident in WASP-107b's atmosphere. The flat spectrum is consistent with previous transmission spectroscopy measurements of WASP-107b made with the other WFC3 grism (G141), by Kreidberg et al. (2018). The more significant result from this project was the first detection of helium on an exoplanet. We measured absorption in the narrow line of metastable helium at 10 830Å , at a significance of 4.5σ. The amplitude of the signal was 0.049±0.011% in a bandpass of 98Å , which suggests that the core of the absorption line reaches 6±1% in transit depth. The deep core of the absorption line suggests that WASP-107b is shrouded in a cloud of helium that extends up to tens of thousands of kilometers in altitude above the observed cloud deck in its lower atmosphere (at least up to 1.6 planetary radii). Even though this height falls within WASP-107b's Roche radius - so we observe no direct evidence for atmospheric escape - our observations are consistent with a one-dimensional escaping atmosphere model which suggests WASP-107b is losing 0.1-4% of its atmosphere every gigayear.

This first detection of helium in an extended exoplanet atmosphere has opened the door to a small wave of helium detections in other exoplanet atmospheres (Allart et al. 2018; Nortmann et al. 2018; Salz et al. 2018), and it represents a new way to study the diffuse upper atmospheres of exoplanets that have so far been difficult to study.

The second chapter described observations of a near-infrared phase curve of the hot exoplanet WASP-19b, using HST/WFC3+G141. The aim of this project was to probe deeper into WASP-19b's atmosphere than had been observed before, down to pressures of 1-10 bar (previous Spitzer phase curves were sensitive to ∼1mbar bar), using the 1.7 - 1.7 μm wavelength region that is expected to be dominated by water opacities, rather than clouds. Our results suggest the planet has a large phase-curve hotspot offset of $57^{+21\circ}_{-16}$, and a relatively small phase-curve amplitude of $0.60^{+0.06}_{-0.08}$. Both results indicate that our observations probe a region of the atmosphere that is dominated by a strong, equatorial jet that efficiently re-distributes heat around the planet. This finding agrees with predictions from general circulation models of the planet at pressures of 1 bar (e.g. Kataria et al. 2016). WASP-19b is the first exoplanet to have such a large hotspot offset measured with HST/WFC3. Interestingly, exoplanets with both lower- and higher equilibrium temperatures have much smaller measured hotspot offsets than WASP-19b, which could mean that WASP-19b falls into a middling temperature regime that is hot enough to drive strong equatorial jets, but not hot enough to cause magnetic breaking (by atmospheric ionisation, e.g. Perna et al. 2010). However, more planets with similar equilibrium temperatures to WASP-19b will need to be studied to confirm this.

The final project was a near-UV to near-infrared transmission spectrum of the puffy gas giant WASP-127b using HST and Spitzer. The aim of this project was to classify the planet's atmosphere as clear or condensate-dominated, and begin understanding its atmospheric composition by measuring the relative abundances of sodium, potassium, and water. We observe some evidence for condensates on WASP-127b, but not enough to mask all atmospheric absorption features from the transmission spectrum, which is information-rich. Summarising our results starting with the short-wavelength end of the transmission spectrum: we observe a fairly shallow slope downwards from the near-UV, which is inconsistent with a previously-reported spectrum of WASP-127b measured using ground-based telescopes, which shows a sharp rise blue-ward of 0.4 microns (Palle et al. 2017). The contrasting results may be due to the difficulty in correcting for telluric contamination and measuring precise and accurate transmission spectra from the ground - especially at shorter wavelengths where interference is particularly strong. We see evidence for both sodium and potassium, but no strong evidence for lithium, as has been previously reported (Chen et al. 2018). We measure a strong water absorption feature at 1.4 μm, although its amplitude suggests there may be some grey opacity source at high alititudes. Finally, concerning our two photometric data points measured with Spitzer: the 4.5 μm channel gives a significantly deeper transit depth than the 3.6 μm channel. This suggests there is a strong absorption feature at around 4.5 μm, which could be due to either carbon monoxide or carbon dioxide. In either case, the evidence for strong absorption features in WASP-127b's infrared transmission spectrum means it is an outstanding target for future observations with the James Webb Space telescope, which can be used to measure its atmospheric carbon-to-oxygen ratio and perhaps shed light on the formation and migration history of the planet.

5.2 The future

What is the overall chemical composition of a given exoplanet? How did it migrate and evolve over time? These questions will be the focus of much of exoplanet science in the future. We need answers to these two questions for many exoplanets if we want to paint a coherent picture of what kinds of planetary systems form around which stars, and hence understand how common true Earth-twins might be, for example. Exoplanet atmospheres are a window into planet interiors and histories that are inaccessible to mass and radius measurements alone - because different mixtures of atoms and molecules can give the same bulk densities, and the compressible nature of fluids under the influence of gravity further complicates the issue. White dwarfs that are polluted by infalling exoplanetary remnants provide another fascinating inroad to bulk compositions (e.g. Zuckerman et al. 2007), and have even led to measurements of relative abundances similar to Earth rock (Hollands et al. 2018). We do not have complete theories of planet formation and evolution, because it is still unclear how and where hot Jupiters form in protoplanetary disks (e.g. Nelson et al. 2017; Dawson & Johnson 2018), and we do not know what super-Earths and mini-Neptunes[1] *are* - i.e. whether they have significant envelopes of hydrogen and helium, or are mostly made of water, methane, and ammonia, like the ice giants of the Solar System. There is no known super-Earth or mini-Neptune in the Solar System, yet they appear to be the most common planets in the Galaxy (e.g. Dressing & Charbonneau 2015; Fulton et al. 2017).

To answer our questions we must measure the compositions of exoplanet atmospheres. This is complicated by several physical effects, which need to be understood. Firstly, clouds and hazes mask absorption features in exoplanet spectra, so we need to know where and how they form (one of the aims in Chapter 4). Secondly, exoplanets are 3D objects whose temperature, winds, and chemistry vary with latitude, longitude, and altitude. Disequilibrium processes can put more or less of a particular gas than expected in the region of the atmosphere we observe (e.g. Beer 1975), and previously unconsidered effects (like H_2 dissociation, e.g. Bell et al. 2017) can mask absorption features as clouds do. Therefore 3D maps of the temperature distribution of planets are required (Chapter 3). Finally, we need to know how exoplanet atmospheres evolved over time, for example whether they started with a large H/He envelope that evaporated away. Chapter 2 presented a new method to observe extended and escaping exoplanet atmospheres. The following sections discuss two new space telescopes that will be key to our future understanding of exoplanet atmospheres; and the follow-up work that should be completed as a result of the projects presented here.

---

[1] here I refer to planets with radii between 1.5 and 4 Earth radii

5.2.1 TESS

Transiting Exoplanet Survey Satellite (TESS) is a space-based telescope on a wide-Earth orbit, with a period of 13.7 days. It takes photometric measurements of stars across nearly the entire sky in order to discover exoplanets via the transit method. The aim of the TESS mission is to detect small exoplanets orbiting stars that are bright enough for mass determination with the radial velocity technique (Ricker et al. 2015). It was launched on 18 April 2018, has a two-year primary mission, and it has already led to the discovery of several exoplanets (Huang et al. 2018, Vanderspek et al. 2019, Wang et al. 2019, Nielsen et al. 2019, Jones et al. 2018, Esposito et al. 2019), including a sub-Earth sized planet with a likely rocky composition (Dragomir et al. 2019).

In a simulation of the expected yeild, Barclay et al. (2018) estimated that TESS will find 1250±70 exoplanets, including 250 smaller than 2 Earth radii. As Figure 5.1 shows, many of these small planets will orbit nearby stars ($<$ 100 parsec), and may therefore be amenable to atmospheric characterisation with transmission spectroscopy. Studying the atmospheres of small planets has so far been difficult, because (1) few $<$ 4 Earth radii planets have been found around bright stars, and (2) the small size of the planets mean their atmospheric signals are small. TESS will help solve the first problem, and the next two sections discuss possible solutions to the second.

5.2.2 JWST

The James Webb Space Telescope (JWST) is a 6.5m-diameter space telescope, set to launch in 2021, which will act as a successor to the Hubble Space Telescope. JWST will be deployed near the Earth-Sun L_2 lagrange point. It has a wavelength coverage of 0.6 - 28.5 μm, so is primarily and infrared telescope, and its suite of four instruments (NIRCam, NIRSpec, MIRI, and NIRISS) will provide a great range of imaging and spectroscopic capabilities. Because of its versatility, JWST will be used

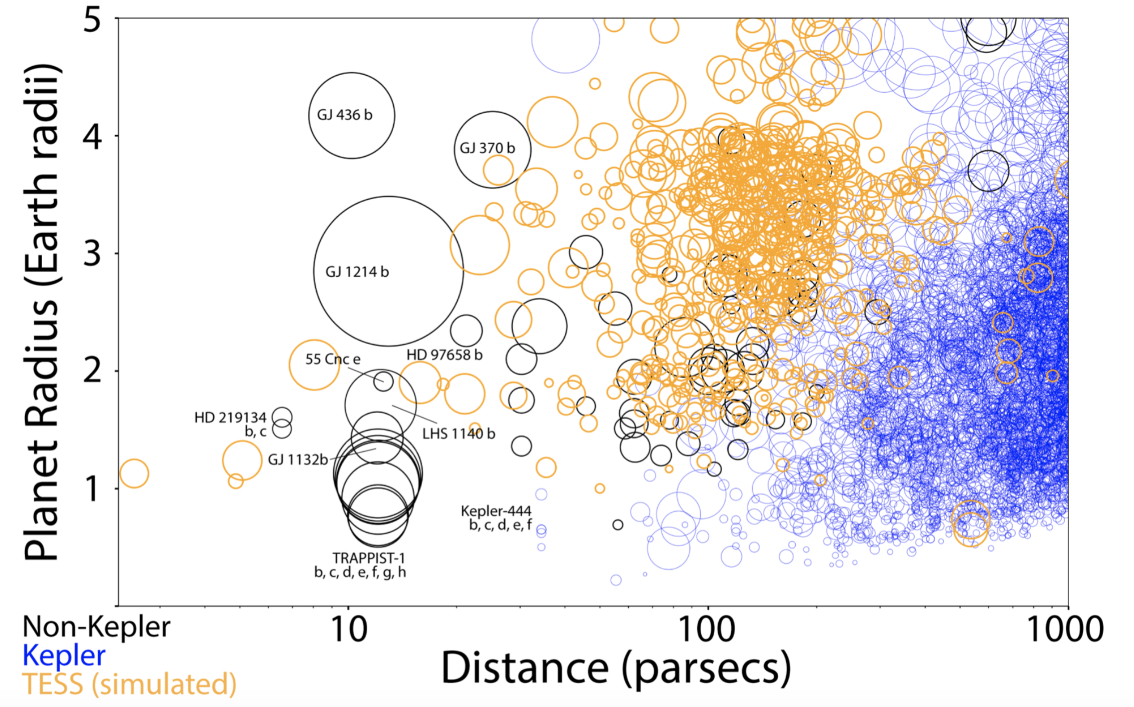

Figure 5.1: TESS small-planet yield, in orbital distance versus planet radii. Kepler planet candidates from Thompson et al. (2018) are shown in blue, our simulated TESS detections in orange, and planets detected using other telescopes in black. The size of the circle is proportional to the transit depth. A subset of nearby planets are marked. Figure and caption from Barclay et al. (2018)

to answer a diverse set of questions from many branches of astronomy, including how the first galaxies in the universe formed, and what the atmospheres of exoplanets are made of.

Figure 5.2 shows the much larger collecting power of JWST compared to HST. The larger mirror will give JWST a sensitivity 3× greater than HST, which, coupled with its 10× greater spectral range, means it will become the superlative instrument for exoplanet atmosphere characterisation.

It has so far proven difficult to detect absorption features in the atmospheres of planets with radii smaller than 4 Earth radii. However, Greene et al. (2016) model transmission and emission spectra for several classes of exoplanets, and use them to simulate JWST observations in several instrument modes. They find that with JWST it will be possible to constrain the major atmospheric constituents of cool (500K) planets as small as 2 Earth radii, provided their amtospheres are cloud-free and of solar composition. We can therefore expect JWST to revolutionise our understanding of exoplanet atmospheres, and allow us to observe smaller and cooler exoplanets than has previously been possible. Small planets around bright stars found with TESS will be ideal targets for JWST observations.

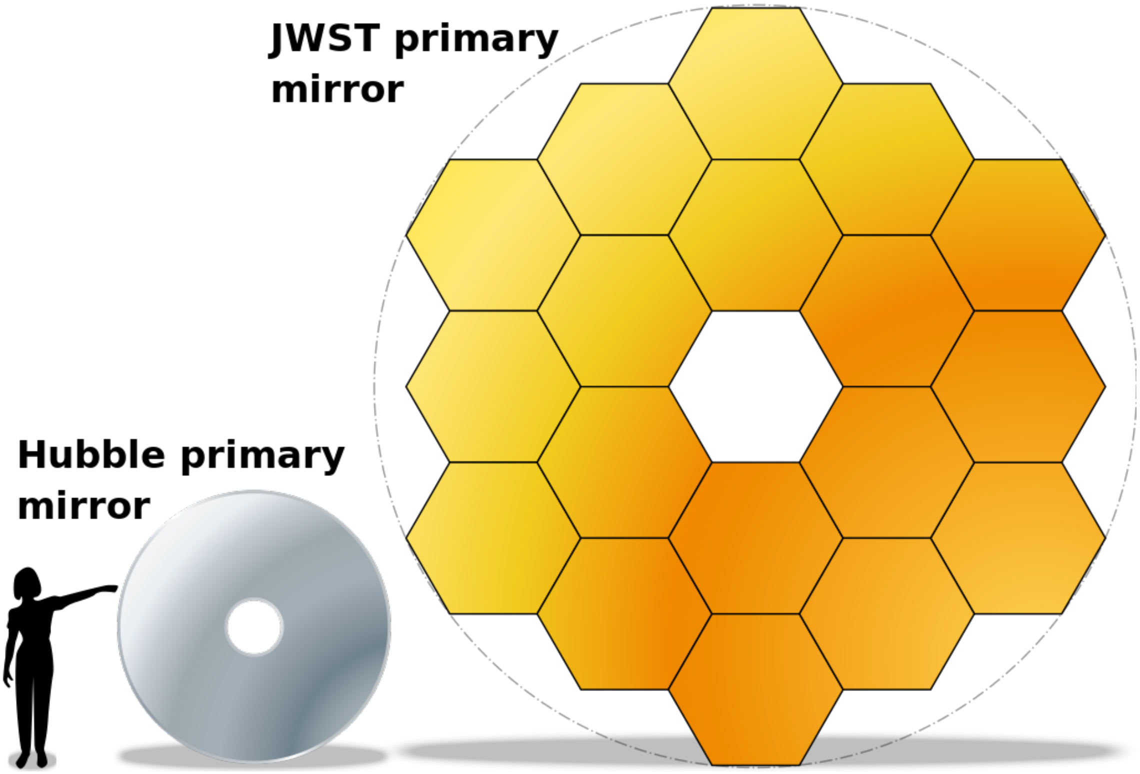

Figure 5.2: Size comparison for the primary mirrors of the Hubble Space Telescope and the James Webb Space Telescope.

5.2.3 A new way to observe escaping atmospheres

Until recently, most observations of the upper atmospheres of exoplanets were made using measurements at UV wavelengths, which can only be done from space, with HST. The advantage of using helium to probe exoplanet atmospheres is that it can be done from the ground. Recently, several high-resolution infrared spectrographs have come online (thanks to efforts to find Earth-mass planets around M-dwarfs with the radial velocity technique). These instruments are capable of resolving the shape of the helium 10 830Å triplet, which provides much more information about the upper atmospheres, including wind speeds. These observations can be combined with 3D models of extended and escaping atmospheres and reveal how planets lose their atmospheres to space. For example - are the outflows magnetically confined?

The schematic in Figure 5.3 explains a possible future method to search for magnetic confinement of planetary outflows using measurements of 10 830Å absorption. In any case, many more observations of helium in exoplanet atmospheres have already been scheduled, and they should hopefully reveal, at least, which planets are prone to atmospheric escape, and how we can better predict their mass-loss rates. TESS will find planets around small, bright stars, which, with their relatively high XUV-output, will be favourable for observations of atmospheric helium. Such observations could perhaps be used to quantify the size of any hydrogen/helium envelopes of planets smaller than 4 Earth radii, and begin to reveal the nature of super-Earths and mini-Neptunes.

5.2.4 WASP-127b with JWST

Time on JWST will be extremely competitive, and it will be difficult to justify spending time observing an exoplanet atmosphere that may be cloudy, and so have a flat spectrum at infrared wavelengths. Our observations of WASP-127b's atmosphere have revealed strong evidence for large absorption features out to 4.5 microns in the infrared. Additionally, WASP-127b orbits a bright star, and it has a long transit duration which means high-signal-to-noise observations will be possible. These combined facts make WASP-127b a standout target for transmission spectroscopy with JWST. In particular, it will be possible to reveal which carbon-bearing species is responsible for the absorption feature we detect at 4.5 microns. Öberg et al. (2011) suggest that by measuring the carbon-to-oxygen ratios of exoplanet atmospheres we can learn where the planet formed in relation to the H_2O and CO snowlines in its protoplanetary disk. If JWST measurements of water and carbon-bearing molecules in WASP-127b's atmosphere can be combined with an understanding of its 3D temperature structure, cloud distribution, and dynamics, then perhaps we can begin to learn how the planet formed. This may help to explain why the planet has such an unusually low density.

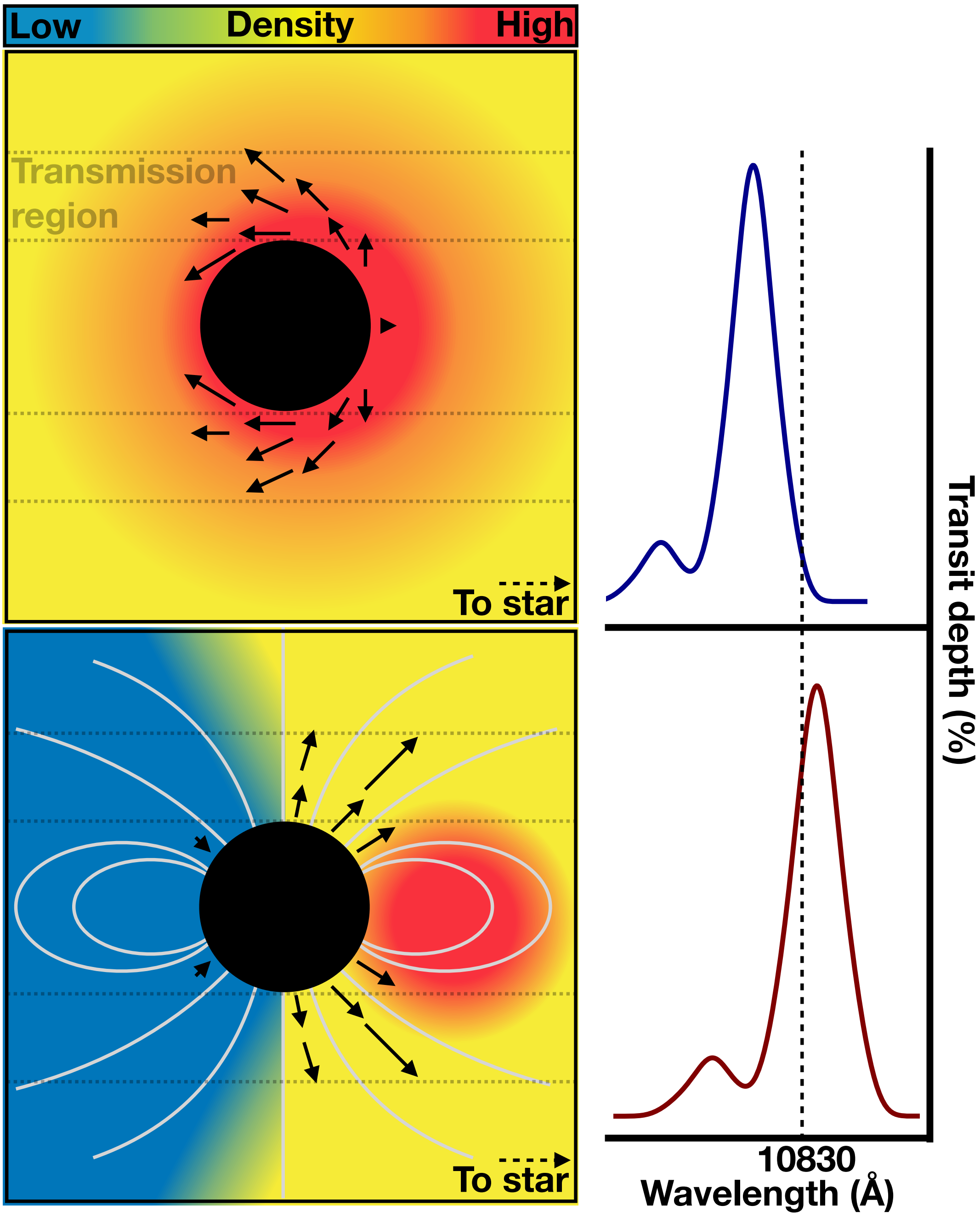

Figure 5.3: Schematic of method to infer magnetic confinement of exoplanetary winds. Without a magnetic field (top row) the planetary wind is blown away from the star by radiation pressure and thermal pressure gradients, and the 10 830Å helium absorption line is redshifted. With a dipole magnetic field the outflow is constrained along field lines (shown in grey) and the line is blueshifted. Note the over-dense substellar region which could potentially be targeted in emission spectra. Based on models from Owen & Adams (2014).

5.3 Closing remarks

Exoplanets are complex objects, but it is difficult to observe them in detail because they are so faint compared to their stars, and so small compared to interstellar space. To answer our many questions about them we need the best of our skills as both planetologists and astronomers. That means we must understand individual planets as many interconnected physical parts, but also keep an accurate eye on the entire sky and its billions of stars.

Bibliography

Ackerman, A. S. & Marley, M. S. 2001, ApJ, 556, 872

Afram, N. & Berdyugina, S. V. 2015, A&A, 576, A34

Aigrain, S., Pont, F., & Zucker, S. 2012, MNRAS, 419, 3147

Allart, R., Bourrier, V., Lovis, C., et al. 2019, arXiv e-prints

Allart, R., Bourrier, V., Lovis, C., et al. 2018, Science, 362, 1384

Alonso, R., Brown, T. M., Torres, G., et al. 2004, ApJ, 613, L153

Ambikasaran, S., Foreman-Mackey, D., Greengard, L., Hogg, D. W., & O'Neil, M. 2014

Amundsen, D. S., Baraffe, I., Tremblin, P., et al. 2014, A&A, 564, A59

Amundsen, D. S., Mayne, N. J., Baraffe, I., et al. 2016, A&A, 595, A36

Anderson, D. R., Collier Cameron, A., Delrez, L., et al. 2017, A&A, 604, A110

Anderson, D. R., Gillon, M., Maxted, P. F. L., et al. 2010, A&A, 513, L3

Andretta, V. & Giampapa, M. S. 1995, ApJ, 439, 405

Andretta, V., Giampapa, M. S., Covino, E., Reiners, A., & Beeck, B. 2017, ApJ, 839, 97

Andretta, V. & Jones, H. P. 1997, ApJ, 489, 375

Arcangeli, J., Desert, J.-M., Parmentier, V., et al. 2019, arXiv e-prints

Armstrong, D. J., de Mooij, E., Barstow, J., et al. 2016, Nature Astronomy, 1, 0004

Bakos, G., Noyes, R. W., Kovács, G., et al. 2004, PASP, 116, 266

Barclay, T., Pepper, J., & Quintana, E. V. 2018, ApJS, 239, 2

Barman, T. 2007, ApJ, 661, L191

Barstow, J. K., Aigrain, S., Irwin, P. G. J., & Sing, D. K. 2017, ApJ, 834, 50

Bean, J. L., Miller-Ricci Kempton, E., & Homeier, D. 2010, Nature, 468, 669

Beer, R. 1975, ApJ, 200, L167

Bell, T. J. & Cowan, N. B. 2018, ApJ, 857, L20

Bell, T. J., Nikolov, N., Cowan, N. B., et al. 2017, ApJ, 847, L2

Ben-Jaffel, L. & Ballester, G. E. 2013, A&A, 553, A52

Benneke, B. & Seager, S. 2012, ApJ, 753, 100

Benneke, B. & Seager, S. 2013, ApJ, 778, 153

Berdyugina, S. V. 2005, Living Reviews in Solar Physics, 2, 8

Biller, B. A., Vos, J., Bonavita, M., et al. 2015, ApJ, 813, L23

Bonnefoy, M., Zurlo, A., Baudino, J. L., et al. 2016, A&A, 587, A58

Borucki, W. J., Koch, D., Basri, G., et al. 2010, Science, 327, 977

Bourrier, V. & Lecavelier des Etangs, A. 2013, A&A, 557, A124

Bourrier, V., Lecavelier des Etangs, A., Ehrenreich, D., et al. 2018, A&A, 620, A147

Bourrier, V., Lecavelier des Etangs, A., Ehrenreich, D., Tanaka, Y. A., & Vidotto, A. A. 2016, A&A, 591, A121

Brammer, G., Pirzkal, N., McCullough, P., & MacKenty, J. 2014, Time-varying Excess Earth-glow Backgrounds in the WFC3/IR Channel, Tech. rep.

Brown, T. M. 2001, The Astrophysical Journal, 553, 1006

Brown, T. M., Charbonneau, D., Gilliland, R. L., Noyes, R. W., & Burrows, A. 2001, ApJ, 552, 699

Burrows, A., Hubbard, W. B., Lunine, J. I., & Liebert, J. 2001, Reviews of Modern Physics, 73, 719

Burrows, A. & Sharp, C. M. 1999, ApJ, 512, 843

Castelli, F. & Kurucz, R. L. 2004, ArXiv Astrophysics e-prints

Charbonneau, D., Allen, L. E., Megeath, S. T., et al. 2005, ApJ, 626, 523

Charbonneau, D., Brown, T. M., Latham, D. W., & Mayor, M. 2000, ApJ, 529, L45

Charbonneau, D., Brown, T. M., Noyes, R. W., & Gilliland, R. L. 2002, ApJ, 568, 377

Chauvin, G., Desidera, S., Lagrange, A.-M., et al. 2017, A&A, 605, L9

Chen, G., Pallé, E., Welbanks, L., et al. 2018, A&A, 616, A145

Chen, H. & Rogers, L. A. 2016, ApJ, 831, 180

Christie, D., Arras, P., & Li, Z.-Y. 2013, ApJ, 772, 144

Claret, A. 2000, A&A, 363, 1081

Cowan, N. B. & Agol, E. 2008, ApJ, 678, L129

Cowan, N. B., Machalek, P., Croll, B., et al. 2012, ApJ, 747, 82

Crossfield, I. J. M. 2015, PASP, 127, 941

Crossfield, I. J. M., Barman, T., & Hansen, B. M. S. 2011, ApJ, 736, 132

Crossfield, I. J. M., Hansen, B. M. S., Harrington, J., et al. 2010, ApJ, 723, 1436

Crossfield, I. J. M. & Kreidberg, L. 2017, AJ, 154, 261

Currie, T., Burrows, A., Itoh, Y., et al. 2011, ApJ, 729, 128

Czesla, S., Klocová, T., Khalafinejad, S., Wolter, U., & Schmitt, J. H. M. M. 2015, A&A, 582, A51

Dai, F. & Winn, J. N. 2017, AJ, 153, 205

Dang, L., Cowan, N. B., Schwartz, J. C., et al. 2018, Nature Astronomy, 2, 220

Davis, T. A. & Wheatley, P. J. 2009, MNRAS, 396, 1012

Dawson, R. I. & Johnson, J. A. 2018, ARA&A, 56, 175

Deming, D., Knutson, H., Kammer, J., et al. 2015, ApJ, 805, 132

Deming, D., Seager, S., Richardson, L. J., & Harrington, J. 2005, Nature, 434, 740

Deming, D. & Sheppard, K. 2017, ApJ, 841, L3

Deming, D., Wilkins, A., McCullough, P., et al. 2013, ApJ, 774, 95

Demory, B.-O., Gillon, M., de Wit, J., et al. 2016, Nature, 532, 207

Désert, J.-M., Charbonneau, D., Demory, B.-O., et al. 2011, ApJS, 197, 14

Diamond-Lowe, H., Berta-Thompson, Z., Charbonneau, D., & Kempton, E. M. R. 2018, AJ, 156, 42

Dobbs-Dixon, I. & Lin, D. N. C. 2008, ApJ, 673, 513

Dragomir, D., Teske, J., Gunther, M. N., et al. 2019, arXiv e-prints

Drake, G. W. 1971, Phys. Rev. A, 3, 908

Dressing, C. D. & Charbonneau, D. 2015, ApJ, 807, 45

Drummond, B., Tremblin, P., Baraffe, I., et al. 2016, A&A, 594, A69

Eastman, J., Gaudi, B. S., & Agol, E. 2013, PASP, 125, 83

Ehrenreich, D., Bourrier, V., Wheatley, P. J., et al. 2015, Nature, 522, 459

Erkaev, N. V., Kulikov, Y. N., Lammer, H., et al. 2007, A&A, 472, 329

Esposito, M., Armstrong, D. J., Gandolfi, D., et al. 2019, A&A, 623, A165

Evans, T. M., Aigrain, S., Gibson, N., et al. 2015, MNRAS, 451, 680

Evans, T. M., Pont, F., Sing, D. K., et al. 2013, ApJ, 772, L16

Evans, T. M., Sing, D. K., Goyal, J. M., et al. 2018, AJ, 156, 283

Evans, T. M., Sing, D. K., Kataria, T., et al. 2017, Nature, 548, 58

Evans, T. M., Sing, D. K., Wakeford, H. R., et al. 2016, ApJ, 822, L4

Fazio, G. G., Hora, J. L., Allen, L. E., et al. 2004

Fink, U. & Larson, H. P. 1978, Science, 201, 343

Foreman-Mackey, D., Hogg, D. W., Lang, D., & Goodman, J. 2013, PASP, 125, 306

Fortney, J. J. 2005, MNRAS, 364, 649

Fortney, J. J., Lodders, K., Marley, M. S., & Freedman, R. S. 2008, ApJ, 678, 1419

Fortney, J. J., Shabram, M., Showman, A. P., et al. 2010, ApJ, 709, 1396

Fossati, L., Haswell, C. A., Froning, C. S., et al. 2010, ApJ, 714, L222

Fraine, J., Deming, D., Benneke, B., et al. 2014, Nature, 513, 526

France, K., Loyd, R. O. P., Youngblood, A., et al. 2016, ApJ, 820, 89

Fulton, B. J., Petigura, E. A., Howard, A. W., et al. 2017, AJ, 154, 109

Gibson, N. P., Aigrain, S., Roberts, S., et al. 2012, MNRAS, 419, 2683

Gillon, M., Triaud, A. H. M. J., Demory, B.-O., et al. 2017, Nature, 542, 456

Gondoin, P. 2008, A&A, 478, 883

Gordon, I., Rothman, L. S., Wilzewski, J. S., et al. 2016, in AAS/Division for Planetary Sciences Meeting Abstracts, Vol. 48, AAS/Division for Planetary Sciences Meeting Abstracts #48, 421.13

Goudfrooij, P. & Christensen, J. A. 1998, STIS Near-IR Fringing. III. A Tutorial on the Use of the IRAF Tasks, Tech. rep.

Goyal, J. M., Mayne, N., Sing, D. K., et al. 2018, MNRAS, 474, 5158

Goyal, J. M., Wakeford, H. R., Mayne, N. J., et al. 2019, MNRAS, 482, 4503

Greene, T. P., Line, M. R., Montero, C., et al. 2016, ApJ, 817, 17

Guillot, T. 2010, A&A, 520, A27

Guillot, T., Burrows, A., Hubbard, W. B., Lunine, J. I., & Saumon, D. 1996, ApJ, 459, L35

Hansen, B. M. S. 2008, ApJS, 179, 484

Haswell, C. A., Fossati, L., Ayres, T., et al. 2012, ApJ, 760, 79

Hellier, C., Anderson, D. R., Collier-Cameron, A., et al. 2011, ApJ, 730, L31

Helling, C., Jardine, M., Stark, C., & Diver, D. 2013, ApJ, 767, 136

Helling, C., Thi, W.-F., Woitke, P., & Fridlund, M. 2006, A&A, 451, L9

Helling, C., Woitke, P., & Thi, W.-F. 2008, A&A, 485, 547

Heng, K. & Lyons, J. R. 2016, ApJ, 817, 149

Heng, K., Menou, K., & Phillipps, P. J. 2011, MNRAS, 413, 2380

Henry, G. W. 1999, PASP, 111, 845

Hodgman, S. S., Dall, R. G., Byron, L. J., et al. 2009, Phys. Rev. Lett., 103, 053002

Hollands, M. A., Gänsicke, B. T., & Koester, D. 2018, MNRAS, 477, 93

Huang, C. X., Burt, J., Vanderburg, A., et al. 2018, ApJ, 868, L39

Hubbard, W. B., Fortney, J. J., Lunine, J. I., et al. 2001, ApJ, 560, 413

Huitson, C. M., Sing, D. K., Pont, F., et al. 2013, MNRAS, 434, 3252

Huitson, C. M., Sing, D. K., Vidal-Madjar, A., et al. 2012, MNRAS, 422, 2477

Husser, T.-O., Wende-von Berg, S., Dreizler, S., et al. 2013, A&A, 553, A6

Irwin, J., Aigrain, S., Hodgkin, S., et al. 2006, MNRAS, 370, 954

Irwin, J., Berta, Z. K., Burke, C. J., et al. 2011, ApJ, 727, 56

Irwin, J. M., Berta-Thompson, Z. K., Charbonneau, D., et al. 2015, in Cambridge Workshop on Cool Stars, Stellar Systems, and the Sun, Vol. 18, 18th Cambridge Workshop on Cool Stars, Stellar Systems, and the Sun, ed. G. T. van Belle & H. C. Harris, 767–772

Irwin, P. G. J., Teanby, N. A., de Kok, R., et al. 2008, J. Quant. Spec. Radiat. Transf., 109, 1136

Isaacson, H. & Fischer, D. 2010, ApJ, 725, 875

Jeans, J. 1925, The Dynamical Theory of Gases, 1st edn. (Cambridge University Press)

Jensen, A. G., Redfield, S., Endl, M., et al. 2012, ApJ, 751, 86

Jin, S., Mordasini, C., Parmentier, V., et al. 2014, ApJ, 795, 65

Jones, M. I., Brahm, R., Espinoza, N., et al. 2018, arXiv e-prints

Jordán, A., Espinoza, N., Rabus, M., et al. 2013, ApJ, 778, 184

Kataria, T., Showman, A. P., Fortney, J. J., et al. 2015, ApJ, 801, 86

Kataria, T., Sing, D. K., Lewis, N. K., et al. 2016, ApJ, 821, 9

Katsanis, R. M. & McGrath, M. A. 1998, The Calstis IRAF Calibration Tools for STIS Data, Tech. rep.

King, G. W., Wheatley, P. J., Bourrier, V., & Ehrenreich, D. 2019, MNRAS, 484, L49

King, G. W., Wheatley, P. J., Salz, M., et al. 2018, MNRAS, 478, 1193

Kirk, J., Wheatley, P. J., Louden, T., et al. 2017, MNRAS, 468, 3907

Kirk, J., Wheatley, P. J., Louden, T., et al. 2016, MNRAS, 463, 2922

Knutson, H. A., Benneke, B., Deming, D., & Homeier, D. 2014, Nature, 505, 66

Knutson, H. A., Charbonneau, D., Allen, L. E., Burrows, A., & Megeath, S. T. 2008, ApJ, 673, 526

Knutson, H. A., Charbonneau, D., Allen, L. E., et al. 2007, Nature, 447, 183

Knutson, H. A., Charbonneau, D., Cowan, N. B., et al. 2009, ApJ, 703, 769

Knutson, H. A., Lewis, N., Fortney, J. J., et al. 2012, ApJ, 754, 22

Koskinen, T. T., Yelle, R. V., Lavvas, P., & Lewis, N. K. 2010, ApJ, 723, 116

Kramida, A. 2008, in APS Division of Atomic, Molecular and Optical Physics Meeting Abstracts, OPR.10

Kreidberg, L. 2015, PASP, 127, 1161

Kreidberg, L., Bean, J. L., Désert, J.-M., et al. 2014, Nature, 505, 69

Kreidberg, L., Line, M. R., Bean, J. L., et al. 2015, ApJ, 814, 66

Kreidberg, L., Line, M. R., Parmentier, V., et al. 2018a, AJ, 156, 17

Kreidberg, L., Line, M. R., Thorngren, D., Morley, C. V., & Stevenson, K. B. 2018b, ApJ, 858, L6

Kulow, J. R., France, K., Linsky, J., & Loyd, R. O. P. 2014, ApJ, 786, 132

Kuntschner, H., Bushouse, H., Kümmel, M., & Walsh, J. R. 2009, WFC3 SMOV proposal 11552: Calibration of the G102 grism, Tech. rep.

Lagrange, A.-M., Bonnefoy, M., Chauvin, G., et al. 2010, Science, 329, 57

Lam, K. W. F., Faedi, F., Brown, D. J. A., et al. 2017, A&A, 599, A3

Lammer, H., Odert, P., Leitzinger, M., et al. 2009, A&A, 506, 399

Lammer, H., Selsis, F., Ribas, I., et al. 2003, ApJ, 598, L121

Lavie, B., Mendonça, J. M., Mordasini, C., et al. 2017, AJ, 154, 91

Lecavelier Des Etangs, A. 2007, A&A, 461, 1185

Lecavelier Des Etangs, A., Ehrenreich, D., Vidal-Madjar, A., et al. 2010, A&A, 514, A72

Lecavelier Des Etangs, A., Pont, F., Vidal-Madjar, A., & Sing, D. 2008, A&A, 481, L83

Lecavelier des Etangs, A., Vidal-Madjar, A., McConnell, J. C., & Hébrard, G. 2004, A&A, 418, L1

Lee, G., Dobbs-Dixon, I., Helling, C., Bognar, K., & Woitke, P. 2016, A&A, 594, A48

Li, H., You, J., Yu, X., & Du, Q. 2007, Sol. Phys., 241, 301

Line, M. R., Wolf, A. S., Zhang, X., et al. 2013, ApJ, 775, 137

Lines, S., Mayne, N. J., Boutle, I. A., et al. 2018, A&A, 615, A97

Lodders, K. 2003, ApJ, 591, 1220

Lopez, E. D. & Fortney, J. J. 2014, ApJ, 792, 1

Lopez, E. D., Fortney, J. J., & Miller, N. 2012, ApJ, 761, 59

Louden, T. & Kreidberg, L. 2018, MNRAS, 477, 2613

Louden, T. & Wheatley, P. J. 2015, ApJ, 814, L24

Macintosh, B., Graham, J. R., Barman, T., et al. 2015, Science, 350, 64

Madhusudhan, N., Agúndez, M., Moses, J. I., & Hu, Y. 2016, Space Sci. Rev., 205, 285

Madhusudhan, N., Burrows, A., & Currie, T. 2011, ApJ, 737, 34

Madhusudhan, N. & Seager, S. 2009, ApJ, 707, 24

Mandell, A. M., Haynes, K., Sinukoff, E., et al. 2013, ApJ, 779, 128

Marley, M. S. & Robinson, T. D. 2015, ARA&A, 53, 279

Marois, C., Macintosh, B., Barman, T., et al. 2008, Science, 322, 1348

Maxted, P. F. L., Anderson, D. R., Doyle, A. P., et al. 2013, MNRAS, 428, 2645

Mayne, N. J., Baraffe, I., Acreman, D. M., et al. 2014, A&A, 561, A1

Mayor, M. & Queloz, D. 1995, Nature, 378, 355

McCullough, P. R., Crouzet, N., Deming, D., & Madhusudhan, N. 2014, ApJ, 791, 55

Mendonça, J. M., Tsai, S.-m., Malik, M., Grimm, S. L., & Heng, K. 2018, ApJ, 869, 107

Menou, K. & Rauscher, E. 2009, ApJ, 700, 887

Morley, C. V., Fortney, J. J., Kempton, E. M.-R., et al. 2013, ApJ, 775, 33

Moses, J. I., Visscher, C., Fortney, J. J., et al. 2011, ApJ, 737, 15

Moutou, C., Coustenis, A., Schneider, J., Queloz, D., & Mayor, M. 2003, A&A, 405, 341

Močnik, T., Hellier, C., Anderson, D. R., Clark, B. J. M., & Southworth, J. 2017, MNRAS, 469, 1622

Murray-Clay, R. A., Chiang, E. I., & Murray, N. 2009, ApJ, 693, 23

Nelson, B. E., Ford, E. B., & Rasio, F. A. 2017, AJ, 154, 106

Nielsen, L. D., Bouchy, F., Turner, O., et al. 2019, A&A, 623, A100

Nikolov, N., Chen, G., Fortney, J. J., et al. 2013, A&A, 553, A26

Nikolov, N., Sing, D. K., Burrows, A. S., et al. 2015, MNRAS, 447, 463

Nikolov, N., Sing, D. K., Fortney, J. J., et al. 2018, Nature, 557, 526

Nikolov, N., Sing, D. K., Pont, F., et al. 2014, MNRAS, 437, 46

Nortmann, L., Pallé, E., Salz, M., et al. 2018, Science, 362, 1388

Nutzman, P. & Charbonneau, D. 2008, PASP, 120, 317

Öberg, K. I., Murray-Clay, R., & Bergin, E. A. 2011, ApJ, 743, L16

Oklopčić, A. & Hirata, C. M. 2018, ApJ, 855, L11

Osterbrock, D. E. & Ferland, G. J. 2006, Astrophysics of gaseous nebulae and active galactic nuclei

Owen, J. E. & Adams, F. C. 2014, MNRAS, 444, 3761

Owen, J. E. & Jackson, A. P. 2012, MNRAS, 425, 2931

Owen, J. E. & Wu, Y. 2013, ApJ, 775, 105

Palle, E., Chen, G., Prieto-Arranz, J., et al. 2017, A&A, 602, L15

Parker, E. N. 1958, ApJ, 128, 664

Parmentier, V. & Crossfield, I. J. M. 2018, Exoplanet Phase Curves: Observations and Theory, 116

Parmentier, V., Fortney, J. J., Showman, A. P., Morley, C., & Marley, M. S. 2016, ApJ, 828, 22

Parmentier, V. & Guillot, T. 2014, A&A, 562, A133

Parmentier, V., Showman, A. P., & Lian, Y. 2013, A&A, 558, A91

Perna, R., Menou, K., & Rauscher, E. 2010, ApJ, 724, 313

Pollacco, D. L., Skillen, I., Collier Cameron, A., et al. 2006, PASP, 118, 1407

Pont, F., Sing, D. K., Gibson, N. P., et al. 2013, MNRAS, 432, 2917

Poppenhaeger, K., Schmitt, J. H. M. M., & Wolk, S. J. 2013, ApJ, 773, 62

Rackham, B., Espinoza, N., Apai, D., et al. 2017, ApJ, 834, 151

Rackham, B. V., Apai, D., & Giampapa, M. S. 2018, ApJ, 853, 122

Rameau, J., Chauvin, G., Lagrange, A.-M., et al. 2013, ApJ, 779, L26

Redfield, S., Endl, M., Cochran, W. D., & Koesterke, L. 2008, in Astronomical Society of the Pacific Conference Series, Vol. 393, New Horizons in Astronomy, ed. A. Frebel, J. R. Maund, J. Shen, & M. H. Siegel, 259

Ricker, G. R., Winn, J. N., Vanderspek, R., et al. 2015, Journal of Astronomical Telescopes, Instruments, and Systems, 1, 014003

Rodgers, C. D. 2000, Inverse methods for atmospheric sounding : theory and practice, ed. C. D. Rodgers (World Scientific Publishing)

Rothman, L. S., Gordon, I. E., Barber, R. J., et al. 2010, J. Quant. Spec. Radiat. Transf., 111, 2139

Salz, M., Czesla, S., Schneider, P. C., et al. 2018, A&A, 620, A97

Salz, M., Czesla, S., Schneider, P. C., & Schmitt, J. H. M. M. 2016, A&A, 586, A75

Sanz-Forcada, J. & Dupree, A. K. 2008, A&A, 488, 715

Schwartz, J. C., Kashner, Z., Jovmir, D., & Cowan, N. B. 2017, ApJ, 850, 154

Seager, S. & Mallén-Ornelas, G. 2003, ApJ, 585, 1038

Seager, S., Richardson, L. J., Hansen, B. M. S., et al. 2005, ApJ, 632, 1122

Seager, S. & Sasselov, D. D. 2000, ApJ, 537, 916

Sedaghati, E., Boffin, H. M. J., Jeřabková, T., et al. 2016, A&A, 596, A47

Showman, A. P., Fortney, J. J., Lian, Y., et al. 2009, ApJ, 699, 564

Showman, A. P. & Guillot, T. 2002, A&A, 385, 166

Sing, D. K., Fortney, J. J., Nikolov, N., et al. 2016, Nature, 529, 59

Sing, D. K., Lecavelier des Etangs, A., Fortney, J. J., et al. 2013, MNRAS, 436, 2956

Sing, D. K., Pont, F., Aigrain, S., et al. 2011, MNRAS, 416, 1443

Sing, D. K., Wakeford, H. R., Showman, A. P., et al. 2015, MNRAS, 446, 2428

Smith, Maximilian Zavodny, G. R. M. B. 2008, Calibration of image persistence in HgCdTe photodiodes

Snellen, I. A. G., Albrecht, S., de Mooij, E. J. W., & Le Poole, R. S. 2008, A&A, 487, 357

Snellen, I. A. G., Brandl, B. R., de Kok, R. J., et al. 2014, Nature, 509, 63

Snellen, I. A. G., de Kok, R. J., de Mooij, E. J. W., & Albrecht, S. 2010, Nature, 465, 1049

Spake, J. J., Sing, D. K., Evans, T. M., et al. 2018, Nature, 557, 68

Stevenson, K. B., Désert, J.-M., Line, M. R., et al. 2014, Science, 346, 838

Stevenson, K. B., Harrington, J., Lust, N. B., et al. 2012, ApJ, 755, 9

Stevenson, K. B., Harrington, J., Nymeyer, S., et al. 2010, Nature, 464, 1161

Stevenson, K. B., Line, M. R., Bean, J. L., et al. 2017, AJ, 153, 68

Swain, M. R., Vasisht, G., & Tinetti, G. 2008, Nature, 452, 329

Takeda, Y. & Takada-Hidai, M. 2011, PASJ, 63, 547

Tennyson, J., Yurchenko, S. N., Al-Refaie, A. F., et al. 2016, Journal of Molecular Spectroscopy, 327, 73

Thompson, S. E., Coughlin, J. L., Hoffman, K., et al. 2018, ApJS, 235, 38

Tinetti, G., Vidal-Madjar, A., Liang, M.-C., et al. 2007, Nature, 448, 169

Tody, D. 1993, in Astronomical Society of the Pacific Conference Series, Vol. 52, Astronomical Data Analysis Software and Systems II, ed. R. J. Hanisch, R. J. V. Brissenden, & J. Barnes, 173

Tremblin, P., Amundsen, D. S., Chabrier, G., et al. 2016, ApJ, 817, L19

Tremblin, P., Amundsen, D. S., Mourier, P., et al. 2015, ApJ, 804, L17

Tremblin, P. & Chiang, E. 2013, MNRAS, 428, 2565

Tsuji, T. 2002, ApJ, 575, 264

Tsuji, T. 2005, ApJ, 621, 1033

Tsuji, T., Nakajima, T., & Yanagisawa, K. 2004, ApJ, 607, 511

Turner, J. D., Christie, D., Arras, P., Johnson, R. E., & Schmidt, C. 2016, MNRAS, 458, 3880

Udalski, A., Paczynski, B., Zebrun, K., et al. 2002, Acta Astron., 52, 1

Vanderspek, R., Huang, C. X., Vanderburg, A., et al. 2019, ApJ, 871, L24

Vaughan, Jr., A. H. & Zirin, H. 1968, ApJ, 152, 123

Venot, O., Hébrard, E., Agúndez, M., et al. 2012, A&A, 546, A43

Verner, D. A. & Yakovlev, D. G. 1995, A&AS, 109, 125

Vidal-Madjar, A., Désert, J.-M., Lecavelier des Etangs, A., et al. 2004, ApJ, 604, L69

Vidal-Madjar, A., Lecavelier des Etangs, A., Désert, J.-M., et al. 2003, Nature, 422, 143

Wakeford, H. R. & Sing, D. K. 2015, A&A, 573, A122

Wakeford, H. R., Sing, D. K., Deming, D., et al. 2013, MNRAS, 435, 3481

Wakeford, H. R., Sing, D. K., Deming, D., et al. 2018, AJ, 155, 29

Wakeford, H. R., Sing, D. K., Kataria, T., et al. 2017, Science, 356, 628

Waldmann, I. P., Tinetti, G., Rocchetto, M., et al. 2015, ApJ, 802, 107

Wang, S., Jones, M., Shporer, A., et al. 2019, The Astronomical Journal, 157, 51

Watson, A. J., Donahue, T. M., & Walker, J. C. G. 1981, Icarus, 48, 150

Wheatley, P. J., Louden, T., Bourrier, V., Ehrenreich, D., & Gillon, M. 2017, MNRAS, 465, L74

Wheatley, P. J., West, R. G., Goad, M. R., et al. 2018, MNRAS, 475, 4476

Wong, I., Knutson, H. A., Kataria, T., et al. 2016, ApJ, 823, 122

Wong, I., Knutson, H. A., Lewis, N. K., et al. 2015, ApJ, 811, 122

Yan, F. & Henning, T. 2018, Nature Astronomy, 2, 714

Zahnle, K. J. & Marley, M. S. 2014, ApJ, 797, 41

Zarro, D. M. & Zirin, H. 1986, ApJ, 304, 365

Zellem, R. T., Lewis, N. K., Knutson, H. A., et al. 2014, ApJ, 790, 53

Zhang, X. & Showman, A. P. 2017, ApJ, 836, 73

Zhou, Y., Apai, D., Lew, B. W. P., & Schneider, G. 2017, AJ, 153, 243

Zirin, H. 1982, ApJ, 260, 655

Zuckerman, B., Koester, D., Melis, C., Hansen, B. M., & Jura, M. 2007, ApJ, 671, 872